Ultra High Energy Neutrinos and Gamma Rays in Astrophysics: A Multi-messenger Study

Submitted in partial fulfillment of the requirements
for the degree of

Doctor of Philosophy

by

Prantik Sarmah
(Roll No. 186121018)

Supervisor:
Dr. Sovan Chakraborty

Department of Physics

INDIAN INSTITUTE OF TECHNOLOGY GUWAHATI
Guwahati - 781039, Assam, India

This thesis is dedicated to my parents and brother....

Declaration

Prantik Sarmah
Roll No. 186121018
Department of Physics
Indian Institute of Technology Guwahati
Guwahati, India
email: prantik@iitg.ac.in

I hereby declare that works presented in the thesis entitled "**Ultra High Energy Neutrinos and Gamma Rays in Astrophysics: A Multi-messenger Study**" have been carried out by me under the supervision of **Dr. Sovan Chakraborty** at the Department of Physics, Indian Institute of Technology Guwahati, India. The thesis has not been submitted anywhere else for any degree. Works presented in the thesis are all my own unless referenced to the contrary in the thesis.

Date: 20-10-2023

Signature

Certificate

Dr. Sovan Chakraborty
Associate Professor
Department of Physics
Indian Institute of Technology Guwahati
Guwahati, India
email: prantik@iitg.ac.in

It is certified that the work contained in the thesis entitled "**Ultra High Energy Neutrinos and Gamma Rays in Astrophysics: A Multi-messenger Study**" by Mr. Prantik Sarmah (Roll No. - 186121018), a Ph.D. student in the Department of Physics, Indian Institute of Technology Guwahati is carried out under my supervision and has not been submitted elsewhere for the award of any other degree.

Date: 20-10-2023

Sovan Chakraborty

Signature

Acknowledgements

As I approach the conclusion of this remarkable five-year journey, it is time to express my gratitude to the many significant individuals who have consistently supported and made valuable contributions along the way.

First and foremost, I extend my heartfelt gratitude to my thesis supervisor, Dr. Sovan Chakraborty, whose unwavering support, friendly mentorship, and expertise have been instrumental in shaping this research. I consider myself very fortunate to have a supervisor who has been not only approachable but also open to discussing a wide range of topics, including academic matters. I am confident that our association will not conclude here and will continue indefinitely.

I am deeply indebted to my collaborators, whose collaboration and collective effort have significantly enhanced the quality and scope of this research. Irene Tamborra, Katie Auchettl, Poonam Mehta, Jagdish Joshi, Moon moon Devi, Debanjan Bose, and Abinash Medhi, your collaboration has been inspiring, and I am thankful for the opportunities to work alongside such talented individuals.

I would like to acknowledge and thank my doctoral committee for their insightful feedback and guidance throughout this research endeavor. Prof. Bipul Bhuyan, as the chairperson of the committee, I appreciate your leadership and constructive input. Dr. Debasish Borah and Dr. Debaprasad Maity, your expertise in the field has enriched this work, and I am grateful for your contributions. I am equally appreciative of Dr. Subhaditya Bhattacharya, Dr. Sayan Chakraborti, Dr. Charudatt Kadolkar, Dr. Santabrata Das, and Dr. M.C. Kumar, with whom I've had valuable opportunities to engage in discussions not only pertaining to physics but also on broader topics.

I extend my gratitude to the heads of the Department of Physics, both past and present. Prof. Perumal Algarswammy, our present Head of the Department, and Prof. Subhradip Ghosh, our past Head of the Department, your leadership has created an environment conducive to academic excellence, and I am thankful for your support.

I would also like to acknowledge the Department of Physics and my institute as a whole for providing the resources and infrastructure necessary for this research. Special thanks to Basab da for helping me out to resolve various technical issues related softwares which I have faced in my initial days.

I would like to acknowledge the support and encouragements of our research group mem-

bers Madhurima Chakraborty (senior) and Esha Bhatia (junior). Although my association with Tarun and Soumen is very new, I must acknowledge their kindness and support.

I would like to acknowledge my all batch mates, with special mention to Sumit, Suruj, Sahabub and Debu. I am indebted to all my seniors, especially Dibyendu da, Kajal da, Lopa di, Topo da, Arghya da, Samit, Ipsita di, Devabrat and Pritam for always being supportive and inspirational. I am also thankful to my juniors like Gargi and Nayan.

I extend my heartfelt gratitude to all my friends, particularly Alakesh, Kumar, Kunjan, Dilip, Shiva, Suma, Anindita, Sangeeta, and Utpal with whom I have shared many wonderful moments.

I express my gratitude and profound appreciation to my professors during my master's program at NIT Silchar, including Dr. Subhasis Panda, Dr. Rupak Dutta, Dr. Asim Roy, Dr. Avijit Choudhury, Dr. Soumya R Mohapatra, and Dr. R. G. Nair. Their inspiration and motivation have been instrumental in guiding me towards a research path in physics.

Although being separated from my home and family was challenging, the presence of my close relatives around has greatly eased my life. I am deeply grateful to Kunja jethai, Kamal da, and Mimi for their love and support. No less than I extend my thanks to Pehi, Peha, Mon, Pushpa jethai, and Baby ba for their affection and support.

Above all, the individuals who serve as the ultimate source of my motivation are my parents and dada, without whom my very existence would be incomplete. I deeply appreciate their love and support.

To all those mentioned above and to anyone else who has been a part of this academic journey, I offer my heartfelt thanks. Your contributions have been integral to the successful completion of my PhD thesis.

List of publications

1. **“High energy particles from young supernovae: gamma-ray and neutrino connections"**, **Prantik Sarmah**, Sovan Chakraborty, Irene Tamborra, Katie Auchettl
   *e*print: arXiv: 2204.03663 [astro-ph.HE],
   Published in **JCAP 08 (2022) 08, 011**,
   Remark: Chapter 3 and Chapter 5 are based on this.

2. **“Probing LHAASO galactic PeVatrons through gamma-ray and neutrino correspondence"**, **Prantik Sarmah**, Sovan Chakraborty, Jagdish C. Joshi
   *e*print: arXiv: 2301.04161 [astro-ph.HE],
   Published in **Mon.Not.Roy.Astron.Soc. 521 (2023) 1, 1144-1151**,
   Remark: Chapter 2 is based on this.

3. **“Gamma-rays and neutrinos from supernovae of Type Ib/c with late time emission"**, **Prantik Sarmah**, Sovan Chakraborty, Irene Tamborra, Katie Auchettl
   *e*print: arXiv: 2303.13576 [astro-ph.HE],
   Published in **Under review**,
   Remark: Chapter 4 is based on this.

4. **“A relook at the GZK Neutrino-Photon Connection: Impact of Extra-galactic Radio Background & UHECR properties"**, Sovan Chakraborty, Poonam Mehta, **Prantik Sarmah**
   *e*print: arXiv: 2307.15667 [astro-ph.HE],
   Published in **Under review**,
   Remark: Chapter 6 and Chapter 7 are based on this.

5. **“New constraints on the gamma-ray and high energy neutrino fluxes from the circumstellar interaction of SN 2023ixf"**, **Prantik Sarmah**
   *e*print: arXiv: 2307.08744 [astro-ph.HE],
   Published in **Under review**,
   Remark: Not included in the thesis.

Abstract

Cosmic rays (CRs) accelerated in astrophysical sources like supernovae (SNe), active galactic nuclei interacting with different targets such protons (ambient medium, interstellar gas) or photons (ambient photons, ISRF, CMB, ERB, EBL) can produce different secondary particles such as gamma-rays, high energy neutrinos, electrons and positrons. Among these secondaries, Gamma-rays (photons) and high energy neutrinos play crucial role in the study of high energy astrophysics. Neutrinos being weakly interacting propagate without any losses, while photons can attenuate due pair production losses on the background photons, e.g., CMB, ERB. These secondaries have emerged to be powerful multi-messenger tools as they carry information about both the origin and propagation of CRs. Due to advancement of experiments like Fermi-LAT (gamma-ray) and IceCube (neutrino), detection of these secondaries has become a reality, opening the door to multi-messenger analysis. In this thesis, we explore gamma-ray and neutrino flux produced in different point as well as diffuse CR sources and analyse their detection prospects with current and upcoming generation of different gamma-ray (e.g., Fermi-LAT, LHAASO ,CTA, Auger, GRAND) and neutrino (e.g., IceCube, IceCube-Gen2, KM3NeT,Auger, GRAND) telescopes.

For point sources, we consider several galactic sources (SN remnants, pulsars) detected by LHAASO as well as different types (IIn, II-P, IIb/II-L, Ib/c and Ib/c (LT)) of young SNe (YSNe) powered by shock-CSM interaction. For diffuse fluxes of gamma-rays and neutrinos, we consider YSNe and Ultra-high Energy CRs (UHECR). Galactic sources and YSNe contribute in the energy range from GeV to a few decades of PeV, whereas the UHECRs contribute in the EeV energies. In the lower energies, gamma-rays and neutrinos are produced through interaction of CRs with target protons i.e, inelastic $p-p$ collisions. While in the UHE energies, gamma-rays and neutrinos are produced as result of CRs interacting with CMB photons, the so called GZK process. The effect of ERB on the propagation of the GZK photons is crucial and depends on different ERB models. We explore the impact of different ERB models and

associated uncertainties on the GZK photon flux in detail.

We show that the fluxes of gamma-rays and high energy neutrinos from the galactic sources are detectable in the experiments like CTA, IceCube-Gen2, and KM3NeT. Whereas among the YSNe types, Type IIn has been found to be detectable in neutrino and gamma-ray telescopes up to a few Mpc. The remaining YSNe types are found to be detectable at shorter distances. In fact, our study shows that the diffuse flux of high energy neutrinos from YSNe can explain the diffuse neutrino flux detected by IceCube. The corresponding diffuse gamma-ray flux is found to be below the diffuse gamma-ray flux measured by Fermi-LAT. In the UHE regime, we estimate the fluxes of GZK photons and GZK neutrinos. The ERB uncertainties are found to give rise to large uncertainties in the GZK photon flux. Our estimated GZK fluxes are below the existing sensitivities of current experiments such as Auger and IceCube, but detectable in upcoming IceCube-Gen2 and GRAND experiments. We use the IceCube-Gen2 sensitivity to obtain the primary UHECR properties as the neutrino flux propagates without attenuation. Using these constraints, we obtain a multi-messenger limit on the GZK photon flux.

Contents

Chapter 1

Introduction

Ever since the discovery of cosmic rays (CRs) by Victor Hess in 1912, our understanding of CRs has been growing in leaps and bounds. In particular, the CR spectrum has been measured in great detail. The CR spectrum measured by various experiments extends over a broad energy range from 10^9 eV to 10^{20} eV. (1; 2). A single power law fitting of this spectrum has revealed a spectral index of about 2.7 and two breaks at energies around 10^{15} eV and 10^{18} eV which are traditionally referred to as the "knee" and "ankle", respectively (1; 2). The general understanding of the observed CR spectrum is that the CRs are certainly extrasolar, originating either in our own Galaxy (Milky-way) or in some external galaxies. The CRs up to the knee are thought to be originated in Milky-way, whereas those above the ankle have extra-galactic origin (1; 2). The CRs above the ankle are generally referred to as ultra-high energy cosmic rays (UHECR) (3). However, yet there are many open questions about the properties and origin of CRs (4; 3; 1). These CRs are believed to be mostly produced through shock acceleration of low energy particles. Several acceleration mechanisms have been proposed to explain the observed CR spectrum at different energies, but a complete understanding is yet elusive. Similarly, detection of CRs, (5; 6; 7) beyond the Greisen (8), Zatsepin and Kuzmin (9) (GZK) cut-off (4×10^{19} eV) necessitates a thorough comprehension of the propagation of UHECR. This is be-

cause CRs above this cut-off travelling more than 6 Mpc are expected to attenuate substantially after interacting with the CMB and there are no known sources within this distance (3; 10). The composition of UHECR is another issue in UHECR physics. Our present understanding of the CR composition based is on different observations. The Fly's Eye experiment reported a prevalence of predominantly light elements at these energies (11). However, the AGASA experiment failed to confirm this observation (12). Recent measurements carried out by the Auger Observatory suggest that as energies increase, there is an increasing tendency for cosmic rays to consist of heavier elements (13; 14; 15; 16; 17). In fact, all these issues in CR physics multiply as the direct observations of CRs are not sufficient to decode the sources and propagation of CRs. This is due to the fact that the CRs can deflect in the Galactic as well as inter-galactic magnetic fields.

Recent developments in multi-messenger astronomy emerge to be powerful tools in CR physics probe and can be helpful in understanding the CR sources and propagation (18; 19; 20). Multi-messenger analysis primarily involves the examination of various potential signals such as electromagnetic radiation, gravitational waves, gamma-rays and high energy neutrinos associated with CRs. Once CRs undergo acceleration, they can engage in collisions with various targets, including ambient gas or photons within the source region. Moreover, during their journey through the Galaxy, they may interact with interstellar gases and different radiation fields, such as the Inter-Stellar Radiation Field (ISRF) or Cosmic Microwave Background (CMB). These interactions typically involve inelastic processes, such as proton-proton ($p-p$) collisions and photo-hadronic interactions ($p\gamma$). These collisions give rise to the production of secondary particles, which include electrons, high-energy neutrinos, and gamma-rays. While secondary electrons, being charged particles, experience energy losses due to interactions with magnetic fields and exhibit deviations in their trajectories, rendering them less useful for directional analysis. However, the trajectories of gamma-rays and neutrinos are not influenced by magnetic fields. Detecting gamma-rays and neutrinos, therefore, provides a means to trace back to the sources' directions. Neutrinos, characterized by their weak interactions, undergo negligible energy losses and hence proven valuable for gaining insights into the properties of CR sources. Conversely, gamma-rays can interact with low-energy photons within the source environment or with photons from various backgrounds such as the ISRF, CMB, Extra-galactic Background Light (EBL), and Extra-galactic Radio Background (ERB), leading to the production of electron-positron pairs. Consequently, gamma-rays may experience energy losses along

their journey. Detecting gamma-rays offers a means to understand the region between the CR sources and Earth, shedding light on the processes of CR propagation. Thus, the combined detection of gamma-rays and neutrinos serves as a powerful probe for investigating the origin and propagation of cosmic rays.

The field of multi-messenger analysis has undergone a profound transformation thanks to advancements in detection technologies, exemplified by instruments like Fermi Large Area Telescope (Fermi-LAT) for gamma-rays and IceCube for high-energy neutrinos [1]. Perhaps the most notable illustration of multi-messenger detection is the joint observation of the blazar TXS 0506+056 by these telescopes (21). Beyond Fermi-LAT, there are other gamma-ray detectors like Large High Altitude Air Shower Observatory (LHAASO) and Tibet-ASγ that have unveiled captivating discoveries in recent times (22; 23). Currently, the Auger Observatory plays a crucial role in searching ultra-high-energy cosmic rays (UHECRs) and the secondary particles resulting from the Greisen-Zatsepin-Kuzmin (GZK) mechanism. Looking ahead, the future of multi-messenger astrophysics appears promising with the advent of numerous planned experiments and detectors. These forthcoming initiatives encompass projects such as the Cherenkov Telescope Array (CTA) (24), IceCube-Gen2 (25), KM3NeT (26), and the Giant Radio Array for Neutrino Detection (GRAND) (27). These developments have collectively rendered the field of multi-messenger astrophysics not only captivating but also full of promise.

In this thesis, we undertake a comprehensive multi-messenger exploration of CR secondary particles (high energy neutrinos and gamma-rays) encompassing a wide span of the CR spectrum, ranging from TeV to ZeV. Our research involves detailed phenomenological investigations into the fluxes of gamma-rays and high-energy neutrinos, commencing with the early phases of various supernovae (SNe) types and extending to the phenomena occurring within supernova remnants (SNRs). Additionally, we engage in a multi-messenger examination of the origins of UHECR through detecting GZK photons and GZK neutrinos. Below, we offer an overview of the diverse topics that will be addressed throughout this thesis.

In the lower energies around the knee, indirect evidences for CR production up to PeV energies have been provided by recent gamma-ray detection by LHAASO from several Galactic sources like supernova remnants (SNR), pulsars (22; 28). This is because CR interaction

[1] We must not forget the recent revolution in gravitational wave astronomy via detection of numerous sources of gravitational waves.

with neighbouring molecular cloud (inelastic $p-p$ collision, (29)) can produce a number of charged and neutral pions that further decay to secondaries like gamma-rays and high energy neutrinos. However, no neutrinos are detected by the present high energy neutrino detectors like IceCube and ANTARES. In this regard, we analyse the detection possibilities of neutrinos from these sources with present and upcoming high energy neutrino telescopes like IceCube (30; 21; 31), IceCube-Gen2 and KM3NeT. Although the sources are found to be beyond the reach of IceCube, the upcoming IceCube-Gen2 and KM3NeT might be able to detect some of these sources.

Particle (protons) acceleration up to a few decades of PeV energies is also found to be feasible in early phase (1 year time scale) of supernova (SN) explosion (32; 33; 34; 35; 36). Strong shock waves created by interaction of high speed SN ejecta with dense circumstellar medium (CSM) may drive such acceleration. The dense CSM is created by heavy mass-loss of massive stars in years prior to SN explosion, (37; 38; 39; 40). The accelerated protons then collide with the non-relativistic protons (inelastic $p-p$ collision) in the unshocked CSM producing secondary gamma-rays and high energy neutrinos. Evidence of CSM interaction has been inferred from multi-wavelength observations of many SNe (38; 41; 42; 43; 44). However, neither gamma-rays nor neutrinos have yet been detected from such sources. Probable recent SN event candidates are found to have occurred at distances, beyond the reach of present gamma-ray and neutrino detectors (34; 33; 45). Recently, Fermi-LAT detected gamma-rays from the direction of a peculiar supernova iPTF14hls (46). Such discovery is however uncertain because of the presence of a blazar in the detection error circle. We analyse the reach of the current and forthcoming gamma-ray and high energy neutrino detectors for different types of such SNe (IIn, II-P, IIb, II-L and Ib/c). One might also look for such gamma-rays and high energy neutrinos in the SN graveyard. The reason being past SNe across the universe could create diffuse backgrounds these secondaries. These diffuse backgrounds might have contributions to the Isotropic Gamma-ray Background (IGRB) (47) and High Energy Starting Events (HESE), (48) detected by Fermi-LAT and IceCube, respectively. We analyse these possible contributions from different types of SNe like IIn, II-P, IIb, II-L and Ib/c. The diffuse gamma-ray background from SNe is found to be much below the Fermi-LAT IGRB. On the other hand, the corresponding diffuse neutrino background is found to have significant contributions to the HESE events.

In the extreme energies beyond the ankle, we investigate the fluxes of GZK secondaries

such as gamma-rays and neutrinos which are produced as a result of UHECRs interacting with the CMB (the GZK effect) (8; 9; 10). This interaction produces charged and neutral pions giving rise to the secondaries, GZK neutrinos and GZK photons (gamma-rays) (49). As a result of the GZK effect, the UHECR flux at Earth is expected to attenuate substantially above the GZK cut-off ($\sim 4 \times 10^{19}$ eV) (10; 50). Detection of the secondary signals from this GZK process can provide us with an opportunity for multi-messenger study of UHECRs. We estimate the diffuse background of GZK neutrinos and GZK photons for a wide range of the source and propagation parameter space. Subsequently, we analyse the detection prospects of these secondaries with various present and upcoming UHECR and UHE neutrino detectors (5; 25; 51; 27). The present detectors are found to be incapable of detecting these secondary signals. However, some of the proposed future detectors (IceCube-Gen2, GRAND200k and Auger upgrade) show exciting potential for GZK flux detection. In addition, we provide a multi-messenger constraint on the GZK photon flux from the IceCube-Gen2 sensitivity limit to the GZK neutrino flux.

In the following sections, we offer a brief overview of CR physics, encompassing insights into their sources and the mechanisms responsible for their production. Furthermore, we delve into the intricate process of cosmic ray propagation, which results in the generation of secondary signals, notably high-energy neutrinos and gamma-rays. We then explore the significance of these signals in the context of conducting multi-messenger analyses, serving as valuable tools for investigating the realm of cosmic ray physics.

1.1 Cosmic rays

Cosmic ray experiments play a pivotal role in unraveling the mysteries of high-energy particles originating from space. These experiments span a wide range of energies and locations to provide insights into cosmic ray composition, origins, and behavior. The Pierre Auger Observatory (Auger), located in Argentina, focuses on UHECR, operating within the energy range of 10^{18} eV to 10^{20} eV (52). It employs an extensive array of surface detectors and fluorescence telescopes to investigate the sources of the most energetic CRs. The Telescope Array (TA) Project, situated in Utah, USA, primarily studies high-energy CRs, typically ranging from a few 10^{17} eV to 10^{20} eV (53). Using fluorescence detectors and ground-based detectors, it delves into the

sources and composition of these CRs. AMS-02 (54), onboard the International Space Station, observes medium to high-energy CRs, spanning from a few GeV to several TeV. It serves a dual purpose by not only studying CRs but also searching for dark matter and antimatter in space. The Fly's Eye Experiment, conducted in Utah, USA, specializes in UHECRs, particularly those exceeding 10^{19} eV. This pioneering experiment employed fluorescence detectors to scrutinize and analyze the highest-energy CRs. AGASA (Akeno Giant Air Shower Array), based in Japan, concentrates on UHECRs, typically above 10^{18} eV (7). AGASA consisted of an array of detectors to investigate the arrival directions and energies of these high-energy particles.

Looking to the future, the Giant Radio Array for Neutrino Detection (GRAND) is an upcoming experiment that aims to explore CRs using radio signals (27). GRAND will cover a broad energy range and offer valuable insights into the most energetic particles in the universe, complementing the efforts of existing experiments.

Together, these experiments contribute significantly to our understanding of CRs, shedding light on their energy spectra, sources, and composition across various energy ranges. Each experiment is tailored to its specific energy range of interest, advancing our knowledge of these enigmatic particles from space.

The global CR energy spectrum measured by the various experiments is shown in Fig. 1.1. The spectrum spans over about 12 decades of energies, starting from GeV to beyond 10^{20} eV. The most striking feature of this spectrum is that it has a single power law behaviour throughout all energies with a spectral index of about 2.7. However, there are certain deviations at energies around the knee ($\sim$ 1 PeV) and the anke ($\sim$ 1 EeV). At low energies (below TeV), the CR flux is very large, i.e., every second, there is 1 CR particle hitting 1 m^2 area of the Earth's atmosphere. The rate of CRs drops rapidly with energy, e.g., the rate around the knee is about 1 particle$/(m^2 - \text{year})$. Cosmic rays at the extreme tail of the spectrum are very rare, *i.e*, we observe about 1 particle per km^2 in a century. The CR composition is also measured in the above mentioned experiments and found to be primarily consisting of about 90% protons, 9% alpha particles and 1% other heavier nuclei (1). The CRs at low energies (below the knee) as well as those above are reasonably understood. However, there are several open issues regarding the CRs such as their sources, composition and production mechanism which are not yet completely understood. In the following, we provide a brief overview of these questions.

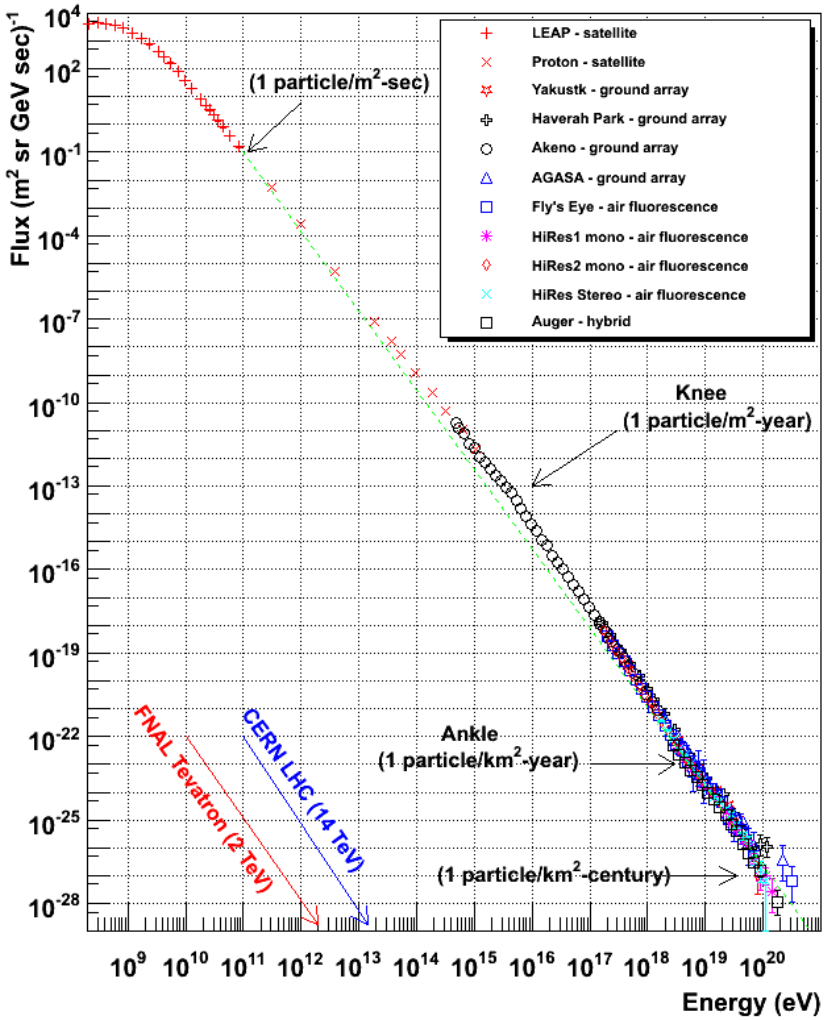

Figure 1.1: Cosmic ray spectrum measured by different experiments (55).

1.1.1 Sources

The sources of cosmic rays (CRs) are known to exhibit a wide range of diversity. CRs with energies just a few orders of magnitude above the 'knee' are thought to originate from particles accelerated by SN blastwaves within our own Milky Way galaxy. Apart from SNR, Galactic pulsars are also found to be probable CR source candidates. Substantial supporting evidence backs this theory, including the detection of statistically significant anisotropy in the distribution of CRs below the knee (3). Furthermore, it is expected that the intensity of CRs will be at its highest near the Galactic center and gradually decrease as one moves away from this central region. This distinctive pattern is anticipated to be reflected in the production of secondary gamma-rays resulting from the interaction between CRs and interstellar gas. Although not definitive, there are observational indications that lend support to this argument (3).

The spectral feature known as the 'ankle,' occurring around 1 EeV in the cosmic ray (CR) spectrum, is widely considered to mark the transition point from Galactic to extra-galactic cosmic rays. Cosmic rays above the ankle are seldom referred to as ultra-high energy cosmic rays (UHECRs) and are believed to originate from extra-galactic sources. Several factors contribute to this hypothesis. Firstly, these UHECRs exhibit a high degree of isotropy in their distribution. Secondly, within the Milky Way, there are no known sources capable of producing particles with such exceptionally high energies. This is primarily because the gyration radius of protons in the Galactic magnetic field is of a comparable scale to that of our entire Galaxy, rendering containment and effective acceleration mechanisms implausible. While the identification of specific extra-galactic objects as definitive sources of UHECRs remains elusive, several potential candidates have been proposed, including active galactic nuclei (AGNs), radio galaxies, pulsars, and gamma-ray bursts (GRBs). The production of UHECR in these sources is believed to be through shock acceleration in relativistic jets.

In addition to this bottom-up approach of UHECR production, there is a top-down mechanism in the literature. In this top-down hypothesis, UHECRs are believed to be produced through the decay of exotic objects such as super heavy dark matter, cosmic strings and many more (see Ref. 3, for details). However, these models are very strongly constrained by different UHECRs observations (52). In this thesis we shall be focusing on the bottom-up approach only.

1.1.2 Composition

The chemical composition of the high energy CRs represents another aspect that remains poorly comprehended. The prevailing anticipation is that these CRs should consist of a diverse range of elements (1; 2; 3). Our understanding of cosmic ray composition relies on data collected from various ground-based and space-based telescopes, as well as balloon experiments. However, it's important to note that this data primarily reflects the composition of cosmic rays at Earth or just beyond Earth's atmosphere. It's quite possible that the composition of cosmic rays at their source differs significantly from what these measurements indicate.

Based on the measurements, it has been determined that CRs up to energies of approximately 1 TeV are overwhelmingly comprised of protons. These CRs are primarily believed to originate within the confines of our solar system, potentially accelerated within the solar wind. Note that at these energies, other particles such as electrons, positrons, and anti-protons exist, but their abundance is orders of magnitude lower than that of protons. Notably, the composition of CRs has been observed to change with increasing energy. For example, As we move beyond the 1 TeV energy range, the CR spectrum encompasses a variety of elements together with protons and is predominantly composed of particles originating from outside our solar system. However, in the vicinity of the CR spectrum knee, the contribution of the heavier elements towards the composition decreases.

In the UHE regime, specifically beyond the ankle, the composition of CRs also remains a subject of uncertainty. The Fly's Eye experiment initially reported a predominantly light composition at these energies (11). However, the AGASA experiment could not substantiate this finding (12). Recent measurements conducted by the Auger Observatory have indicated that the prevalence of heavier elements in CRs tends to rise with increasing energy (13; 14; 15; 16; 17).

1.1.3 CR acceleration

A significant inquiry in the realm of cosmic ray physics pertains to the mechanisms responsible for generating CR particles spanning from GeV to ZeV energies. Broadly, there are two conceivable production scenarios referred to as 'top-down' and 'bottom-up.' As previously men-

tioned, top-down production models face considerable constraints imposed by observations. Conversely, the literature predominantly explores 'bottom-up' approaches, where particles are accelerated to high energies, primarily grounded in Fermi's original proposal. In the following, we briefly discuss these bottom-up models.

In 1949, Fermi introduced the original Fermi mechanism, proposing a method to accelerate particles (56; 1; 2). According to his idea, these particles accelerate undergoing multiple encounters with magnetized clouds within the galaxy. During each interaction, the particle's energy would either increase or decrease, depending on whether the encounter was head-on or overtaking. The magnetized nature of the clouds would lead to collisionless scattering of the particles with the magnetic field irregularities, preventing energy loss and thermalization. Given that head-on collisions outnumber overtaking ones on average, particles would tend to gain energy through this process. The net gain in energy for a particle after exiting the acceleration region is proportional to the square of the cloud velocity (v), i.e $\left(\frac{v}{c}\right)^2$, where c is the speed of light. Because of this velocity squared dependence, this process is known as second order acceleration. The accelerated particles results in a power law distribution in energy with a power law index which depends on the escape timescale of the particle as well as fraction of energy gain.

However, this acceleration mechanism is not very efficient due to the $\left(\frac{v}{c}\right)^2$ dependence of the energy gain. In addition, the power law index depends on various properties of the acceleration region such as cloud speed and escape time of the particles. Due to these limitations of the Fermi's original idea, several alternate acceleration mechanisms were proposed in the late 1970s. This led to development of the Fermi's first order acceleration mechanism which is often referred to as diffusive shock acceleration. This mechanism was developed independently by Axford, Leer and Skadron (1977) (57), Krymsky (1977) (58), Bell (1978) (59) and Blandford and Ostriker (1978) (60). We shall discuss here the approach of Bell (1978) in which the behaviour of individual particle is studied. This model is based on particle acceleration by strong shock waves produced by astrophysical environments such as supernova (SN) explosions, active galactic nuclei (AGN). The shock is assumed to be collisionless so that energy losses due to different particle interaction is negligible. In this acceleration, a strong shock is generally assumed to move with supersonic velocity ($\mathbf{v}_1$) sweeping up a diffuse gas. Thus, the shocked gas moves away from the shock with a velocity ($\mathbf{v}_2$) relatively smaller than the shock speed. In

this process, the particles in the shocked gas attain a net velocity which is equal to $|\mathbf{v}_1 - \mathbf{v}_2|$ implying the net energy gain proportional to this velocity difference. Due to presence of magnetic field in the plasma, charged particles can be trapped in the acceleration region for sufficiently long time causing repeated back and forth encounters with the shock. This process can lead the particles to accelerate to extremely high energy. Like the second order mechanism, this mechanism also gives rise to a power law distribution of the accelerated particles. The key feature of the particle distribution in this process is that it gives power law index which is independent of the properties of the acceleration environment and predicted to be around 2.

Because of the universal nature of the spectral shape, this mechanism has been widely acknowledged by the astrophysical community. However, it has certain limitations arising from oversimplified assumptions. These assumptions encompass an oversimplified shock geometry, a lack of consideration for the impact of accelerated particles on the shock's structure, and the lack of understanding for the origin of the necessary magnetic field fluctuations responsible for particle scattering. Furthermore, this approach is primarily tailored to non-relativistic shocks, which may not be suitable for ultra-relativistic shocks found in objects such as GRBs. One can expect significant modifications in the particle distribution such as deviation of spectral index from the standard value, 2 due to the influence of these phenomena (see 3; 61; 62, for details). Thus in the following analysis, we allow the spectral index of the primary CR particles to vary around 2.

Another aspect of this acceleration mechanism is the maximum energy of a particle that a astrophysical source can produce. This maximum energy is estimated by the famous Hillas Criterion (63), i.e, for CRs to be accelerated to energies beyond a certain threshold ($E_{\rm max}$), the gyration radius of these particles within the accelerator region ($r_{\rm g}$) must be smaller than or comparable to the size of the accelerator (R). When this condition is met, it implies that CRs can be effectively confined and accelerated within the source. The maximum attainable energy ($E_{\rm max}$) can then be calculated by rearranging the gyration radius equation:

$$E_{\rm max} = qBR \approx 1 \text{ EeV} \times Z \left(\frac{B}{\mu\text{G}}\right) \left(\frac{R}{\text{kpc}}\right) \tag{1.1}$$

This fundamental limit on maximum achievable energy provides an intuition on the nature

of the sources of CR accelerators such as size and magnetic field.

1.2 Production and propagation of secondaries

CRs accelerated to very high energies in different astrophysical sources can undergo various propagation effects effectively interacting with the background particles create a flux of secondary particles such as neutrinos, gamma-rays, electrons and positrons (29; 49). These background target particles can be of different origin such as interstellar gas, molecular clouds in the Galaxy and extra-galactic photon backgrounds like CMB, ERB, EBL. The general interaction of CRs with gas particles or molecular clouds is considered to be inelastic proton-proton ($p-p$) collision (29), whereas the major interaction with photon background is considered to be photo-production ($p\gamma$) of pions (49). It is crucial to note that the CRs can also take part in other interactions such as electron pair production on photon backgrounds and other radiative losses such as synchrotron, inverse Compton. Depending on the energy of the parent CRs, these processes can show dominant effects at different energies. In general, the $p-p$ collision has a lower threshold energy (GeV) and leads to production of charged and neutral pions. On the other hand, the threshold energy of CRs for the $p\gamma$ interaction depends on the energy of the target photons, e.g, a CR particle requires energy of about 4×10^{10} GeV to interact with a CMB photon (3). This process also produces charged and neutral pions. In both the above processes, the charged and neutral pions decay to give rise to secondary high energy particles such as gamma-rays, neutrinos and electrons. In the following we briefly discuss the propagation of gamma-rays and neutrinos.

The secondary particles produced in CR interaction can take part in various interaction in their production site or during propagation to Earth depending on the propagation medium. The charged secondaries, electrons and positrons suffer severe radiative losses such as synchrotron and bremsstrahlung and their trajectories are strongly deflected by magnetic field in the intergalactic space or in our own Milky-Way (3). In most cases, these charged secondaries are attenuated heavily and can not reach Earth. Hence, they are not treated useful messengers. While on the other hand, propagation of the secondary gamma-rays and high energy neutrinos are not effected by magnetic field. Thus, their trajectories can point back to the direction of

their origin and can be useful to probe the sources.

The neutrinos being weakly interacting in nature propagate without any losses. Thus, neutrinos are crucial information carriers. While the gamma-rays can interact with low energy photons as well as ambient matter at source and with different photon backgrounds such as EBL, CMB and ERB during propagation through space (45; 10; 3; 64). Due to such interactions gamma-rays can produce electron positron pairs and suffer losses resulting in attenuated flux. The attenuation depends on the optical depth of the target photons which in turn depends on the energy of the target photons as well as their number density. As the photons of CMB, EBL and ERB have different energies, their effects show up at different energies in the gamma-ray flux. For instance, as the CMB photons have higher energies than the ERB ones, the attenuation due to CMB in the gamma-ray flux would be pronounced in lower energies whereas the effect of ERB would appear at higher energies. It should be noted that gamma-ray flux can also be modified by electromagnetic cascades such pair annihilation, inverse Compton by primary and secondary electrons. Thus, the resultant gamma-ray flux at Earth encodes information about all these processes and the photon backgrounds. Note that secondary electrons as well as shock accelerated primary electrons can produce low energy gamma-rays as well as hard X-rays which can dominate the low energy flux (34; 65). However in this thesis we mostly focus on high energy gamma-rays, i.e, above 100 MeV where these contributions are negligible.

Although neutrinos suffer negligible energy losses during propagation as mentioned above, they can undergo flavour oscillation. In general, neutrino oscillations are of two types: vacuum and Mikheyev-Smirnov-Wolfenstein (MSW) oscillation. Vacuum oscillation occurs when neutrinos propagate through space over large distance, whereas MSW oscillation arises when neutrinos traverse through matter with varying electron density, such as those found in the Sun or the Earth. The neutrino oscillation probability increases with propagation length but decrease with increasing energy (see 66, for details). Thus, the high energy neutrinos need to propagate large distances (cosmological scale) to undergo substantial flavour conversions. The maximum impact of MSW oscillation occurs at resonance which requires a high resonance matter density for TeV-PeV neutrinos (67). As the density of the Earth or Sun is not high enough to achieve resonance, the expected effect of MSW oscillation on high-energy neutrino flux is negligible. Therefore, neutrinos can undergo vacuum oscillation only. In the vacuum oscillation scenario, the flavour ratio of astrophysical high energy neutrinos becomes equal, i.e,

$\nu_e : \nu_\mu : \nu_\tau = 1 : 1 : 1$ (68; 69; 70; 71; 72). Hence, we will consider the equal flavour ratio through out this thesis.

As neutrinos and gamma-rays are linked to the parent cosmic rays through the $p - p$ or $p\gamma$ interaction channel, their combined detection can lead us to multi-messenger analysis which can be useful for understanding the properties of CR sources as well as CR propagation. In the following, we briefly discuss the essence of multi-messenger analysis with gamma-ray and neutrino detectors.

1.3 Multi-messenger analysis

Multi-messenger astrophysics represents a cutting-edge approach to unravel the mysteries of the universe by simultaneously studying multiple cosmic messengers, such as high-energy neutrinos, gamma-rays, gravitational waves and electromagnetic radiation (X-rays, radio waves etc.) (18; 19; 20). These messengers provide complementary insights into some of the most extreme and enigmatic astrophysical phenomena. In this thesis, we focus on the study involving high energy neutrinos and gamma-rays.

High-energy neutrinos are nearly massless, chargeless particles that can traverse vast cosmic distances without interaction, making them ideal for studying distant and highly energetic sources. They can be produced in extreme environments like supernovae, gamma-ray bursts, and active galactic nuclei as a result of CR interactions as discussed above. Detecting high-energy neutrinos on Earth is a significant challenge due to their elusive nature, but specialized detectors like IceCube at the South Pole have made remarkable progress in this field. In addition to IceCube, Auger is another detector capable of detecting UHE neutrinos. While these detectors are currently operating, there are several future plans such as IceCube-Gen2, KM3NeT, GRAND (25; 73; 27).

On the other hand, the CR interaction which produces the high energy neutrinos can also produce gamma-rays. Instruments like Fermi Gamma-ray Space Telescope and Auger have revolutionized our understanding of gamma-ray astronomy through detection of various gamma-ray source (74; 47; 75; 76; 77; 78; 5; 79). Recent inclusion in the technology, the LHAASO and Tibet-ASγ experiments have provided new insights in this field by detecting various gamma-ray

sources in our Milky-way (22; 23). In the coming future, detectors like CTA and GRAND will be able unveil many more secrets of the gamma-ray sky.

Multi-messenger analysis involves combining data from high-energy neutrino detectors like IceCube with observations from gamma-ray telescopes to gain a more comprehensive view of cosmic events. This synergy pinpoints the sources of high-energy phenomena with greater precision. For example, the detection of a high-energy neutrino can prompt astronomers to scan the sky for simultaneous gamma-ray emissions, helping to identify the astronomical objects responsible for these neutrinos. This was the case in 2017 when IceCube detected a high-energy neutrino, and astronomers were able to trace it back to the blazar TXS 0506+056, a type of active galactic nucleus, through its gamma-ray emissions (21).

This approach offers several advantages, including enhanced source localization, improved astrophysical modeling, and a deeper understanding of the extreme environments in the universe. It also provides an opportunity to test fundamental physics, such as the properties of neutrinos and the nature of cosmic accelerators.

In this thesis, we shall be utilizing observations of high energy neutrino detectors and gamma-ray telescopes mentioned to model gamma-ray and neutrino emission from CR interaction in sources like SNe. We shall also explore potential of the future planned telescopes to probe CR interactions through detection of high energy neutrinos and gamma-rays.

1.4 Structure of the thesis

This thesis is designed as follows. In Chapter 2, we estimate the gamma-ray and the high energy neutrino fluxes from 12 Galactic gamma-ray sources recently detected by the LHAASO experiments, followed by the analysis of their detection prospects. In Chapter 3, we explore the high energy neutrino and gamma-ray emission in interaction-powered SNe (interaction of SN ejecta with CSM). We estimate the fluxes of these particles for different types of SNe (IIn, II-P, IIb/II-L, Ib/c) and analyse their detection prospects. In Chapter 4, we provide a detailed analysis of gamma-ray and neutrino emission from a subclass of Ib/c SNe that have exhibited late interaction with far away dense CSM (based on observation of SN 2014C), followed by detection prospects of similar future events. In Chapter 5, we estimate the diffuse backgrounds

of gamma-rays and high energy neutrinos created by past interaction-powered SNe across the Universe. We also explore their possible connection with the observed neutrino and gamma-ray backgrounds by IceCube and Fermi-LAT. In Chapter 6, we explore production of UHECR and their interaction with CMB that leads to production of GZK neutrinos and photons. We also explore the dependence of these GZK secondaries on source properties and their propagation through inter-galactic space. In Chapter 7, we discuss in detail the impact of ERB model uncertainties on the propagation of GZK photon flux and analyse the detection prospects of both GZK secondaries with current and future experiments. The analysis is complimented by a multi-messenger analysis leading to crucial constraints on the GZK photon and neutrino flux. Finally, in Chapter 8, we provide a brief summary of the thesis and conclude.

Chapter 2

Point sources: The LHAASO PeVatrons

The advancement of high energy neutrino and gamma-ray detectors such as IceCube and Large Area Telescope on board the Fermi Space Telescope has opened up the window to multi-messenger analysis at high energies (TeV-PeV). Recent additions to the gamma-ray detection technology such as the Large High Altitude Air Shower Observatory (LHAASO) and Tibet Asγ experiments have provided new insights to this aspect. All these detectors are capable of discovering point sources as well as diffuse sources. Detection of any specific point source can provide crucial information about various properties such as high energy constituents, shock acceleration. On the other hand, the diffuse sources can provide with a broad understanding of high energy astrophysical sources such as their distribution across the Universe and the optimum limits of the source properties. Indeed, these detectors have already made some significant discoveries regarding both point sources as well as diffuse sources. In this chapter, we particularly discuss several Galactic gamma-ray sources detected by the LHAASO. We estimate the high energy neutrino fluxes from these sources utilizing the gamma-ray data from the LHAASO experiment and discuss their detection prospects with current and upcoming neutrino detectors. Detection of these neutrinos will open up multi-messenger probe of these sources and can be useful in understanding properties of these sources such as hadronic or leptonic, shock acceler-

ation.

2.1 The LHAASO Galactic PeVatrons

The LHAASO has recently detected PeV gamma-rays from a dozen of Galactic sources (PeVatrons). These gamma-rays are probably connected to the knee region of the observed cosmic ray (CR) spectrum at around 3 PeV and are expected to be produced by the Galactic sources (80). The probable source candidates for these gamma-rays are inferred to be Supernova remanants (SNRs), Pulsars, Pulsar Wind Nebulae (PWN) and star forming regions. However, none of these sources is firmly established as the origin of the PeV gamma-rays, except for the one which is found to be associated to the Crab Nebula. One of these sources has also been detected by the Tibe Asγ and found to be spatially associated with the SNR G106.3+2.7. It is important to note that, there has been detection of plethora of TeV gamma-ray sources, namely the TeV Catalogue (TeVCat) by various experiments such as High Altitute Water Cherenkov Observatory (HAWC), High Energy Stereoscopic System (H.E.S.S.), Very Energetic Radiation Imaging Telescope Array System (VERITAS) and Major Atmospheric Gamma Imaging Cherenkov Telescopes (MAGIC). On the other hand, the IceCube neutrino observatory has very recently announced a 4.5σ significance discovery of high energy neutrinos from the Galactic plane. The origin of these neutrinos is speculated to be either Galactic diffuse emission or some unresolved point sources. Nevertheless, this neutrino detection is found to be consistent with the gamma-ray source distribution.

There are two possible physical processes capable of producing PeV gamma-rays, i.e., the leptonic and hadronic. In the lepnonic process, gamma-rays of PeV energies can be produced through inverse Comptonisation of low energy photons by CR electrons. On the other hand, the hadronic process i.e., inelastic pp collision can yield gamma-rays via the decay of neutral pions produced in the pp collision. This hadronic process also produces charged pions that decays to create secondary neutrinos. Hence, the gamma-rays produced in hadronic process must be accompanied by high energy neutrinos. This multi-messenger connection distinguishes the hadronic origin from that of leptonic origin.

Both leptonic as well as hadronic processes requires CR particle (electrons and protons)

acceleration up to PeV energies. Supernova remnants (SNRs) and pulsars are considered to be the most favourable Galactic objects producing CRs around PeV energies (81; 82; 83; 84; 85). The LHAASO collaboration paper (22), have listed the SNRs and pulsars that are spatially associated with the observed gamma-rays and are consistent with the expected potential sources of CRs (86; 87; 88). Individual supernova remnants (SNRs), i.e., IC 443 and W44, in our Galaxy have also been detected by the Fermi-Satellite in the MeV-GeV band, providing important hints of proton acceleration in SNRs (89). Further, decade long observations of the Galactic centre region by the HESS telescope have indicated that Sagittarius A* could accelerate protons upto PeV energies (90).

Another interesting source in our Galaxy is CRAB pulsar wind nebula (PWN), in which the radiation has been observed from radio wavelengths to PeV gamma-rays. LHAASO collaboration have also detected high energy photons from CRAB PWN upto a maximum energy of (1.12 ± 0.09) PeV (91). They have interpreted the multi-wavelength radiation using a synchrotron self-Compton model with electrons having maximum energy ≈ 2.15 PeV, hence termed as leptonic PeVatron. However, the slightly larger gamma-ray flux at the tail of the UHE spectra in CRAB PWN is considered to be of hadronic origin (CR proton acceleration) (92; 93). Hence, CRAB PWN might be a source of both CR electrons and protons upto PeV energies. Indeed, the observed CR proton data by Dark Matter Particle Explorer (DAMPE) satellite indicates more than one class of Galactic CR sources (94; 95).

The gamma-rays detected by LHAASO can also have the possibility of both leptonic or hadronic origin (28; 22). In the leptonic channel, such gamma-rays may be produced by inverse Compton of relativistic electrons. For the hadronic channel, the interaction of CR protons with background protons in dense gas medium can provide a dominant contribution. Gamma-rays and neutrinos are produced simultaneously in this hadronic interaction (87; 96). Detection of the associated neutrinos together with the gamma-rays will probe this hadronic origin (97; 98) and will differentiate leptonic channel.

For the hadronic channel, interaction of CR protons accelerated in SNR with molecular cloud is considered to be a prominent source of the UHE flux. SNRs with age ($t_{age} \sim 100$ yr) are favoured as accelerators of CRs upto PeV energies due to amplification of the magnetic field in the downstream shock regions (83). The acceleration depends on the confinement time of CR protons and gas density of the acceleration zone. Longer confinement would provide the

protons with sufficient time to accelerate to higher energies. The association of UHE gamma-ray sources with old SNRs ($t_{age} \geq 10$ kyr) might indicate a long time confinement of CR protons, surrounding the SN shocks (99; 100). The gas density determines magnetic field strength and also responsible for CR energy losses due to interaction like $p-p$ collisions. For example, for a confinement time of about 10 kyr, the required source gas density is found to be about 10 cm^{-3} (see 101, for details). These accelerated protons are expected to escape the source and interact with neighbouring molecular clouds. Therefore, detection of neutrinos produced in these interactions is crucial to probe the origin of these PeVtrons.

These neutrinos might be detected by current (IceCube) and future (IceCube-Gen2, KM3NeT) high energy neutrino detectors. In fact, it has been shown that IceCube and KM3NeT are sensitive to objects like SNR G40.5-0.5 and Vela junior (102). IceCube has detected bunch of diffuse neutrinos over a period of 7.5 years (103). Although, most of these neutrinos are found to be of extra-galactic origin (45; 104; 36), the possibility of few of these events originating in the galaxy can not be ruled out (105; 106). In addition, detection of gamma-rays by LHAASO and TibeT AS+MD makes Galactic PeVatrons strong contenders of high energy neutrino factories, detection of neutrinos can reveal these gamma-ray associated PeVatrons.

In the following section, we shall build a hadronic ($p-p$) interaction model utilising the gamma-ray observations of two specific sources; SNR G106.3+2.7 and SNR G40.5-0.5 to estimate the gamma-ray and neutrino fluxes for the LHAASO sources. Both these sources have associated molecular cloud in close vicinity. The gamma-rays mostly illuminated by the molecular cloud motivates for this hadronic model with protons acceleration and diffusing out of the SNR interacts with the protons in molecular cloud.

2.2 Model of Secondary Gamma-ray and Neutrino emission

The interaction of CR protons with the molecular cloud leads to the production of charged $\pi^{\pm}$ and neutral pions π^0, respectively. The decay of neutral pions produces gamma-rays (γ) and charged pions produce neutrino (ν) fluxes. The fluxes of these gamma-rays and neutrinos depend on the CR proton spectra ($J_p(E_p)$), the molecular cloud density (n_H), and the production spectra of the secondary particles ($F_{\gamma,\,\nu}$) for a given energy of proton (E_p) (29). The spectra of

secondary particles is expressed as (29),

$$Q_{i,pp}(E_i) = cn_H \int_{\mathrm{E_i}}^{\infty} \sigma_{pp}(E_p) J_p(E_p) F_i\left(\frac{E_i}{E_p}, E_p\right) \frac{dE_p}{E_p}, \tag{2.1}$$

where, $i = \gamma$ or ν_f and f stands for neutrino flavours (e, μ). The CR protons are assumed to follow a power-law type distribution with an exponential cutoff above E_0, i.e., $J_p(E_p) = A_p E_p^{-\alpha} \exp(-E_p/E_0)$ TeV^{-1}. The power-law index α is typically chosen to be 2 based on Fermi's diffusive shock acceleration mechanism (1). The normalization constant A_p is related to the total energy ($E_{p,\mathrm{total}}$) of the CR protons by the relation $\int_{m_p}^{\infty} E_p J_p(E_p) \mathrm{d}E_p = E_{p,\mathrm{total}}$ and $\sigma_{pp}(E_p)$ is the energy dependent cross-section for the $p-p$ interaction (107). Eq. 2.1 can be qualitatively understood as follows. The function F_i gives the spectral distribution of secondaries for a single proton energy, and the product of $\sigma_{pp}(E_p) J_\mathrm{p}(E_\mathrm{p})$ provides us with an estimate of the secondaries created for a single proton target (29). To obtain the total number of secondaries created, we integrate Eq. 2.1 over E_p and multiply with the target density n_H. In particular, the upper limit of this integration is the maximum proton energy, $E_{p,\mathrm{max}}$ which depends on the magnetic field of the acceleration zone, confinement time and shock speed (1; 28). In case of SNR, this $E_{p,\mathrm{max}}$ is found to be a few PeV (28). Since, J_p has an exponential cutoff, the integrand drops very rapidly at high energies. Thus, the integration is not sensitive to the exact value of $E_{p,max}$.

Now, these secondary gamma-rays and the neutrinos are produced from the same $p-p$ interaction implying a connection between the final state fluxes of these secondaries. The secondary fluxes are connected by the following relation at $E_\gamma \approx 2E_\nu$ (68)

$$E_\gamma \frac{\mathrm{d}N_\gamma(E_\gamma)}{\mathrm{d}E_\gamma} \simeq e^{-d/\lambda_{\gamma\gamma}} \frac{2}{3} \sum_f E_{\nu_f} \frac{\mathrm{d}N_{\nu_f}(E_\nu)}{\mathrm{d}E_{\nu_f}}, \tag{2.2}$$

where, $\frac{\mathrm{d}N_\gamma(E_\gamma)}{\mathrm{d}E_\gamma}$ and $\frac{\mathrm{d}N_{\nu_f}(E_\nu)}{\mathrm{d}E_{\nu_f}}$ are the differential fluxes of gamma-rays and neutrinos of flavour f respectively. $\lambda_{\gamma\gamma}$ is the mean free path for the UHE gamma-rays in the Galactic radiation fields for a source located at a distance d. Therefore, one might predict the neutrino

flux from SNR using this multi-messenger connection, i.e., from gamma-ray observations.

The same secondary gamma-ray and neutrino flux at earth can also be estimated directly from Eq. 2.1 and given by

$$E_i^2 \frac{\mathrm{d}N_i}{\mathrm{d}E_i} = \frac{E_i^2 Q_{i,pp}(E_i)}{4\pi d^2}. \tag{2.3}$$

Since we are interested in detection of muon tracks with high energy neutrino detectors like IceCube, the muon flux at earth, $E_{\nu_\mu}^2 \frac{\mathrm{d}N_{\nu_\mu}}{\mathrm{d}E_{\nu_\mu}}$ is computed by assuming the flavour ratio 1 : 1 : 1. Note that neutrinos and anti-neutrinos are treated as same here. Clearly, for sources with known properties like n_H, E_0 etc., one may use Eq. 2.3, otherwise the Eq. 2.2 can be used for sources with only gamma-ray observations.

Neutrinos being weakly interacting in nature can propagate to earth without any losses. However, gamma-rays may undergo absorption during propagation. Absorption might effect the gamma-rays produced in SNRs and therefore, it is important to analyse this absorption process. This might also effect the cut-off energy, E_0 of the CR protons i.e., large absorption would allow large E_0 for the primary CR flux. The absorption is due to pair production on low energy photon backgrounds like cosmic microwave background (CMB) and the Galactic interstellar radiation field (ISRF). This is estimated by the factor $e^{-\tau_{\gamma\gamma}}$, where $\tau_{\gamma\gamma} = d/\lambda_{\gamma\gamma}$ is the attenuation of gamma-rays on the low energy photons (108). Larger the optical depth, larger is the absorption. The optical depth depends on the density and average energies of these low energy photons and the distance to the source d. Clearly, gamma-ray fluxes from further sources experience larger absorption. The CMB photons' number density is about 440 cm^{-3} and has an average energy of the order of 10^{-4} eV. This results in threshold energy for gamma-rays to interact with CMB photons at about 100 TeV (108). Since the CMB is uniform, the amount of absorption on CMB effectively depends only on the distance, d. On the other hand, the energies of Galactic ISRF photons are larger than that of CMB photons and the distribution of ISRF photons is highly non-uniform. Therefore, the threshold energy for ISRF is lower than 100 TeV and the absorption depends on the location of the source (108). For example, for a source located in a denser ISRF region will have larger absorption than that of a source located in a thinner ISRF.

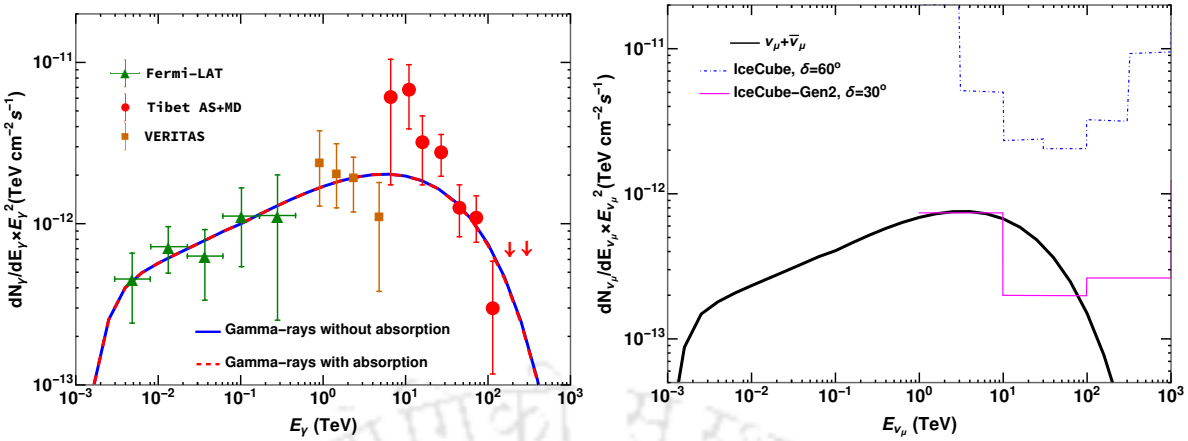

Figure 2.1: Hadronic gamma-rays (left), and muon neutrinos (right) from SNR G106.3+2.7. The high gamma-ray flux is fitted to the Tibet AS+MD data for a primary proton spectra with index 1.8 and the total energy of proton is 8×10^{47} erg. The low energy part of the spectra is fitted to the Fermi-LAT and VERITAS data. The absorption due to pair production on ISRF is negligible that results in overlapping of the gamma-ray flux with (red-dashed) and without absorption (blue). The distance to the source is taken to be 0.8 kpc. The correlated muon neutrino flux has been plotted (right) in addition to the detectors' sensitivities. The sensitivities of the neutrino detectors are chosen for declination, $\delta = 60^\circ$ for IceCube and $\delta = 30^\circ$ for IceCube-Gen2 which are closest available to the declination of this SNR. IceCube is not sensitive to this neutrino flux but IceCube-Gen2 has good sensitivity.

In the following, we use the method of direct calculation, i.e., Eqs. 2.1 and 2.3 for the secondary fluxes from the Galactic SNR sources, G106.3+2.7 and G40.5-0.5, as requisite properties are known from observations.

SNR G106.3+2.7

SNR G106.3+2.7 is one of the probable PeVatron source in which CR protons are accelerated due to the high shock speed (109). The distance of this source is 0.8 kpc and its shape is not perfectly spherical but a comet shaped SNR of length 14 pc and width of 6 pc (110). Recently, The Tibet ASγ Collaboration reported the discovery of gamma-rays above 10 TeV which extends upto 100 TeV gamma-rays (28). Further, the LHAASO collaboration also reported the discov-

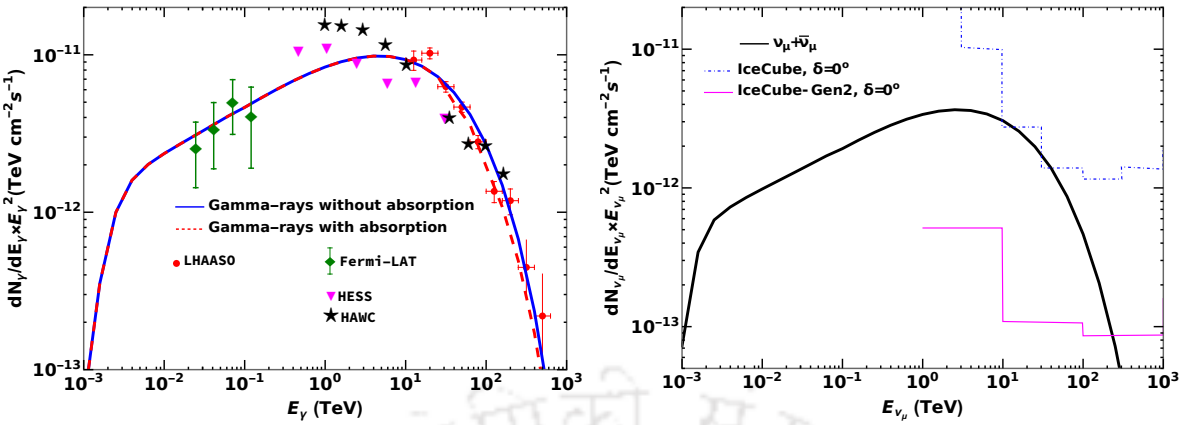

Figure 2.2: Hadronic gamma-rays (left), and muon neutrinos (right) from SNR G40.5-0.5. The gamma-ray flux is fitted to the LHAASO J1908+0621 data for a primary proton spectra with index 1.75 and the total energy of protons is 9×10^{49} erg. The distance to the source is taken to be 8.5 kpc. Gamma-rays above 10 TeV suffer tiny loss due to pair production on ISRF that is shown by the red-dashed curve while the gamma-ray spectra without absorption is shown by the blue curve. The corresponding neutrino flux has good sensitivity to IceCubt-Gen2 but weak to IceCube. The sensitivities of the neutrino detectors are shown for the declination, $\delta = 0^\circ$ closest available to the declination of this SNR.

ery of UHE gamma-rays from this spatial region from the source LHAASO J2226+6057 (22). These UHE gamma-rays are found to be spatially correlated with a molecular cloud and hence CR proton interactions are considered to be strong contenders (28). This is also supported by the hadronic interaction models developed for this source (111; 112). The probable density of the molecular cloud region is approximately 10 cm^{-3} and is consistent with the Bremsstrahlung radiation of electrons (113).

Figure 2.1 shows the model fitting of Tibet AS+MD gamma-ray data (left) and the corresponding neutrino emission in the model (right). The multi-messenger nature of the emission is crucial in fitting the gamma-ray spectra. The spectra data at the lower energies ($10^{-3} - 1$ TeV) are from Fermi-LAT (114), at intermediate energies ($1 - 10$ TeV) are from VERITAS (115), and at higher energies (~ 10 TeV) are taken from Tibet ASγ (28). The best fitting parameters $E_{p,\mathrm{total}}$, E_0 and α are such that both the normalisation and the slope of the spectra are well explained (see Table 2.1). We note the smaller $E_{p,\mathrm{total}}$ for this SNR and this may be due to low transfer of shock kinetic energy to accelerated protons (28). Moreover, the power law index, α in this object is found to be less than 2 from gamma-ray spectra fitting. This is in contrast

with the diffusive shock acceleration theory that predicts $\alpha = 2$. Extreme pressure at shock front might cause such efficient particle acceleration (see e.g., 116). These fit parameters are also consistent with (28). The source being located only at 0.8 kpc, the gamma-ray flux has negligible absorption during propagation to earth (28; 108).

Based on these parameter choices, we estimate the gamma-ray flux from this object. The resulting gamma-ray flux gives a good fitting to the gamma-ray data at both low energy and high energy. As mentioned, absorption during propagation is negligible which resulted in the overlap of the blue and red dashed curves. The associated neutrino flux is estimated using Eq. 2.3 and is found to be consistent with Eq. 2.2. This neutrino flux is found to be much below the detection sensitivity of IceCube. However, IceCube-Gen2 will be able to detect neutrinos from this source. Note that larger α would change the sensitivity.

SNR G40.5-0.5

SNR G40.5-0.5 is spatially overlapped with the UHE gamma-ray source LHAASO J1908+0621 (22). In earlier observations, this SNR was found be overlapped with extended TeV source MGRO J1908+06, detected by Milagro Galactic plane survey (117). This source was also detected by the H.E.S.S. telescope in gamma-rays (118). UHE gamma-rays were also discovered from MGRO J1908+06 source by the HAWC detector (119) that makes SNR G40.5-0.5 a plausible CR particle accelerator. The source distance is uncertain and CO Molecular-line emission infers a source distance of approximately 3.4 kpc (120) but at a larger distance of 5.5 to 8.5 kpc using $\Sigma-$D relation (121). The mean gas density in the associated molecular cloud is ~ 45 cm^{-3} taking the source distance 8 kpc (122) and the source linear size at this distance would be approximately 60 pc.

Model fit of the gamma-ray data of this object is shown in the left panel Fig. 2.2 for the parameters listed in Table 2.1. The low energy ($10^{-3} - 10^{-1}$ TeV) data are from Fermi-LAT (123; 22) and at high energies ($> 10^{-1}$ TeV) data are taken from HESS (124), HAWC (119), and LHAASO (22). The parameters listed in Table 2.1 can well explain these multi-messenger gamma-ray data. Note that $E_{p,\mathrm{total}}$ in this SNR is found to be larger than that of SNR G106.3+2.7. However, the power-law index α is found to be similar to that of G106.3+2.7.

Parameters	SNR G106.3+2.7	SNR G40.5-0.5
$E_{p,\mathrm{total}}$ (erg)	8×10^{47}	9×10^{49}
E_0 (TeV)	6×10^2	4×10^2
α	1.8	1.75

Table 2.1: Model parameters chosen for the two prototype SNRs. These parameters give the best fit to the observed gamma-ray data of these objects. SNR G106.3+2.7 is located at 0.8 kpc and G40.5-0.5 is located at 8.5 kpc. The target gas density, n_H for SNR G106.3+2.7 is 10 cm^{-3} and for G40.5-0.5 is 45 cm^{-3}.

Since this source is farther away, gamma-rays suffer larger absorption due to pair production on ISRF compared to G106.3+2.7. However, this absorption is still tiny and negligible; and shown by the red dashed curve. The corresponding neutrino flux is estimated using Eq. 2.3 and shown in the right panel. This neutrino flux estimation is found to be consistent with Eq. 2.2. To check the IceCube neutrino sensitivity, we look into the closest available declination of IceCube, i.e., $\delta = 0^\circ$ to the source declination. The neutrino flux has weak sensitivity to IceCube but has reasonably good sensitivity to IceCube-Gen2. Hence, this object sets an outstanding goal to neutrino detection in IceCube-Gen2 as the neutrino flux is much above the detection sensitivity.

In the following, we investigate the parameter space of Galactic PeVatrons allowed by gamma-ray observations (28; 22) and discuss the future detection prospects with gamma-ray and neutrino detectors.

2.3 Detection prospects of Galactic PeVatrons

In the preceding sections, we have computed the expected muon neutrino flux in detail for the two prototype sources. The neutrino flux estimates of such objects show that the flux might be detected by the current and upcoming generation of IceCube experiment. This motivates one to look further into the detection prospects of these Galactic objects. Based on this, we make estimate of future detection of such sources motivated by the two detected prototype SNRs. We also estimate the expected neutrino events in IceCube from the LHAASO catalog sources (see Table 2.2 and (22)) to check the consistency of our chosen parameter space.

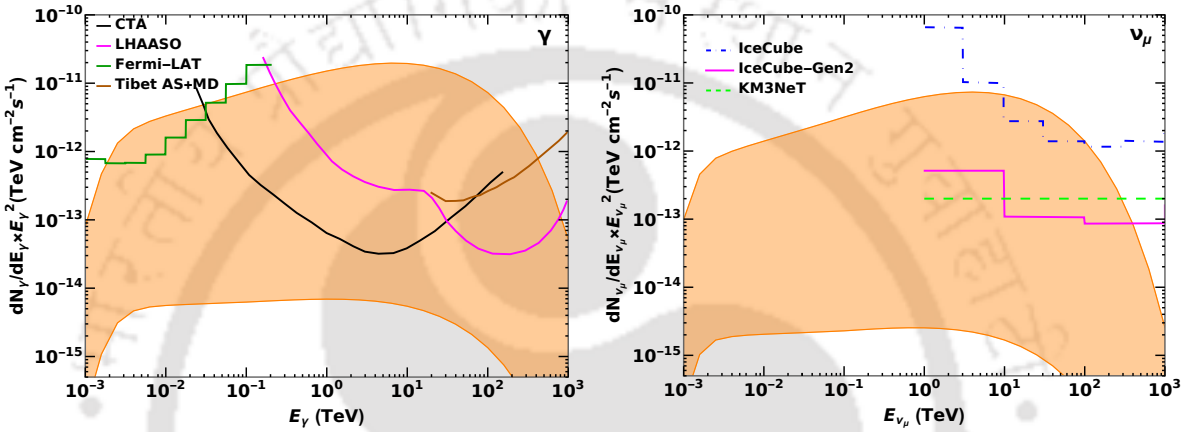

Figure 2.3: *Left:* Detection prospects of gamma-rays from Galactic SNR at 10 kpc with different gamma-ray telescopes. The curves in different colours shows the sensitivities of Fermi-LAT (green) (125), LHAASO (magenta) (126), Tibet AS+MD (brown) (127) and CTA (black) (24). The orange band shows gamma-ray flux for the parameter space based on the observations of SNR G106.3+2.7 and G40.5-0.5. This shows that the high energy gamma-ray detectors will probe large fraction of this parameter space for SNR at 10 kpc. *Right:* Corresponding detection prospects at high energy neutrino detectors. The sensitivities of IceCube, IceCube-Gen2 and KM3NeT are shown by the blue dot-dashed, magenta and green lines respectively (128; 25; 73). These neutrino detectors will also probe some part of the parameter space.

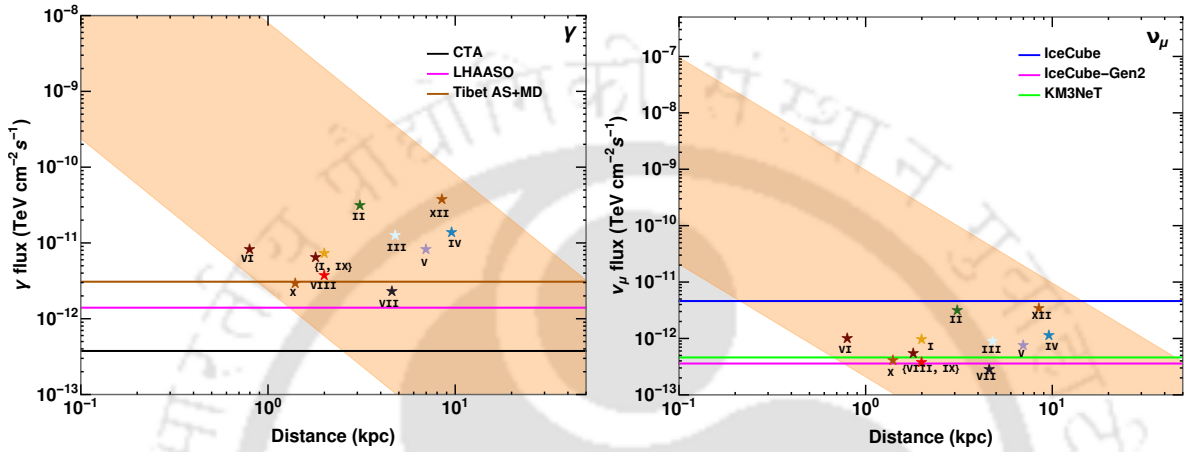

Figure 2.4: *Left:* Detection horizon of SNRs for different gamma-ray telescopes. The orange band show integrated flux above 1 TeV as a function of distance (kpc) for the same parameter as in Fig. 2.3.. The horizontal lines show the detectors sensitivities (126; 125; 24; 127). All these gamma-ray telescopes are capable of probing a large part of the parameter space . The upcoming CTA will probe sources as far as 50 kpc. *Right:* Corresponding detection horizon of different neutrino detectors. The orange band shows the energy integrated ($10^1 - 10^2$ TeV) ν_μ flux as a function of distance (kpc) for the same parameter as in Fig. 2.3. The horizontal lines show the energy integrated sensitivities (corresponds to $\delta = 0^\circ$ in the energy range $10^1 - 10^2$ TeV) of IceCube (blue), IceCube-Gen2 (magenta) and KM3NeT (green) (128; 25; 73). This shows that the maximum reach of IceCube is about 10 kpc whereas for IceCube-Gen2 and KM3NeT, the maximum reach is about 50kpc. The stars of different colours in both panels show the energy integrated γ and ν_μ flux for the sources listed in Table 2.2.

In order to investigate the detection possibility, a range of CR proton spectra parameters is considered, motivated by the observations (22; 28). This parameter space is obtained by varying the total energy $E_{p,\mathrm{total}}$ ($10^{48} - 10^{51}$ erg) and the power law index α ($1.7 - 2.0$) based on the gamma-ray observations of SNR G106.3+2.7 and G40.5-0.5. While varying the parameters, we choose to keep the cut-off energy, E_0 fixed as both objects show similar values. The power law index, α is also found to be similar in these two objects, i.e., about 1.8. However, this index is in contrast with the diffusive shock acceleration theory which predicts a power law index $\alpha = 2.0$ (1). Such smaller value of α is possibly due to very efficient proton acceleration in these objects (116; 129). Indeed, observation of neutrinos from such sources by the neutrino detectors in question will be crucial to probe the softer spectra i.e., large α. Therefore, the variation of α is considered in the range $(1.7 - 2.0)$.

For the parameter space discussed above, gamma-ray and muon neutrino fluxes are estimated for an SNR at 10kpc. The left panel in Fig. 2.3 shows the gamma-ray flux and the right panel shows the corresponding muon neutrino flux. The orange band in both panels corresponds to the uncertainty in the parameters $E_{p,\mathrm{total}}$ and α. In the gamma-ray plot, the sensitivities of different gamma-ray telescopes operating at different energy ranges have been shown. At low energy, Fermi-LAT is capable of probing a small part of the SNR parameter space. Interestingly, the high energy gamma-ray telescopes like LHAASO, Tibet AS+MD and CTA (upcoming) will be able to probe a much larger fraction of the SNR parameter space.

In addition to the correlated neutrino flux, high energy neutrino detectors' sensitivities have also been plotted in right panel of Fig. 2.3. The blue dot dashed line corresponds to the sensitivity of IceCube (128), the magenta line shows the sensitivity of IceCube-Gen2 (25) and the green-dashed line is the sensitivity of KM3NeT (73). This shows that IceCube is hardly sensitive to such neutrinos from sources at 10 kpc. However, IceCube-Gen2 and KM3NeT might be able to detect these neutrinos from SNRs provided the neutrino fluxes produced are $> (10^{-13})$ TeVcm^{-2}s^{-1} above 10 TeV. Nevertheless, these future detectors together with the gamma-ray telescopes can put stringent constraints on a significant region of the SNR parameter space. For this, the UHE gamma-rays detected by LHAASO (22) might assist to scan this parameter space and help us to understand the future detection possibilities.

The PeVatron sources detected in gamma-rays by LHAASO (22) are listed in Table 2.2. The estimation of neutrinos from these sources is not straightforward due to the following rea-

Sl No.	LHAASO sources	IceCube events, $\mathcal{N}_{\nu_\mu}$ (5 yr)
I	J0534+2202	2.74
II	J1825-1326	0.28
III	J1839-0545	0.08
IV	J1843-0338	4.68
V	J1849-0003	2.82
VI	**J1908+0621**	4.55
VII	J1929+1745	0.85
VIII	J1956+2845	1.33
IX	J2018+3651	2.33
X	J2108+5157	1.05
XI	J2032+4102	1.07
XII	**J2226+6057**	2.57

Table 2.2: Expected number ν_μ events at IceCube for the LHAASO catalogue. The sources J2226+6057 and J1908+0621 are associated with SNR G106.3+2.7 and G40.5-0.5 respectively. The conventional atmospheric ν_μ flux produces a background of $\mathcal{O}(10^4)$ events on top of these events.

sons. All of these objects might not be pure hadronic PeVatrons and therefore might not produce much neutrinos (101). In fact, the source J0534+2202 is found to be associated with the Crab nebula and most of these gamma-rays are expected to be of leptonic origin except for the tail of the spectra which might be hadronic (91). Therefore, we use the gamma-ray-neutrino correlation given by Eq. 2.2 to estimate the maximum possible neutrinos from the Crab considering these gamma-rays to be completely hadronic. For the remaining LHAASO sources, association of any molecular cloud is not well known (22) and model of CR interacting with molecular cloud might not be appropriate. In addition, only the fluxes at 100 TeV are available for these sources (91). Thus, we assume a proton power law index $\alpha = 1.8$ and normalize the gamma-ray flux at 100 TeV to estimate the neutrino fluxes from these objects (22).

To analyze the detection possibility of these sources with IceCube, we have computed the number of ν_μ tracks at IceCube by the following formula

$$\mathcal{N}_{\nu_\mu} = T \int_{0.1\ TeV}^{100\ TeV} \mathrm{d}E_{\nu_\mu} \frac{\mathrm{d}N_{\nu_\mu}}{\mathrm{d}E_{\nu_\mu}} A_{eff}(\delta) \tag{2.4}$$

where, T is the observation time and $A_{eff}(\delta)$ is the declination dependent effective area (130). The declination of the source plays an important role in the detection of neutrinos. Therefore, the declination of each source in Table 2.2 is taken into account for the calculation of IceCube events. The number of events for 5 years are shown in Table 2.2. The events are found to be so tiny that they might be buried deep in the large conventional atmospheric background ($\mathcal{O}(10^4)$). This explains the non-observation of neutrinos till date from such SNRs (131).

It is clear from the above analysis that the source distance is also an important parameter for the detection of these PeVatron sources by gamma-ray and neutrino telescopes. Fig. 2.4 shows the energy integrated gamma-ray (left) and muon neutrino (right) flux as a function of source distance (in kpc). The orange band in both panels corresponds to the uncertainty in the SNR parameters, $E_{p,\mathrm{total}}$ and α as discussed above. The gamma-ray flux is integrated above 1 TeV following the best sensitive energy ranges of the different detectors. The horizontal lines in the left plot are the integral sensitivities for CTA, LHAASO and Tibet AS+MD. All these gamma-ray telescopes are well capable of detecting SNRs in the galaxy. In future, CTA will probe vast region of the SNR parameter space.

Similarly, detection horizons of different high energy neutrino telescopes like IceCube, IceCube-Gen2 and KM3NeT are shown in the right panel of Fig. 2.4. The orange band shows the integrated ν_μ flux in the range $(10 - 10^2)$ TeV for the parameter space discussed above. Energy integrated sensitivities in the range $10^1 - 10^2$ TeV of IceCube, IceCube-Gen2 and KM3NeT for declination angle $\delta = 0^\circ$ have also been plotted. This plot shows that the maximum reach of IceCube is about 10 kpc whereas for IceCube-Gen2 and KM3NeT the maximum reach is about 50kpc. However, for the lower limit of the neutrino flux, the detection horizon for IceCube falls below 200 pc and for IceCube-Gen2, KM3NeT, it falls below 1 kpc.

The gamma-ray and neutrino fluxes produced by the LHAASO sources (22) listed in Table. 2.2 are also shown in Fig. 2.4 by the star symbols in different colours. All these sources are above the sensitivities of LHAASO and CTA, while they are below the sensitivity of IceCube. Interestingly, the upcoming neutrino detectors IceCube-Gen2 and KM3NeT will be able to detect neutrinos from such SNRs. As pointed out earlier, all of these sources might not be pure hadronic PeVatrons (101). Therefore, the neutrino fluxes shown here can only be treated as upper limits. As mentioned earlier, the Crab gamma-ray fluxes are expected to be mostly leptonic (91). Thus, neutrino emission from Crab might be faint and not detectable. Even for the purely hadronic model, the neutrino flux from Crab is found to be below IceCube sensitivity. Indeed, IceCube-Gen2 and KM3NeT will be able to constrain the hadronic nature of these sources.

Note that the detection of neutrinos strongly depends on the source declination, δ. The sensitivities shown here for the neutrino detectors are for $\delta = 0^\circ$. For declination angle other than this, the sensitivity would be lower and some of the sources might fall below the detectors' sensitivities. Nevertheless, the upcoming neutrino detectors might still be able to detect some PeVatrons and unravel the nature of these sources, i.e, hadronic or leptonic.

2.4 Summary and Conclusion

The 12 sources detected by LHAASO in TeV gamma-rays provide evidence of CR acceleration to very high energies. If these gamma-rays are created by hadronic interaction of CR protons with background protons, they should be accompanied by neutrinos. However, no neutrinos are expected for leptonic origin of these gamma-rays. Therefore, detection of neutrinos will

play a crucial role to identify the nature of these sources. Based on the gamma ray data, we have estimated the plausible neutrino fluxes from these sources and test their detectability in IceCube, IceCube-Gen2 and KM3NeT.

These objects detected by LHAASO are found to be spatially associated with SNRs and pulsars. CRs accelerated in SNRs and pulsar interacting with any nearby molecular cloud can be the origin of these gamma-rays. In fact, for two of these sources, gamma-rays are found to be originated in the molecular clouds of SNR G106.3+2.7 and G40.5-0.5. However, for some of these sources no molecular clouds have been identified yet. On the other hand, one of these objects is found to be connected to the Crab nebula where the emission is expected to be mostly leptonic. Therefore, detection of the associated neutrino signal is important to probe the nature of these sources.

Using the gamma-ray data of SNR G106.3+2.7 and SNR G40.5-0.5, we have developed a $p-p$ interaction model and estimated the neutrino fluxes from these objects. The age of SNR G106.3+2.7 is $\sim$ 10 kyr, while for SNR G40.5-0.5, it is in between 10-20 kyr (see e.g., 22). For these two sources, model parameters, i.e., CR proton energy $E_{\rm p,total}$, spectral index α, the cutoff energy E_0 are listed in Table 2.1. We found α and E_0 to be similar for both SNRs (1.8 and $\sim$ 500 TeV) but their $E_{\rm p,total}$ is very different. The asymmetry in the source geometry and cloud morphology can affect the escape of the CR protons and may cause this difference in the total energy in CR protons (113). Our chosen spectral indices are harder compared to the standard diffusive shock acceleration model, which predicts $\alpha = 2$ (132). However, if the shock compression ratio is very high then the CR spectral index can be harder; i.e. $\alpha = 1.5$ (133) as also predicted using nonlinear diffusive shock acceleration mechanism (129). The neutrino flux from SNR G106.3+2.7 is found to be below IceCube sensitivity and SNR G40.5-0.5 has poor sensitivity to IceCube. This also explains the non-observation of neutrinos from these two sources. However, both these sources appeared to be sensitive to IceCube-Gen2. Hence, IceCube-Gen2 will be able to probe the hadronic channel in these objects.

Based on the analysis of these two sources, we have derived the probable parameter space of this SNR + molecular cloud model. The parameter space has been constructed considering uncertainties in the model parameters, i.e., spectral index, α and total energy, $E_{p,\rm total}$. The upper limit of $\alpha = 2.0$ is considered based on the standard CR acceleration mechanism. The wide variation in $E_{p,\rm total}$ is taken based on the observation the two SNR G106.3+2.7 and G40.5-

0.5. Future neutrino telescopes (IceCube-Gen2 and KM3NeT) will be able to probe a large portion of this parameter space, provided the events are located within 50 kpc. However, the best possibility of detection indeed lies within a region of 10 kpc which is inferred by the LHAASO sources.

We have also estimated the neutrino flux from Crab nebula based on the gamma-ray spectra observed by LHAASO. Most of these gamma-rays are expected to be of leptonic origin. Thus, the neutrino signal is expected to be weak. The neutrino flux from Crab is found to be below IceCube sensitivity, even for the purely hadronic model. Neutrino fluxes for the remaining LHAASO sources are estimated based on the gamma-ray data and assuming a power law index 1.8. All these sources are found to be below IceCube sensitivity but many of them might be detectable in IceCube-Gen2 and KM3NeT.

Further, primary and secondary electrons accelerated at the shock regions, can also contribute towards the multi-wavelength radiation. Their synchrotron radiation depends on the magnetic field and hence this can be tuned to get the radio to X-ray spectrum consistent with the observations. The inverse-Compton radiation can be another channel for the gamma-ray spectrum in the UHE regime. In this work we are mainly interested in estimating the maximum neutrino flux from SNRs, hence we have not discussed the radiation due to electrons. However, contamination from the leptonic channel of the concentric PWN cannot be discarded in these sources (134; 135; 136)

To conclude, we have analysed the detection prospects of the LHAASO sources and also similar possible sources in the Galaxy. IceCube might be able to detect closer objects within 1 kpc but for extremely neutrino bright sources the detection horizon extends up to 10 kpc. The future detectors KM3NeT and IceCube-Gen2 can have detection sensitivity up to 50 kpc. Such detection will probe the nature of Galactic PeVatrons.

In this chapter, we have estimated the neutrino fluxes from 12 Galactic PeVatrons detected by the LHAASO experiment, considering the gamma-rays are created in interaction of shock accelerated protons in SNR with nearby molecular cloud. Detection of neutrinos in future by detectors like IceCube-Gen2 and KM3NeT will constrain this hadronic interaction scenario as well as particle acceleration in such objects. Particle acceleration to PeV energies in SNRs occurs in a long timescale which is about the lifetime of SNRs. However, such acceleration can also be achieved in new born SNe through interaction of ejected material with dense circumstel-

lar material. In the next chapter, we discuss the secondary gamma-ray and high energy neutrino emission in such scenarios for different types of CCSNe.

This page was intentionally left blank.

Chapter 3

Point sources: Young Supernovae

In this chapter, we analyse a different category of point source, the young Supernovae (YSNe). These YSNe pertain to the phenomenon of interaction between the material ejected during a supernova event and the surrounding dense circumstellar medium (CSM). This interaction typically transpires shortly after the supernova explosion, often within a matter of days, and can result in the acceleration of protons through shock processes. These accelerated protons, upon colliding with the lower-energy protons within the CSM, can generate secondary particles, including high-energy neutrinos and gamma-rays. In the subsequent sections, we undertake the task of estimating the fluxes of these secondary particles for various types of young Supernovae. Additionally, we evaluate the potential for detecting different classes of these YSNe utilizing both presently available and forthcoming gamma-ray and high-energy neutrino detectors.

3.1 Interacting circumstellar medium

The astrophysical community has been periodically intrigued by distinctive observations of core collapse supernovae (CCSNe), which arise as a consequence of the demise of stars. Such

distinct features arising due to varying mass and metallicity of stars lead to classification of CCSNe into various categories such as IIn, II-P, IIb, II-L, Ib and Ic. In addition, numerous multi-wavelength observations in the last few decades have revealed presence of dense circumstellar medium (CSM) around such objects.

The dense CSM is made up of matter deposited through stellar winds further enriched as the progenitor star loses mass via wind and/or violent outbursts (e.g., see Ref. (37) and references therein). The CSM was previously thought to originate from stars losing their mass through steady stellar winds. However, recent SN observations have challenged this traditionally accepted picture (see e.g. (37)). It is now clear that substantial and impulsive mass losses occur in at least 10% of massive stars within one year from the core collapse.

The stellar progenitor of SN2009ip, whose repeated eruptions occurred in the years before explosion, is the best studied example among Hydrogen (H)-rich massive stars (137). The progenitor of this SN was a Luminous Blue Variable (LBV) star. An LBV is a massive star that can have sporadic, violent mass loss events and exhibits mass loss rate as high as 10 $M_{\odot}yr^{-1}$ (138; 139; 140; 141). LBVs were previously thought to be a transitional phase of stellar evolution. However, several recent works have shown that they can be progenitors of Type IIn SNe (see e.g. (142) and references therein). The interaction between the CSM and the SN ejecta is evident from the observation of narrow, symmetric emission lines in “flash" spectroscopy of SNe. This might be due to the photo-ionization of the CSM occurring during the progenitor mass loss phase before explosion, see e.g. (143; 144). UV/optical excesses observed in SNe at early times also hint towards such mass loss phenomena, see e.g. (145).

The interaction of the SN ejecta with this dense CSM may lead to the production of secondary particles, such as neutrinos and gamma-rays, via inelastic proton-proton ($p-p$) collisions (29; 146; 147; 148; 149; 150; 151; 152; 153; 154; 155). In most cases, the interaction of the SN ejecta with the CSM is dominant during the early stages of the SN evolution, for a few months to a few years (38). After this preliminary phase, the interaction weakens due to the fall in the CSM density (156). We focus on the high-energy particle emission during this initial SN phase and refer to it as “Young Supernova (YSN)”. Note that, a clear distinction between YSNe and SN remnants (SNRs) is not straightforward (157; 158; 159). In a SNR, the SN ejecta interacts with and sweeps up the far away CSM or the Interstellar Medium (ISM). For a sufficiently old SNR (1 kyr), the medium is significantly less dense and has a density of

$1 - 10^3$ cm^{-3}. While the dense CSM during the YSN phase can have densities in the scale of $10^9 - 10^{12}$ cm^{-3} (160; 104; 35; 36). Thus the largest contribution to the secondary particle emission is reasonably considered to originate from the YSN phase. These high-energy neutrinos emitted from SNe are possibly detectable by neutrino telescopes like the IceCube Neutrino Observatory (33; 36; 161; 162) and from YSNe, gamma-rays could also be observed by Fermi-LAT (163; 75; 77) and the Cerenkov Telescope Array (CTA) (164).

In the following, we consider YSNe of different Types IIn, II-P, II-L and Ib/c, and explore the related gamma-ray and neutrino emission and investigate their detection prospects with Fermi-LAT (163; 77) and CTA (164) as well as IceCube (30; 48), IceCube-Gen2 (25), and Km3NeT (73).

While neutrinos produced in YSNe propagate undisturbed to Earth, gamma-rays undergo energy losses as they interact with low energy photons ($\gamma\gamma \longrightarrow e^- e^+$) and ambient matter ($\gamma N \longrightarrow N e^- e^+$, where N is nucleus) in the source (34). In addition, over cosmic scales ($\sim$Gpc), the Extra-galactic Background Light (EBL) absorption further affects the gamma-ray flux expected at Earth (165; 166), becoming significant for the diffuse SN emission, but negligible for point source detection in the local universe (i.e., below $\sim$ 10 Mpc).

One can estimate the fluxes of these secondary particles by modelling the necessary ingredients such as the accelerated proton spectrum, the CSM density, the shock profile and the propagation effects based on different SN observations. In the following section, we discuss the model that we have adopted for the estimation of the secondary fluxes.

3.2 Neutrino and gamma-ray production in young supernovae

In this Section, we model YSNe interacting with the CSM in the early phase after the explosion. We focus on YSNe about a year old and develop a model for the shock-CSM interaction, describing the creation of secondary particles: neutrinos and anti-neutrinos [1] and gamma-rays.

[1]Note that we do not distinguish between particles and antiparticles in the following and use "neutrinos" to indicate both species.

3.2.1 Model setup

The material expelled by the massive star at the end of its life forms the CSM. The CSM consists of shells of mostly light elements like H or helium (He). The massive star eventually explodes in the form of a core-collapse SN [2]. The SN shock and the expanding ejecta interact with the surrounding CSM. Charged particles (electrons and protons) in the shocked CSM are accelerated to relativistic energies via Fermi's diffusive shock acceleration (168; 169; 1). In particular, we are interested in high energy processes with dominant neutrino production, hence we focus on inelastic $p-p$ collisions. Here, relativistic protons collide with the non-relativistic protons (inelastic $p-p$ collisions) in the CSM and produce a large number of π and η mesons. Secondary neutrinos, electrons and gamma-rays are produced from the decay of π and η mesons (170; 171; 29; 35; 40; 36). High energy protons can also undergo photo-hadronic ($p\gamma$) interactions with low energy photons in the CSM. However, the energy loss due to this process is negligble and hence neglected (see Appendix A).

The CSM shell is assumed to be spherically symmetric with an effective inner radius $r_{\rm in}$ and outer radius $r_{\rm out}$. The inner radius is defined as $r_{\rm in} = \max[r_{\rm bo}, r_{\rm e}]$ (33). The shock breakout radius[3], $r_{\rm bo}$, corresponds to the beginning of shock acceleration, and $r_{\rm e}$ is the radius of the stellar envelope. Thus $r_{\rm in}$ may differ according to the SN Type (see Sec. 3.3 for details). The outer radius or size of the CSM shell also depends on the SN Type. Given the assumption of spherical symmetry, the radial dependence of the CSM mass density can be modelled in the following way (159):

$$\rho_{\rm CSM}(r) = \frac{\dot{M}_{\rm W}}{4\pi r_{\rm in}^{w} v_{\rm w}} \left(\frac{r_{\rm in}}{r}\right)^{w}. \tag{3.1}$$

Here w is the power-law index of the CSM density profile (e.g., $w = 2$ for a wind-like CSM—see, e.g., Ref. (38)), $\dot{M}_{\rm W}$ is the mass loss rate of the progenitor star and $v_{\rm w}$ is the wind velocity. The radial dependence is provided by the propagation of the shock, r being the shock radius. The number density of the protons in the CSM ($n_{\rm CSM}(r) = \rho_{\rm CSM}(r)/m_{\rm p}$) also varies accordingly.

[2] We focus on core-collapse SNe as the vast majority of Type Ia SNe do not exhibit a dense CSM (with the notable exception of e.g., (167)).

[3] The shock breakout radius corresponds to the optical depth, $\tau = c/v_{\rm sh}$, of the material through which the shock propagates, where $v_{\rm sh}$ is the shock velocity introduced in the following (172).

Thus, the CSM at the inner radius is $n_{\rm in,CSM} = \rho_{\rm CSM}(r_{\rm in})/m_p = \dot{M}_{\rm W}/(4\pi m_p r_{\rm in}^2 v_{\rm w})$, where m_p is the mass of the proton.

A fraction of the protons injected in the shocked region will be accelerated to high energies and in turn produce secondary particles while interacting with the CSM protons. To model this, the SN shock is assumed to expand spherically in the CSM and has a power law dependence on the radius. The velocity of the shock ($v_{\rm sh}$) expanding in the CSM varies slowly with radius (38):

$$v_{\rm sh}(r) = v_{\rm in}\left(\frac{r}{r_{\rm in}}\right)^{\alpha}, \tag{3.2}$$

where $v_{\rm in}$ is the shock velocity at $r_{\rm in}$ and α characterises the shock velocity profile. The index α can be expressed in terms of the power law indices of the CSM and SN ejecta density profiles and is usually found to be negligible, i.e. the shock velocity is nearly constant over the length of the CSM shell during the early phase of the YSN. For more details on the choice of α, see Ref. (40). In our YSN computations, we assume $\alpha = 0$ implying $v_{\rm sh} = v_{\rm in}$.

To estimate the secondary particle population, we need the injection spectra of the accelerated protons in the shocked region. We assume a power law distribution between the maximum ($E_{\rm p,max}$) and minimum ($E_{\rm p,min}$) proton energy for the injection spectra (35):

$$N_{\rm p}^{\rm inj}(E_{\rm p}, r) \propto E_{\rm p}^{-\alpha_{\rm p}} \exp\left(-\frac{E_{\rm p}}{E_{\rm p,max}(r)}\right), \tag{3.3}$$

where $E_{\rm p}$ is the proton energy, $\alpha_{\rm p}$ is the power law index and it is assumed to be equal to 2 unless otherwise mentioned. The choice $\alpha_{\rm p} = 2$ is motivated by diffusive shock acceleration theory (1). The normalization of the injected spectra is obtained from the energy budget of the shock [$E_{\rm K} = (9\pi/8) m_{\rm p} v_{\rm sh}^2 r^2 n_{\rm CSM}(r)$, energy per unit radius]. A fraction of this energy, $\varepsilon_{\rm p}$, is transferred to the charged particles (protons) confined in the shocked region due to the presence of a strong magnetic field and thus accelerates protons to high energies. The fraction $\varepsilon_{\rm p}$ is a free parameter of the problem and may depend on the SN Type. This is due to the fact that CSM density, ejecta kinetic energy and progenitor mass vary for different SN Types (173). The minimum proton energy $E_{\rm p,min}$ is taken as the proton rest mass $m_{\rm p}$. The maximum energy ($E_{\rm p,max}$) of the accelerated protons depends on the different loss processes competing with the acceleration time scale ($t_{\rm acc} = 6E_{\rm p}c/eBv_{\rm sh}^2$) (174; 35), B being the mag-

netic field strength. The magnetic field is inversely proportional to the shock radius r and it is $B = 3/2(4\pi\varepsilon_B m_p n_{in,CSM} v_{sh}^2)^{1/2}(r_{in}/r)$, where ε_B is the fraction of the post shock thermal energy that goes into the magnetic field (35; 175; 176). A detailed analysis on the effects of magnetic field on $E_{p,max}$ can be found in Ref. (177).

The energy losses suffered by relativistic protons mainly come from two competing processes, due to the adiabatic expansion of the shock shell and the $p-p$ interactions with the CSM protons. The adiabatic loss time scale or the dynamical time scale is $t_{ad} \sim t_{dyn} = r/v_{sh}$ and the $p-p$ collision time scale is $t_{pp} = [4\kappa_{pp}\sigma_{pp} n_{CSM}(r)c]^{-1}$, where $\kappa_{pp} = 0.5$ is the proton inelasticity and σ_{pp} is the energy dependent $p-p$ interaction cross-section (178). t_{pp} (35; 36)In addition, protons undergo other energy loss processes, as detailed in Appendix A. Thus, $E_{p,max}$ can be estimated from $t_{acc} = 6E_{p,max}c/eBv_{sh}^2 = \min[t_{pp}, t_{ad}]$ and changes according to the radial evolution of the background environment.

The radial evolution of the steady state proton number, $N_p(E_p, r)$ is described by the following equation (179; 168; 180; 35; 36):

$$\frac{\partial N_p(E_p,r)}{\partial r} + \frac{N_p(E_p,r)}{v_{sh} t_{pp}(r)} - \frac{\partial}{\partial E_p}\left[\frac{E_p N_p(E_p,r)}{r}\right] = N_p^{inj}(E_p,r)\,, \tag{3.4}$$

where the second term on the left hand side corresponds to energy losses via $p-p$ collisions and the third term stands for adiabatic losses. This primary steady state proton number drives the production of the secondary neutrinos and gamma-rays. The time evolution of the fluxes can be probed from the relation betweeen the shock radius and the shock velocity: $r = v_{sh}t$.

3.2.2 Gamma-ray production

Gamma-rays can be produced through $p-p$ interactions via decay of neutral π and η mesons, with the following decay channels: $\pi^0 \longrightarrow 2\gamma$, $\eta \longrightarrow 2\gamma$, $\eta \longrightarrow 3\pi^0$, $\eta \longrightarrow \pi^+\pi^-\pi^0$, and $\eta \longrightarrow \pi^+\pi^-\gamma$ (29). The contribution from π^0 meson dominates over the contribution from η meson (see e.g., 29). The radial evolution of gamma-rays with energy E_γ produced in $p-p$

collisions can be computed as follows (34; 32):

$$\frac{\mathrm{d}N_\gamma(E_\gamma,r)}{\mathrm{d}r}+\frac{N_\gamma(E_\gamma,r)}{v_{\rm sh}t_{\rm esc}}=N_\gamma^{\rm inj}(E_\gamma,r), \tag{3.5}$$

where $t_{\rm esc}=r/4c$ is the escape time of secondary particles. The factor 4 corresponds to the compression of the CSM due to shock pressure (168). The source term, $N_\gamma^{\rm inj}(E_\gamma,r)$, below $E_{\rm p}=0.1$ TeV is given by (29)

$$N_\gamma^{\rm inj}(E_\gamma,r)=2\frac{\tilde{\eta}}{K_\pi}\frac{4cn_{\rm CSM}(r)m_{\rm e}}{v_{\rm sh}m_{\rm p}}\int_{E_{\rm min}}^{\infty}\frac{\mathrm{d}E_\pi}{\sqrt{E_\pi^2-m_\pi^2}}\sigma_{\rm pp}\left(E_{\rm p}\right)N_{\rm p}\left(E_{\rm p}\right)\ , \tag{3.6}$$

where $E_{\rm p}=m_{\rm p}+E_\pi/K_\pi$ and $E_{\rm min}=E_\gamma+m_\pi^2/E_\gamma$. Above $E_{\rm p}=0.1$ TeV,

$$N_\gamma^{\rm inj}(E_\gamma,r)=\frac{4cn_{\rm CSM}(r)m_{\rm e}}{v_{\rm sh}m_{\rm p}}\int_{m_{\rm p}}^{\infty}\mathrm{d}E_{\rm p}\frac{\sigma_{\rm pp}(E_{\rm p})}{E_{\rm p}}N_{\rm p}(E_{\rm p},r)F_\gamma\left(\frac{E_\gamma}{E_{\rm p}}\right)\ , \tag{3.7}$$

with $F_\gamma\left(E_\gamma/E_{\rm p}\right)$ being the gamma-ray production rate, and E_γ the gamma-ray energy. The parameters K_π and $\tilde{\eta}$ are free parameters, used for connecting the injection rates above energy $E_{\rm p}=1$ TeV.

The total gamma-ray flux observed at Earth from a source at luminosity distance $d_{\rm L}$ is given by:

$$\begin{aligned}E_{\gamma,\rm obs}^2\Phi_\gamma(E_{\gamma,\rm obs})&=\frac{e^{-\tau_{\gamma,\rm EBL}(E_\gamma,z)}}{4\pi d_{\rm L}^2}E_\gamma^2\phi_\gamma^{\rm s}(E_\gamma)\\&=\frac{e^{-\tau_{\gamma,\rm EBL}(E_\gamma,z)}}{4\pi d_{\rm L}^2}\int_{r_{\rm in}}^{r_{\rm max}}\mathrm{d}r\frac{E_\gamma^2N_\gamma(E_\gamma,r)e^{-\left(\tau_{\gamma\gamma}+\tau_{\rm BH}\right)}}{m_{\rm e}c^2t_{\rm esc}v_{\rm sh}}\ ,\end{aligned} \tag{3.8}$$

where $E_\gamma=(1+z)E_{\gamma,\rm obs}$, z is the cosmological redshift and $\phi_\gamma^{\rm s}$ is the gamma-ray flux at source. The maximum shock radius, $r_{\rm max}$ corresponds to the end of particle production (see Sec. 3.2.3 for details). Here, $\tau_{\gamma\gamma}$ and $\tau_{\rm BH}$ are the optical depths for gamma-gamma and Bethe-Heitler interactions, respectively; their modeling is introduced in the following. $\tau_{\gamma,\rm EBL}(E_\gamma,z)$ is the optical depth for the interaction of gamma-rays with the EBL (181; 165).

The gamma-rays produced in the hadronic processes can interact with the low energy thermal photons present in the CSM (34; 32; 35). In these interactions, electron-positron pairs

can be produced. Electron-positron pairs can also be produced in Bethe-Heitler processes, where high-energy photons interact with nuclei (mostly protons) in the ejecta (32).

The attenuation of the gamma-ray spectra due to photon-photon pair production is taken into account through the factor $e^{-\tau_{\gamma\gamma}}$ in Eq. 3.8; the optical depth $\tau_{\gamma\gamma}$ of the CSM thermal photons is computed as follows

$$\tau_{\gamma\gamma} = r_{\rm max} \int_0^\infty n_{\rm ph}(\varepsilon)\sigma_{\gamma\gamma}(E_\gamma, \varepsilon){\rm d}\varepsilon \ , \tag{3.9}$$

where ε is the energy of thermal photons and $\sigma_{\gamma\gamma}(E_\gamma, \varepsilon)$ is the photon-photon annihilation cross section (182; 32). The number density of thermal photons follows a black-body spectrum,

$$n_{\rm ph}(\varepsilon) \propto \frac{\varepsilon^2}{\exp(\varepsilon/T)+1} \ , \tag{3.10}$$

where T is the temperature of the thermal photons and can be defined in terms of average energy, $\varepsilon_{\rm av}$ of photons as $T = \varepsilon_{\rm av}/3.15$. The constant of proportionality is such that

$$\int_0^\infty {\rm d}\varepsilon n_{\rm ph}(\varepsilon) = U_{\rm ph,av} \ . \tag{3.11}$$

The average energy density of thermal photons in the CSM is:

$$U_{\rm ph,av} = \frac{1}{r_{\rm max}} \int_{r_{\rm in}}^{r_{\rm max}} {\rm d}r \frac{L_{\rm SN,pk}}{4\pi c r^2} \ , \tag{3.12}$$

where $L_{\rm SN,pk}$ is the SN peak luminosity. In general, the energy density of thermal photons scales as $1/r^2$ with the shock radius, r. We take the average energy density of the thermal photons in the interaction zone, i.e. between $r_{\rm in} \leq r < r_{\rm max}$, to make a reasonable estimate of the absorption of gamma-rays caused by the thermal photons.

In addition to $\gamma\gamma$ pair production losses, Bethe-Heitler pair production losses can also affect the gamma-ray spectra. The loss due to this process can be estimated by the factor $e^{-\tau_{BH}}$ in Eq. 3.8, where τ_{BH} is the optical depth. The latter depends on the mass and composition of the ejecta and we model it as in Ref. (32).

The electrons (positrons) produced in these processes may lose energy via synchrotron

radiation due to the presence of magnetic fields in the shocked CSM. They also lose energy due to inverse Compton scattering with low-energy photons in the CSM. Electrons and positrons can then annihilate and produce low-energy gamma-rays, which in turn modify the observed gamma-ray spectra. This cascading of electromagnetic (EM) interactions modifying the gamma-ray spectrum can be estimated with a broken power law and is given by (183),

$$\phi_{\gamma,\mathrm{cascade}}(E_\gamma) \propto \begin{cases} E_\gamma^{-1.5} & (E_\gamma < E_{\gamma,\mathrm{b}}) \\ E_\gamma^{-\alpha_\gamma} & (E_{\gamma,\mathrm{b}} < E_\gamma < E_{\mathrm{cut}}) \end{cases} \tag{3.13}$$

where E_{cut} is the cut-off energy defined as $\tau_{\gamma\gamma}(E_\gamma = E_{\mathrm{cut}} = E_{\mathrm{max}}) = 1$, $E_{\gamma,\mathrm{b}}$ is the break energy given by $E_{\gamma,\mathrm{b}} = 4E_{\mathrm{cut}}^2/3(2m_\mathrm{e}c^2)^2\varepsilon_{\mathrm{av}}$ and the power law index $\alpha_\gamma = 2$. This cascaded flux is normalized to the total energy lost above E_{cut} due to pair production. This suggests that the larger the absorption, the larger the cascaded flux. Therefore, harder spectra would produce large cascaded gamma-ray flux.

The primary electrons accelerated in the shock could also produce gamma-rays via inverse Compton. The gamma-ray contribution of $p-p$ collisions (i.e., $\pi^0 \longrightarrow 2\gamma$) generally dominates in the high-energy range (GeV), hence the gamma ray contribution from the primary electrons can be ignored, see e.g. (34).

3.2.3 Neutrino production

Neutrinos are produced through the decay of charged pions created in $p-p$ interactions, $\pi \longrightarrow \mu\nu_\mu$ and $\mu \longrightarrow e\nu_e\nu_\mu$. The decay of η mesons also produces neutrinos, but their contribution is smaller than the one of pions (29). The evolution of neutrinos at different radii is governed by the following equation (36):

$$\frac{\mathrm{d}N_{\nu_\mathrm{f}}(E_\nu, r)}{\mathrm{d}r} + \frac{N_{\nu_\mathrm{f}}(E_\nu, r)}{v_{\mathrm{sh}} t_{\mathrm{esc}}(r)} = N_{\nu_\mathrm{f}}^{\mathrm{inj}}(E_\nu, r)\ , \tag{3.14}$$

where $t_{\mathrm{esc}}(r) = r/4c$ is the time required for neutrinos to escape the CSM (see comments below Eq. 3.5). of flavour f ($f = e, \mu$ at the source) with neutrino energy E_ν. The neutrino injection

term $N^{\rm inj}_{\nu_{\rm f}}(E_\nu, r)$ is obtained by following Ref. (29).

For $E_{\rm p} < 0.1$ TeV:

$$N^{\rm inj}_{\nu_e}(E_\nu, r) = 2\frac{\tilde{\eta}}{K_\pi}\frac{4cn_{\rm CSM}(r)m_{\rm e}}{v_{\rm sh}m_{\rm p}}\int_{E_{\rm min}}^{\infty}\frac{{\rm d}E_\pi}{\sqrt{E_\pi^2 - m_\pi^2}}\sigma_{\rm pp}\left(E_{\rm p}\right)N_{\rm p}\left(E_{\rm p}, r\right)f_{\nu_e}\left(\frac{E_\nu}{E_\pi}\right)$$
$$N^{\rm inj}_{\nu_\mu}(E_\nu, r) = 2\frac{\tilde{\eta}}{K_\pi}\frac{4cn_{\rm CSM}(r)m_{\rm e}}{v_{\rm sh}m_{\rm p}}\int_{E_{\rm min}}^{\infty}\frac{{\rm d}E_\pi}{\sqrt{E_\pi^2 - m_\pi^2}}\sigma_{\rm pp}\left(E_{\rm p}\right)N_{\rm p}\left(E_{\rm p}, r\right)$$
$$\times\left[f^{(1)}_{\nu_\mu}\left(\frac{E_\nu}{E_\pi}\right) + f^{(2)}_{\nu_\mu}\left(\frac{E_\nu}{E_\pi}\right)\right] \qquad (3.15)$$

where $E_{\rm p} = m_{\rm p} + E_\pi/K_\pi$, and E_π is the energy of pion and $m_{\rm e}$ is mass of electron. The minimum energy of pion is given by $E_{\rm min} \simeq E_\nu + m_\pi^2/4E_\nu$. The parameters K_π and $\tilde{\eta}$ are free parameters and used for connecting the injection rates above energy $E_{\rm p} = 1$ TeV.

For $E_{\rm p} \geq 0.1$ TeV:

$$N^{\rm inj}_{\nu_e}(E_\nu, r) = \frac{4cn_{\rm CSM}(r)m_{\rm e}}{v_{\rm sh}m_{\rm p}}\int_{m_{\rm p}}^{\infty}{\rm d}E_{\rm p}\frac{\sigma_{\rm pp}(E_{\rm p})}{E_{\rm p}}N_{\rm p}(E_{\rm p}, r)F_{\nu_e}\left(\frac{E_\nu}{E_{\rm p}}\right)$$
$$N^{\rm inj}_{\nu_\mu}(E_\nu, r) = \frac{4cn_{\rm CSM}(r)m_{\rm e}}{v_{\rm sh}m_{\rm p}}\int_{m_{\rm p}}^{\infty}{\rm d}E_{\rm p}\frac{\sigma_{\rm pp}(E_{\rm p})}{E_{\rm p}}N_{\rm p}(E_{\rm p}, r)$$
$$\times\left[F^{(1)}_{\nu_\mu}\left(\frac{E_\nu}{E_{\rm p}}\right) + F^{(2)}_{\nu_\mu}\left(\frac{E_\nu}{E_{\rm p}}\right)\right]. \qquad (3.16)$$

Here, F_{ν_e}, $F^{(1)}_{\nu_\mu}$, $F^{(2)}_{\nu_\mu}$ and f_{ν_e}, $f^{(1)}_{\nu_\mu}$, $f^{(2)}_{\nu_\mu}$ are the neutrino distributions from pion decay valid for $E_p \geq 0.1$ TeV and $E_p < 0.1$ TeV, respectively (29). The energy dependent cross-section $\sigma_{\rm pp}(E_{\rm p})$ is taken from Ref. (29). The neutrino flux of flavour f at source is given by,

$$E_\nu^2\phi^{\rm s}_{\nu_{\rm f}}(E_\nu) = \int_{r_{\rm in}}^{r_{\rm max}}\frac{{\rm d}r}{v_{\rm sh}}\frac{E_\nu^2 N_{\nu_{\rm f}}(E_\nu, r)}{m_{\rm e}c^2 t_{\rm esc}}. \qquad (3.17)$$

The all flavour flux at source is $E_\nu^2\phi^{\rm s}_\nu = \sum_{\rm f}E_\nu^2\phi^{\rm s}_{\nu_{\rm f}}(E_\nu)$. During propagation to Earth, the flavour combination may change due to flavour mixing (184), leading to the following flavour composition at Earth: $\nu_{\rm e} : \nu_\mu : \nu_\tau = 1 : 1 : 1$.

$$E^2_{\nu,{\rm obs}}\Phi_\nu(E_{\nu,{\rm obs}}) = \frac{\sum_{\rm f}E_\nu^2\phi^{\rm s}_{\nu_{\rm f}}(E_\nu)}{4\pi d_{\rm L}^2}, \qquad (3.18)$$

where $E_\nu = (1+z)E_{\nu,\rm obs}$ and z is the cosmological redshift.

Note that the neutrino (gamma-ray) production from $p-p$ interactions ceases to be significant as the shock radius reaches the maximum radius, $r_{\rm max}$. This is determined by $\min[r_{\rm dec}, r_{\rm out}]$. The deceleration radius, $r_{\rm dec}$, of the SN shock corresponds to the radius when the ejecta mass, $M_{\rm ej}$, sweeps up the same amount of CSM mass and is defined as $r_{\rm dec} = M_{\rm ej} v_{\rm w}/\dot{M}_{\rm W} = r_{\rm in} + M_{\rm ej}/(4\pi m n_{\rm in,CSM} r_{\rm in}^2)$. The region $r < r_{\rm dec}$ is known as the free expansion phase of the CSM. Particle acceleration and production are dominant in this phase. Once the shock reaches the maximum radius i.e., $r_{\rm max}$, the interaction of the shock with the ISM begins, which is beyond the scope of this work[4].

Most SNe show signs of interaction within a few years of their evolution with rarer cases showing interaction on timescales of $\mathcal{O}(10)$ years, see e.g. Refs. (185; 186; 187; 188; 189; 190). Since the maximum time, $t_{\rm max}$ (corresponding to $r_{\rm max}$) depends on the extent of the CSM, YSNe with extended CSM could have $t_{\rm max} \sim \mathcal{O}(10)$ years. However, this extended CSM is less dense than the CSM of $t_{\rm max} \simeq 1$ year. Therefore, the neutrino and gamma-ray fluxes for this extended CSM are similar to that of YSNe with CSM of 1 year (results not shown here). Therefore, we take $r_{\rm max} = r_{\rm out}$ (corresponds to $t_{\rm max} = 1$ year) throughout this work.

Different classes of YSNe produce different fluxes of secondaries (gamma-rays and neutrinos) due to wide differences in these input parameters. In the following, we discuss the different Types of YSNe and their impact on the secondary production.

3.3 Young supernova types

Supernovae are classified as Type-I and Type-II based on the presence of H lines in the observed spectra. Type-I SNe do not show H lines, whereas Type-II do. Supernovae are further classified into different sub-Types of Type-I (Ia, Ib and Ic) and Type-II (IIn, II-P, IIb, II-L) SNe depending on different observed characteristics. Type Ia SNe show Silicon II (Si II) absorption lines in their spectra. Presence of He lines in Type Ib SNe differentiates them from Type Ic. Type IIn

[4] In the case of old SNR (1 kyr), the flux due to the Sedov-Taylor phase ($r > r_{\rm dec}$) decreases by several (more than 3–4) orders of magnitude due to the very low target (CSM or ISM) density. Thus, the total flux from the Sedov-Taylor phase will be negligible compared to the early YSN phase.

and IIb exhibit narrow and broad H lines respectively. The spectra of Type II-P SNe show a plateau whereas Type II-L SNe show linearly declining spectra (for details on SN classification, see e.g. Refs. (191; 192)). Except for SNe Ia, all other SN classes are powered by the collapse of the stellar core.

The diverse classes of YSNe differ in parameters like mass loss rate, wind velocity, size of the CSM, and efficiency of shock energy transfer to protons. Below we report about these characteristic parameters as from electromagnetic observations for different Types of YSNe.

- Type IIn SNe are found to have very dense CSM as a result of heavy mass loss (10^{-4}–10^{1} $\dot{M}_{\odot}yr^{-1}$) before explosion (37; 193). The wind velocity, v_w, for such SNe can typically vary between 30–600 kms^{-1} (37). Their progenitors are not well known and have been found to be connected to LBV, Red Supergiant (RGB) and Yellow Hypergiant (YHG) stars (see e.g., (44; 194; 195; 196) and references therein). These stars have large mass loss rates ($\dot{M}_W \sim 10^{-3}$-10^{1} $M_{\odot}yr^{-1}$) and moderate wind velocity ($v_w \sim 100$ kms^{-1}) (37; 193). Therefore, Type IIn SNe show a dense CSM ($n_{in,CSM} \sim 10^{11}$ cm^{-3} (37)). Their shock velocity, v_{sh}, ranges between 10^3 and 10^4 km s^{-1} (36; 38; 40) (see Eq. 3.1). The fraction of kinetic energy, ε_p, that goes into high energy protons is estimated to be 10^{-2}–1.5×10^{-1} (173). Therefore, we choose the range of ε_p as 10^{-2}–10^{-1}. The fraction of post-shock magnetic energy, ε_B, can be constrained from radio observations of SNe and is in the range $\varepsilon_B \sim 10^{-4}$–$10^{-2}$ (38; 39; 158; 197).

- Type II-P SNe show a plateau in their light curves up to a few months ($\sim$ 20–100 days) after the explosion (198; 199). This is due to the abundance of hydrogen in the SN ejecta. This SN class usually arises from red supergiant (RSG) stars (37; 200; 201; 202; 203) and they are found to have large CSM density. Eruptive mass losses of such stars just before [$\mathcal{O}(1)$ year] the SN explosion are believed to be the reason of their large CSM densities (198; 204). The typical mass loss rate during this phase has been reported to be $\mathcal{O}(10^{-3})$ $\dot{M}_{\odot}yr^{-1}$ (204; 205; 206) with wind velocity of $\mathcal{O}(10)$ km s^{-1} (207). Larger mass loss rates [$\mathcal{O}(1)\dot{M}_{\odot}yr^{-1}$] with wind velocity 100 km s^{-1} have also been predicted, see (199; 198); however, this might be an exception (see e.g., (208; 143; 209)) [5]. Inter-

[5] Ref. (199) investigated early light curves of some Type II SNe. Their results suggest the need for local CSM ($r < 2 \times 10^{14}$ cm) in order to reproduce the rapid rise time and brighter emission at peak observed in some SNe. This is an exception and we therefore focus on the average mass loss over a longer period of time.

estingly, our calculation only depends on the ratio $\dot{M}_{\rm W}/v_{\rm W}$ (see Eq. 3.1); hence, given the evidence of large mass loss rates, we adopt 10^{-2} $\dot{\rm M}_{\odot}{\rm yr}^{-1}$ as our typical mass loss rate with wind velocity $\mathcal{O}(100)$ km s^{-1} (204; 199). This choice is equivalent to assume a mass loss rate 10^{-3} $\dot{\rm M}_{\odot}{\rm yr}^{-1}$ with wind velocity 10 km s^{-1}.

The eruptive mass loss is responsible for a dense CSM which is found to exist up to $\sim 10^{15}$ cm (205). The CSM density beyond this radius is smaller and is due to the stellar wind of RSG stars (37). A typical RSG wind has a mass loss rate in the range 10^{-6}–10^{-5} $\dot{\rm M}_{\odot}$ yr^{-1} with wind velocities of about 10–20 km/s (37). We distinguish these two different phases of the CSM by naming them "eruptive" (for the large mass loss rates) and "normal" (the smaller RSG winds). The shock velocity for this YSN class is $\mathcal{O}(10^4)$ km/s (206).

- Type II-L SNe have linear light curves, while Type II-b show broad He lines in their spectra. Their progenitors have similar mass loss rates, which lie in the range 10^{-5}–10^{-4} $\dot{\rm M}_{\odot}{\rm yr}^{-1}$ and have wind velocity between 2×10^{1}–10^{2} km s^{-1} (210; 37; 211; 212; 41; 213; 143). The shock velocity for these Types of SNe is found to be of the order of 10^4 km/s (214).

- Type Ib/c SNe are rich in helium (He) and usually have lower mass loss rates (10^{-7}–10^{-4} $\dot{\rm M}_{\odot}$ yr^{-1}) than IIn and II-P SNe (37; 215; 216; 145). The wind velocity for Ib/c SNe is very large ($v_{\rm w}\sim10^3$ km s^{-1}). Moreover, the inner radius of the CSM is small ($r_{\rm in}\simeq10^{12}$ cm, corresponds to the size of the progenitor). This implies that the volume of the CSM shell in the vicinity of $r_{\rm in}$ is also small and therefore the total number of proton targets is quite low. Thus, the neutrino and gamma-ray emission from such YSNe is negligible (as most of the secondaries are produced near $r_{\rm in}$). However, late time observations of SN 2014C (which was initially classified as Ib/c SN) highlight the presence of interaction of the SN ejecta with the hydrogen rich CSM at 6×10^{16} cm (207). The CSM is found to extend up to 2.5×10^{17} cm (42); hence, we assume $r_{\rm out}=10^{17}$ cm. This corresponds to the beginning of shock interaction at about 1.5 years after the explosion and substantial reduction of the dense CSM interaction at about 3 years. Thus the duration of emission is considered to be about 1.5 years. This dense CSM is possibly created by large mass loss rate of $\mathcal{O}(1)$ $\rm M_{\odot}yr^{-1}$ with wind velocity in the range (10^1-10^3 km s^{-1}) (207). However, smaller mass loss rate of $\mathcal{O}(10^{-3})$ $\rm M_{\odot}yr^{-1}$ with velocity 100 km s^{-1} has also

Table 3.1: Characteristic parameters for different YSN Types. We consider two different phases of the CSM of II-P SNe namely, eruptive (created by the large mass loss occurring a few years prior to explosion) and normal (due to the usual RSG wind during stellar evolution).

Parameters	**IIn** (1 yr)	**II-P**		**IIb/II-L** (1 yr)	**Ib/c** (1 yr)	**Ib/c (LT)** (1.5 yrs)
		Eruptive ($\leq$ 12)	**Normal** ($>$ 12 days)			
$n_{\rm in,CSM}$ (cm^{-3})	10^{11}	10^{12}	10^{9}	6×10^{11}	2.4×10^{12}	2×10^{6}
$\dot{\rm M}_W$(M$_\odot$ yr^{-1})	10^{-1}	10^{-2}	2×10^{-6}	3×10^{-5}	10^{-5}	2×10^{-2}
$v_{\rm w}$ (kms^{-1})	10^{2}	10^{2}	1.5×10^{1}	3×10^{1}	10^{3}	10^{2}
$r_{\rm out}$ (cm)	2×10^{16}	10^{15}	3×10^{16}	3×10^{16}	6×10^{16}	10^{17}
$v_{\rm sh}$ (kms^{-1})	7×10^{3}	10^{4}	10^{4}	10^{4}	2×10^{4}	10^{4}
$r_{\rm in}$ (cm)	4×10^{14}	6×10^{13}	6×10^{13}	6×10^{12}	3×10^{11}	5×10^{16}
$\varepsilon_{\rm p}$	10^{-2}	10^{-1}	10^{-1}	10^{-1}	10^{-1}	5×10^{-2}
$\varepsilon_{\rm B}$	10^{-2}	10^{-2}	10^{-2}	10^{-2}	10^{-2}	10^{-2}
SN Rate	9%	48%	$--$	17%	26%	2.6%

been proposed (217). Hence, we assume a mass loss rate of $\mathcal{O}(10^{-2})$ M$_\odot$yr^{-1} and wind velocity 100 km s^{-1} to be conservative. The exact mechanism of this large mass loss is not well understood. Therefore, we assume a wind profile in order to obtain a conservative estimate of the CSM density. The deceleration radius, $r_{\rm dec}$ $(9\times10^{16}$ cm) of the shock moving forward in the CSM is comparable to r_{out}. SN 2004dk and SN2019yvr are similar examples of Ib/c SN with late time interaction after explosion (43; 218). Reference (207) investigated a sample of 183 Ib/c SNe and found that 10% of the sample has late time interaction like SN2014C, which is about 2.6% of the total core-collapse SNe. Hence, we include late time interaction of Ib/c SNe in our analysis. We choose the SN 2014C as a representative of the class Type Ib/c late time (LT) SN (217; 219; 207; 34).

In Table 3.1, we list the typical values adopted for each of our modelling parameters for all SN Types introduced above. While we chose to be conservative in our choice of the characteristic parameters, we also consider a range of variability for the most uncertain model parameters and the latter defines a band in the final results (see Sec. 5.2 and 5.1).

3.4 Dependence of the gamma-ray and neutrino emission on the young supernova type

The YSN emission properties largely vary across different SN Types. In this Section, we first characterize the gamma-ray and neutrino emission for our benchmark YSN IIn and then compare the particle production across different YSN classes. Throughout this Section, the emission of secondaries is computed for 1 year for all YSN Types, except for Ib/c (LT) YSNe for which we consider an emission period of 1.5 years.

3.4.1 Characteristic gamma-ray and neutrino emission

As a primary example to illustrate the YSN neutrino and gamma-ray emission we consider Type IIn SNe (see Sec. 3.2 and Table 3.1) as they have the highest mass loss rate in the SN sample presented in Table 3.1. Unless otherwise specified, we assume that our benchmark YSN is located at 10 Mpc from Earth. Most SNe are detected between 1 and 100 Mpc, with the majority being discovered at $\mathcal{O}(90)$ Mpc, see e.g. Fig. 2 of Ref. (220). Hence, our choice of the typical SN distance is somewhat optimistic, yet compatible with observations.

The top and bottom left (right) panels of Fig. 3.1 show the gamma-ray (neutrino) luminosity and fluence. The top left panel shows the gamma-ray light curve at E_γ =1, 10^2, 10^4 GeV, while the gamma-ray fluence produced by $p-p$ collisions in IIn YSNe during its first year is displayed in the bottom left panel. The fluence in the bottom left panel of Fig. 3.1 does not include any attenuation at the source. Gamma-rays above 100 GeV can interact with low energy photons and ambient matter in the source and may get lost. This corresponds to $\tau_{\gamma\gamma}$ and $\tau_{\rm BH}$, respectively, in Eq. 3.8 and are discussed below (see discussion of Fig. 3.2).

The top panel on the right shows the neutrino light curve (blue) for three different energies ($E_\nu = 10^3$, 10^4, 10^5 GeV) for the first year of the YSN. The light curves start around 7 days after the explosion. This delay corresponds to the inner radius, $r_{\rm in}$ (i.e., when the interaction between the shock wave accelerated protons and the CSM protons has begun). The inner radius, $r_{\rm in}$, also depends on the class properties of each SN Type. The plot in the bottom right panel

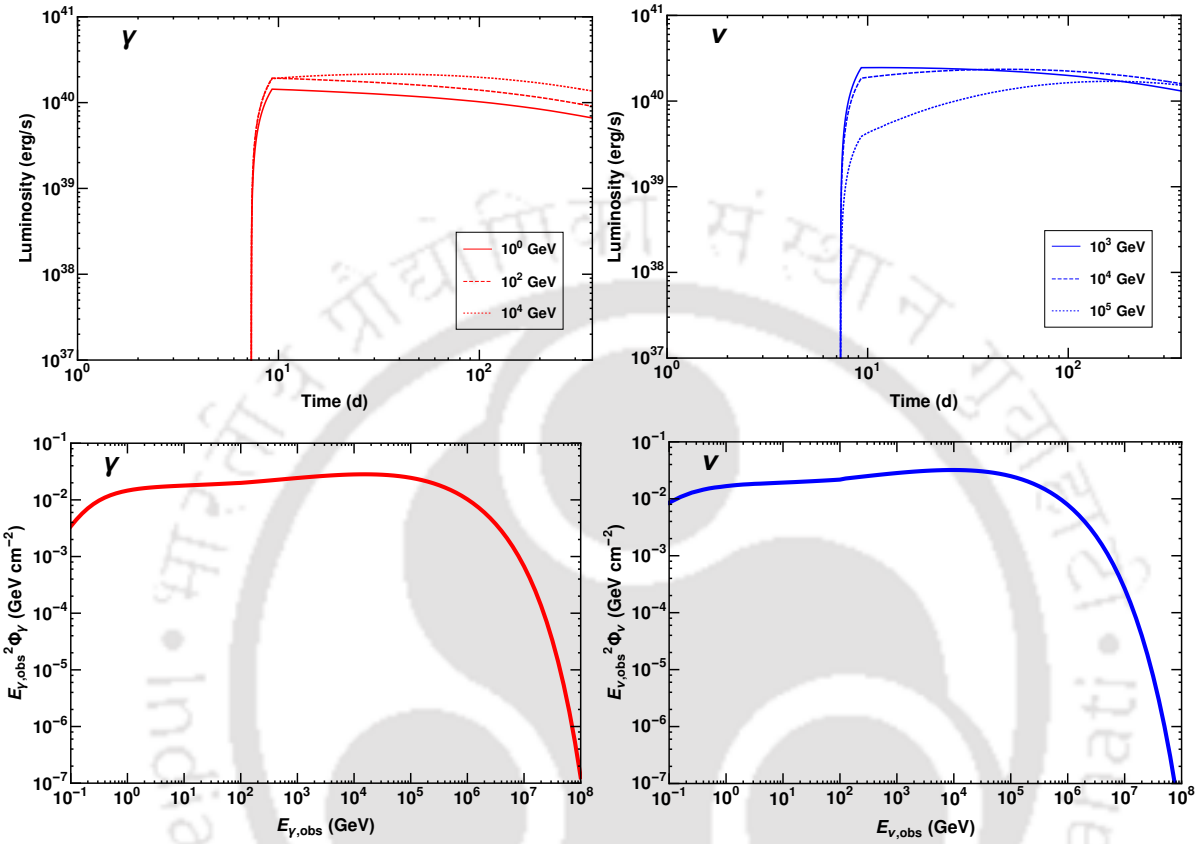

Figure 3.1: *Top panels:* Luminosity of gamma-rays (left) and all-flavour neutrinos (right) of our benchmark YSN IIn (see Table 3.1) as a function of time. The temporal evolution at the source are shown for three representative energies ($E_\gamma = 10^0, 10^2$, and 10^4 GeV for gamma-rays and $E_\nu = 10^3, 10^4$, and 10^5 GeV for neutrinos). *Bottom panels:* Corresponding gamma-ray (left) and all-flavour neutrino (right) fluences at Earth as functions of the observed particle energy. The distance of our YSN IIn from Earth is chosen to be 10 Mpc. Both fluences for neutrinos and gamma-rays are time integrated over the first year of the SN evolution. Gamma-rays are shown without any attenuation due to energy losses (see discussion of Fig. 3.2 for details). Therefore, the spectra of both species from $p-p$ collision follow a similar behaviour of growing with particle's energy and falling rapidly above 10^5 GeV.

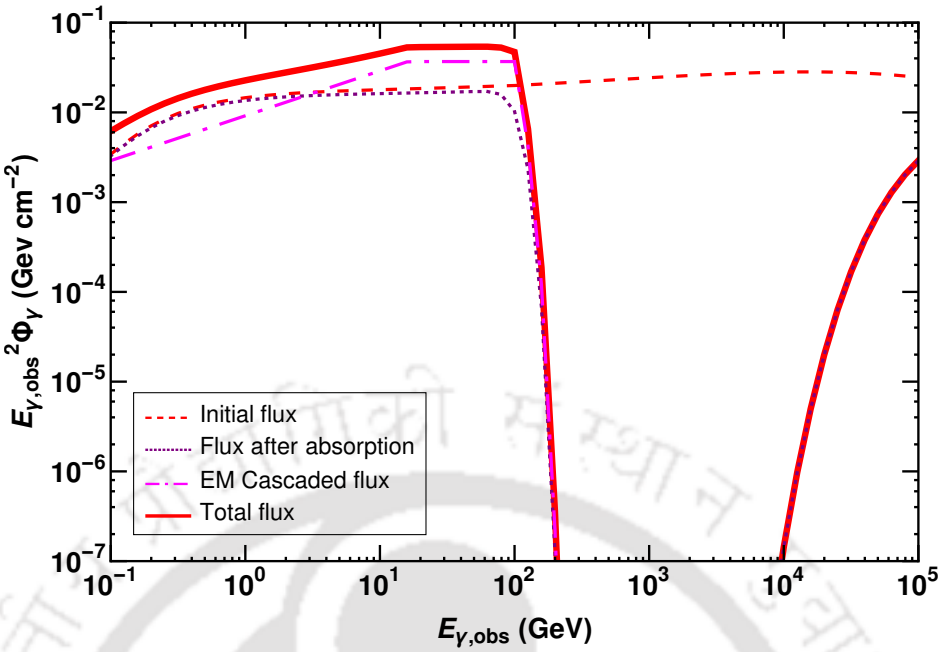

Figure 3.2: Gamma-ray fluence at Earth after including the relevant absorption processes and EM cascades at the source as a function of the gamma-ray energy for our benchmark YSN IIn (see Table 3.1) at a distance of 10 Mpc. The red-dashed curve represents the fluence obtained via $p-p$ collisions. The purple-dotted curve is the fluence after absorption due to $\gamma\gamma$ pair production loss and Bethe-Heitler loss in the CSM. The gamma-ray fluence due to EM cascades is shown by the dot-dashed magenta curve. The thick red solid curve represents total flux at the source after absorption and EM cascades. The gamma-ray fluence between 10^2 to 10^4 GeV is heavily attenuated due to the absorption processes occurring in the source. The final gamma-ray flux (thick red curve) is a combination of the flux surviving to absorption and the EM cascaded flux.

shows the energy spectra of the YSN emitted neutrinos for the first year. The neutrino flux (top right plot) falls rapidly above energy $E_\nu \sim 10^5$ GeV. This is due to the maximum energy of protons $E_{\mathrm{p,max}}$, which determines the exponential cut-off of the proton spectra. This clearly suggests that the SN properties driving $E_{\mathrm{p,max}}$ will influence the cut-off, and the latter would be different for different YSN Types. Note that these interpretations also hold for the gamma-rays in the left panel.

The fluence in the bottom left panel of Fig. 3.1 will be affected by absorption processes. Fig. 3.2 shows the effect of absorption and EM cascades on the gamma-rays produced via $p-p$ interactions for Type IIn YSNe for a thermal energy distribution of photons with average energy

$\varepsilon_{\rm av} = 1$ eV and SN peak luminosity $L_{\rm SN,pk} = 10^{41}$ erg/s respectively (2; 35). We show gamma-rays without any absorption (red-dashed curve), gamma-rays with absorption due to photon-photon pair production and BH pair production (purple-dotted curve), and the EM cascade (magenta dot-dashed curve). It is interesting to note that the initial flux above 200 GeV mostly disappears except a little tail at higher energies due to photon-photon pair production losses. This is due to the fact that the photon-photon cross section $\sigma_{\gamma\gamma}$ falls rapidly at higher energies and the thermal photons, $n_{\rm ph}(\varepsilon)$, have a black-body spectrum; the product of both gives rise to a optical depth, $\tau_{\gamma\gamma}$ creating a well-shaped attenuation factor $e^{-\tau_{\gamma\gamma}}$. The cascaded gamma-ray flux also falls sharply at 200 GeV because the photon-photon pair loss factor $e^{-\tau_{\gamma\gamma}}$ hardly allows for anything to survive above 200 GeV.

Bethe-Heitler losses generally have a tiny effect on the gamma-ray energy distribution. For Type IIn SNe, the amount of attenuation is the small gap between the red-dashed and the purple dotted curve below 200 GeV. Thus the final gamma-ray flux (thick red curve) is a combination of the flux surviving to absorption (purple dotted) and EM cascaded flux (magenta dot-dashed). The EM cascades are responsible for a boost in the gamma-ray spectra below 200 GeV. Propagation to Earth is not important at 10 Mpc but important for large distances ($\sim$ 1 Gpc) as losses due to EBL will take place, for example for the diffuse flux (see Sec. 5.2).

3.4.2 Dependence on the young supernova type

Because of the intrinsic differences among the properties of the YSN Types introduced in Sec. 3.3, we should expect a wide variation in the emission of secondary particles. Below we discuss a few examples of these variations for the secondary gamma-rays and neutrinos for a source at 10 Mpc and $\alpha_{\rm p} = 2.0$.

We show the gamma-ray fluences produced by YSNe in the top left panel of Fig. 3.3 for the benchmark parameters shown in Table 3.1. The fluxes are integrated over a year. Type IIn YSNe produce the largest gamma-ray fluence. The other Types of YSNe create smaller fluences and the fluence of Type Ib/c YSNe is extremely small relative to the one seen from the Type IIn YSNe. The sharp fall and rise of these fluences at higher energies (above 10 GeV) is due to the fact that gamma-rays suffer losses due to $\gamma\gamma$ pair production, as discussed in Sec. 3.2.2.

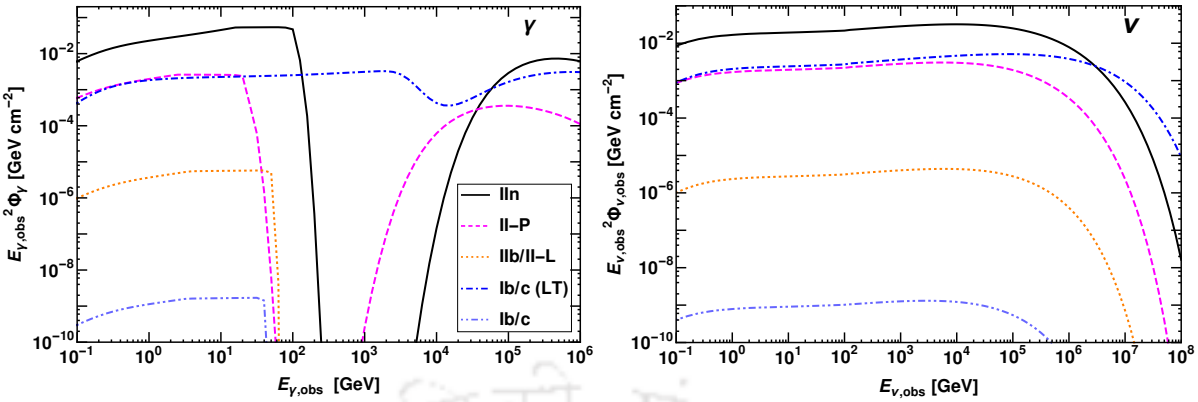

Figure 3.3: Gamma-ray (left) and all-flavour neutrino (right) fluences integrated for a year at Earth from different classes of YSN, as listed in Table 3.1, for a source located at 10 Mpc. For both gamma-rays and neutrinos, Type IIn YSNe have the largest fluence, followed by II-P and Ib/c (LT) YSNe.

The fall and rise of the fluences occur at different energies according to the YSN class. The amount of losses are also different for different YSNe. This is due to the variation of the parameters, i.e. average energy ($\varepsilon_{\mathrm{av}}$) and peak luminosity ($L_{\mathrm{SN,pk}}$) of thermal photons expected from different Types of YSNe. The parameter $\varepsilon_{\mathrm{av}}$ is assumed to be: 1 eV for IIn YSNe, 4.5 eV for II-P YSNe, 1 eV for IIb/II-L and Ib/c YSNe, and 0.05 eV for Ib/c (LT) YSNe. The peak luminosities are assumed to be 10^{41} erg/s for IIn SNe, $\sim 5 \times 10^{40}$ erg/s for II-P and Ib/c (LT) SNe, and 10^{42} erg/s for IIb/II-L and Ib/c SNe (35; 205; 221; 214; 34; 222; 223). The fluence of Type Ib/c (LT) YSN falls at higher energy than that of other SN Types due to its small average energy of thermal photons. The average energy is small because of the lower temperature of thermal photons as the CSM is located very far away (see Table 3.1) from the stellar envelope. The large distance to the CSM also affects the density of the thermal photons that results in less absorption of gamma-rays for Type Ib/c (LT) YSNe. Type IIn and II-P YSNe have similar losses as the peak luminosities of thermal photons are quite similar. Heavy losses of gamma-rays are seen for Type IIb/II-L and Ib/c YSNe because their thermal photon luminosity is quite large which implies large thermal photon density.

The right panel of Fig. 3.3 shows the corresponding neutrino fluence integrated over a year for the different YSN Types. Due to the dense CSM, Type IIn YSNe show the largest fluence falling rapidly around $E_\nu \sim 10^6$ GeV. The fluence of Type Ib/c (LT) YSNe starts to dominate above $E_\nu \sim 3 \times 10^6$ GeV. The reason is that the maximum proton energy ($E_{\mathrm{p,max}}$) strongly

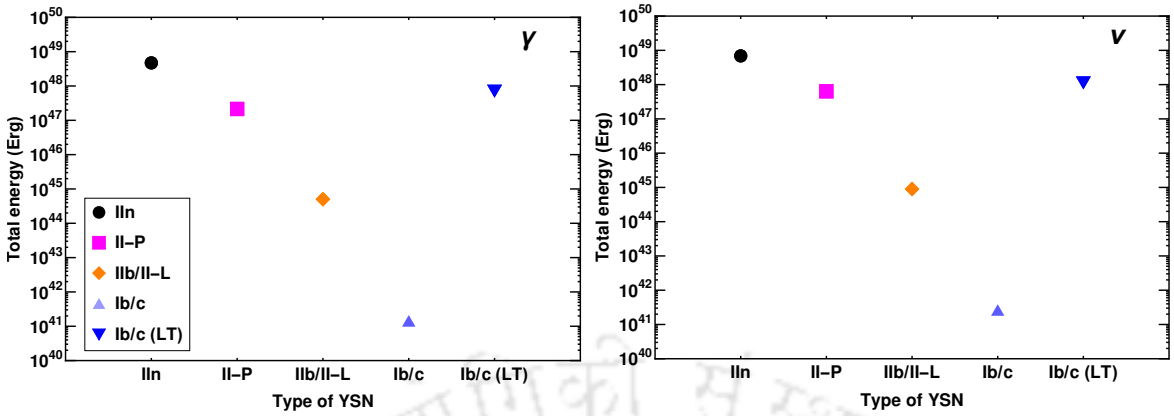

Figure 3.4: Total energy emitted by each source in gamma-rays (left) and neutrinos (right). The duration of emission of secondary particles is taken to be a year and integrated in the range 10^{-1}–10^{8} GeV. The total energy emitted in gamma-rays is generally smaller than that of neutrinos; this is due to the attenuation of gamma-rays in the source. The largest energy is emitted by Type IIn YSNe, followed by Type Ib/c (LT) and II-P YSNe.

depends on the shock velocity and shock radius. The shock velocity and shock radius for Ib/c (LT) YSNe are larger than those of Type IIn YSNe, resulting in greater $E_{\rm p,max}$. The fluence of Type II-P[6] and Ib/c (LT) YSNe are comparable at lower energies due to their dense CSM. The fluences of Type IIb/II-L and Type Ib/c YSNe are quite small in spite of the large initial CSM density, $n_{\rm in,CSM}$. This is due to the small size of their inner radius ($r_{\rm in}$) of the CSM; moreover, most of the secondaries are only produced in the vicinity of $r_{\rm in}$.

The estimated neutrino fluences for the various YSNe classes are comparable to the ones reported in Ref. (33) except for the ones of Type II-P YSNe. In this case, our YSNe-IIP fluence is larger [7] since it relies on model parameters extrapolated from more recent observations of II-P SNe, as discussed in Sec. 3.3; specifically, the mass loss rate that we adopt is one order of magnitude larger than the one assumed in Ref. (33). On the other hand, a CSM density smaller than our benchmark case in Table 3.1 would result in a smaller fluence (33).

Fig. 3.4 shows the total energy emitted in gamma-rays (left) and neutrinos (right) for each

[6]The fluences of Type II-P (gamma-rays and neutrinos) are dominated by the emission from the eruptive phase (see Table 3.1), the contribution from the normal phase is negligible.

[7]Note that the large mass loss rates of II-P SNe discussed in Ref. (199) may be responsible for a fluence comparable to the one of IIn YSNe (224; 155). However, such mass loss rates might be an exception, as we discussed in Sec. 3.3 and therefore we do not consider them.

YSN Type, in order to favour a comparison among their overall energetics. We have integrated the gamma-ray and neutrino fluxes in the energy range 10^{-1}–10^{8} GeV for a year. Both for gamma-rays and neutrinos, the largest energy is emitted by Type IIn YSNe, followed by Type Ib/c (LT) and II-P YSNe. By looking at the fluxes of neutrinos and gamma-rays in Fig. 3.3, one might have the impression that the total energy emitted in gamma-rays is smaller than that of neutrinos due to the large absorption of gamma-rays (the dips). However this is not the case, most of the attenuated high energy gamma-ray flux has reappeared at lower energies due to the EM cascades (see Fig. 3.2 and discussion) determining an overall small amount of loss. If there is no absorption of gamma-rays, the total energy of neutrinos is larger by a factor of about $3/2$ than that of gamma-rays. This corresponds to the product of charged to neutral pion production ratio (2) and the fraction of energy carried by the neutrinos in a charged pion decay ($3/4$).

3.5 Detection prospects of nearby young supernovae in gamma-rays and neutrinos

Now that we have access to the estimated flux data of gamma-rays and neutrinos originating from various YSNe, we can proceed with an evaluation of their detection potential. The detection of neutrinos and gamma-rays from nearby YSNe will help to constrain the model parameters and can potentially provide complementary understanding of shock-CSM interactions. In the following, we investigate the detection prospects of YSNe with present and future gamma-ray telescopes and neutrino detectors.

Figure 3.5 illustrates the detection prospects for our benchmark YSNe in gamma-rays and neutrinos. The top panels display the energy flux expected at Earth for a YSN at 10 Mpc. The top left panel shows that the gamma-ray energy flux would be detectable for Type IIn YSN by Fermi-LAT (163) and CTA (164), while other SN Types can be probed at distances smaller than 10 Mpc. Interestingly, due to gamma-ray attenuation, dips could appear in the gamma-ray spectra between 100–1000 GeV (see related discussion for Fig. 3.2), CTA may be able to probe this feature for local YSNe. However, the detection of such dips requires more detailed analysis (225; 226). The top right panel shows that corresponding neutrino flux from all YSNe are detectable in IceCube (30) below 10 Mpc, in agreement with Ref. (33). Km3NeT (73) and

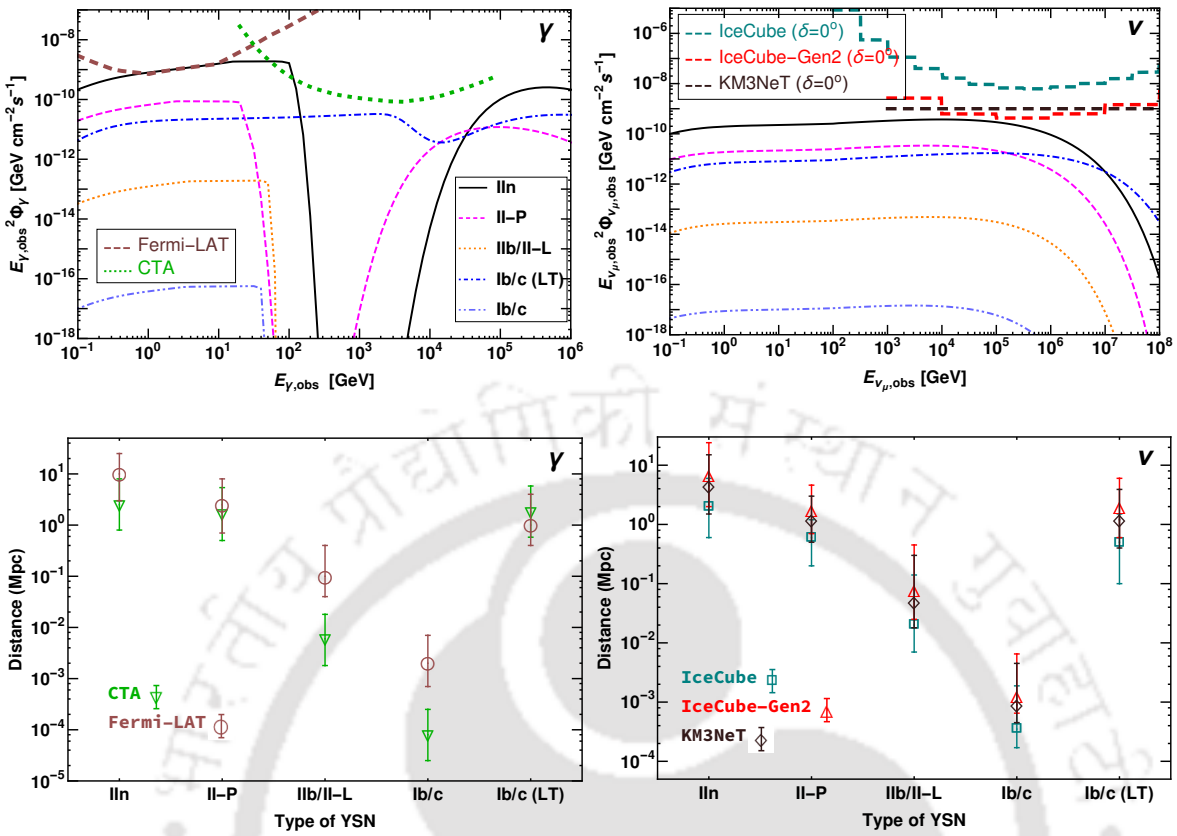

Figure 3.5: Detection prospects of nearby supernovae using gamma-ray (left) and neutrino telescopes (right). *Top left panel:* Gamma-ray energy fluxes from the different YSN Types at 10 Mpc as functions of the observed particle energy. The one year Fermi-LAT sensitivity is shown by the thick light brown dashed curve (163) and the thick green dotted curve represents the 100 hour CTA sensitivity (164). Type IIn YSNe may be detected by both Fermi-LAT and CTA, while all other sources will be too dim at 10 Mpc. *Top right panel:* Corresponding muon neutrino energy fluxes. The sensitivities of IceCube, IceCube-Gen2 and KM3NeT for point source detection are plotted (thick dashed lines) in dark cyan (IceCube) (30), red (IceCube-Gen2) (25) and dark brown (KM3NeT) (73). The sensitivities of IceCube, IceCube-Gen2 and KM3NeT are plotted for the declination angle $\delta = 0^o$. All these neutrino observatories will be able to detect YSNe at distances smaller than 10 Mpc. *Bottom left panel:* Gamma-ray YSN detection horizon for Fermi-LAT (light brown) and CTA (green) as functions of the YSN Type. For each YSN Type, the error band takes into account the model uncertainties (see Sec. 5.2.5). Fermi-LAT and CTA could detect YSNe up to 10 Mpc (see YSNe IIn); CTA could have better sensitivity than Fermi-LAT and reach up to 2 Mpc for YSNe Ib/c (LT). *Bottom right panel:* Corresponding neutrino YSN detection horizon for IceCube (dark cyan), IceCube-Gen2 (red) and KM3NeT (dark brown). IceCube-Gen2 will be able to detect YSNe up to ~ 4 Mpc (see YSNe Type IIn).

IceCube-Gen2 (25) will also be able to detect neutrinos from these sources below 10 Mpc.

The bottom panels of Fig. 3.5 show the detection horizon of existing and upcoming gamma-ray and neutrino telescopes for the different YSN Types, by considering the model parameter uncertainties, see Table 5.1. The reach of different telescopes is calculated by taking into account the integrated flux of each YSN in the specific energy range of detectors' best integral sensitivity. For gamma-rays, the energy range $[10^{-1}, 10^{1}]$ GeV is chosen for Fermi-LAT as it has the best integral sensitivity in this range. However, the whole energy range of CTA, i.e., $[2 \times 10^{1}, 7 \times 10^{4}]$ GeV is taken into account as the fluxes of most of YSNe are attenuated where CTA is most sensitive. The maximum reach of Fermi-LAT and CTA for different YSNe is shown in the bottom left panel of Fig. 3.5. Fermi-LAT and CTA could detect YSNe up to 10 Mpc (see YSNe IIn, for the benchmark parameters). However, Fermi-LAT has comparatively better sensitivity to YSNe than CTA except for Ib/c (LT) YSNe. This is due to the fact that CTA is more sensitive at higher energies and gamma-rays at these energies are attenuated by the thermal photons in the source. The exception of Ib/c (LT) YSNe is accounted for the small gamma-ray attenuation in the source (see top left plot and the discussion of Fig. 3.3). The detection horizon of CTA is affected by the amount of gamma-ray attenuation by the source thermal photons as discussed above. Thus, the detection of these sources in gamma-rays has the potential to unleash information about particle production, emission and propagation in YSNe.

Similarly, for the neutrino telescopes, we consider the YSNe fluxes in the energy range $[10^{5}, 10^{6}]$ GeV as these detectors have best sensitivity to the astrophysical neutrino flux in these energies (see the top right panel). The detection horizons marked in the plot refer to the ones for which the integrated flux is equal to the detectors' integral sensitivity (see the top panels). For example, for YSNe Type IIn at distances above 2 Mpc, the integrated neutrino flux in the energy range 10^{5}–10^{6} GeV would fall below the IceCube sensitivity at $\delta = 0^{o}$ declination. The error bars represent the uncertainties in the model parameters. Our findings concerning the detectability of neutrinos from YSNe IIn are in agreement with the ones of Ref. (36; 227). Considering the uncertainties in the model parameters, IceCube-Gen2 will instead be able to detect Type IIn YSNe up to ~ 20 Mpc (4 Mpc for the benchmark parameters).

3.6 Conclusion

In this chapter, we have investigated the high energy neutrino and gamma ray signals from different classes of young SNe (Type IIn, II-P, IIb/II-L and Ib/c YSNe), up to one year after their explosion. During this time, shock accelerated protons interact with the dense CSM around these objects, leading to the production of secondary high-energy neutrinos and gamma-rays. In addition, we have investigated the late time emission of YSNe Ib/c, coming from the interaction of the SN shock with a dense hydrogen rich CSM far away from the stellar envelope.

The detection prospects of nearby YSNe with existing and upcoming gamma-ray and neutrino telescopes have also been explored. Among all YSNe, Type IIn SNe have the best discovery potential up to $\sim$ 10 Mpc ($\sim$ 4 Mpc) in gamma-rays with Fermi-LAT and CTA (in neutrinos with IceCube, KM3NeT and IceCube-Gen2). Among the remaining Types, II-P and Ib/c (LT) are found to be detectable up to a few Mpc, while the others (IIb/II-L and normal Ib/c) are detectable at kpc scale only. Interestingly, CTA may be able to distinguish gamma-ray attenuation features in the spectral energy distributions for nearby transients. However, a possible amplification of magnetic field, e.g. due to effect like Bell non-resonant streaming of cosmic rays, might influence proton acceleration and the resultant gamma-ray spectra (see e.g., 228; 229; 230). Multi-messenger observations of such point sources will be crucial to probe these mechanisms.

In addition to the conventional Ib/c YSN scenario, we have briefly explored the Ib/c (LT) YSN case in this chapter. We have considered the density profile of Ib/c (LT) to be wind like one. However, different studies in the literature reveals possible deviation from wind profile leading to different CSM density profiles. In the subsequent chapter, we look in to the impact of these CSM models on the emission of gamma-rays and high energy neutrinos.

Chapter 4

Point source: A closer look at SN 2014C

The X-ray and radio observations of SN 2014C have unveiled interactions with a dense hydrogen-rich medium far away from its progenitor. Understanding the origin and characteristics of this CSM is still not complete. The analysis of available data has revealed different plausible CSM profiles. In this chapter, we explore the various CSM profiles proposed in the literature for explaining observation of SN 2014C and analyse their potential effects on the fluxes of gamma-rays and high-energy neutrinos, secondaries generated as a result of shock-CSM interaction. We also conduct an assessment of the prospects for detecting future events similar to SN 2014C with current and upcoming gamma-ray and high-energy neutrino experiments.

4.1 Implications of SN 2014C observations

Early multi-wavelength observations of SN 2014C have shown the signatures of a Type Ib supernova. Supernovae (SNe) Ib and Ic, together labelled as Ib/c are hydrogen poor supernovae and among the dominant SN types (26%) in the local universe (231). Typically, the light curve of a SNe Ib/c fades after a few weeks (232; 233; 149). However, recent observations of SN

2014C, a SN of Type Ib/c, have revealed that a fraction of SNe of Type Ib/c exhibits evidence of late rebrightening at a few $\mathcal{O}(100)$ days (234; 207; 217). Such rebrightening resembles the behavior of a hydrogen-rich SN (i.e. a SN of Type IIn). Due to this peculiar feature, SN 2014C has also been referred to as the"chameleon SN" (207).

The late time (LT) rebrightening may result from the interaction of the SN ejecta with a dense circumstellar medium (CSM) surrounding the dying star. Observations of SN 2014C suggest that the shock may have interacted with a dense hydrogen (H) rich CSM located at larger radii. Such CSM structure could be due to the ejection of the H envelope a few centuries prior to explosion or the interaction of a Wolf-Rayet star wind with a dense red-supergiant wind (42; 207). In addition, evidence for an asymmetric CSM hints towards an explosion occurring within a binary system (235; 236). The dense hydrogen rich CSM of SN2014C is found to be located at about 10^{16}–10^{17} cm, which is at a distance far away from the stellar envelope ($\sim 10^{11}$ cm) and has a mass of about 1–2 $M_\odot$ (207; 237; 42). Such dense CSM has also been observed for different types of core collapse SNe (37; 38; 39; 137).

For a wind-like CSM, the CSM density depends on the mass-loss rate ($\dot{M}_{\rm W}$) and the wind velocity ($v_{\rm W}$). The CSM of conventional SNe Ib/c in the first few 100 days (early phase) exhibits $\dot{M}_{\rm W} \in [10^{-7}, 10^{-4}]$ $M_\odot$ yr^{-1}, with $v_{\rm W}$ being approximately 10^2–10^3 km s^{-1} (37). However, $\dot{M}_{\rm W}$ estimated for SN 2014C after about 200–300 days (late phase) is $\mathcal{O}(1)$ $M_\odot$yr^{-1} (207), with $v_{\rm W} \in [10, 10^3]$ km s^{-1} that corresponds to a CSM density $\sim 2 \times 10^6$ cm^{-3} at 6×10^{16} cm and then falls as a function of the radius as r^{-2}. Analysis of the available X-ray data suggest a constant CSM density up to 8×10^{16} cm which then falls following $r^{-2.5}$ (42). Recent work focusing on the X-ray data from SN 2014C instead infers two different density profiles (238). One of these density profiles scales as $r^{-1.5\pm0.01}$, while the other one has a steeper profile falling as $r^{-2.42\pm0.17}$. Interestingly, this analysis reports that the LT emission from SN 2014C is due to a dense H-rich disk resulting an asymmetric CSM. These conclusions are in contrast with the model based on a spherically symmetric CSM density profile falling as r^{-3} (237). Nevertheless, it is clear that the CSM of SN 2014C is different from the ones usually observed with wind-like CSM (i.e., r^{-2} profile).

Similar LT features have been observed for SNe 2003gk, 2004cc, 2004dk, 2004gk, and 2019yvr (207; 238; 43; 218; 239); additional examples of past SNe Ib/c showing indirect evidence of similar LT activity have been reported in Refs. (207; 238). All these SNe initially

showed properties of usual SNe Ib/c, but later evolved into IIn-like SNe with dense CSM. By relying on current observations, the fraction of SNe Ib/c with LT emission is expected to be about 2.6% of core-collapse SNe (207; 240). In the following, we assume SN 2014C as representative of this class of chameleon SNe.

The interaction of the SN ejecta with the CSM may lead to the production of secondary particles, such as neutrinos and gamma-rays, via inelastic proton-proton ($p-p$) collisions (29; 146; 147; 148; 149; 150; 151; 152; 153; 154; 155). The flux of neutrinos and gamma-rays from the conventional early phase of SNe of Type Ib/c was found to be faint, with poor detection prospects (the detection horizon being estimated to be around 2–6 Mpc) (33; 241; 242; 34). However, due to the presence of the dense hydrogen rich CSM at large radii, the fluxes of neutrinos and gamma-rays from SNe Ib/c LT can be larger than the ones expected in the early SN phase.

Different CSM density profiles may yield different fluxes of neutrinos and gamma-rays. Therefore, the detection of these secondary particles could be crucial to disentangle the properties of the CSM as well as probe the shock acceleration mechanism. In this chapter, we consider the aforementioned CSM profiles to compute the expected fluxes of neutrinos and gamma-rays and discuss their detection prospects with current and upcoming gamma-ray (Fermi-LAT and CTA) and neutrino (IceCube, IceCube-Gen2 and KM3NeT/ARCA) telescopes.

4.2 Modeling of the circumstellar medium

Our understanding of the CSM density profile of SN 2014C is still uncertain and different scenarios have been proposed in the literature (207; 42; 237; 238). In this section, we consider the following CSM models:

- Model A—A spherically symmetric and dense CSM. The CSM density is assumed to be constant ($n_{\rm CSM} \simeq 10^6$ cm^{-3}) between the inner radius, $r_{\rm i} \simeq 6 \times 10^{16}$ cm and the break radius $r_{\rm b} \simeq 8 \times 10^{16}$ cm (42). The CSM density beyond $r_{\rm b}$ falls as $r^{-2.5}$ up to the outer radius, $r_{\rm o} \simeq 2.5 \times 10^{17}$ cm. The origin of the constant CSM is not well understood. It may originate from the interaction of a short lived Wolf-Rayet star wind with the remnant of a dense red supergiant wind (240), due to mass loss (243), or to the ejection of the H

envelope caused by binary interactions (42).

- Model B—An asymmetric CSM model (238). The asymmetry is proposed to be caused by the H-rich disk in the equatorial plane and the observed X-ray emission from SN 2014C is attributed to this disk like CSM (238). Two different density profiles have been proposed for the disk, one with a density profile falling as $r^{-1.50\pm0.01}$ and the other with a steeper profile of the form $r^{-2.42\pm0.17}$. We take into account both density profiles: Model B1 ($r^{-1.5}$) and Model B2 ($r^{-2.42}$).

  To model the asymmetric CSM scenario, we introduce a geometrical (asymmetry) factor, f (≤ 1)(238). The case $f = 1$ corresponds to spherical symmetry in the CSM and the most asymmetric (disk-like) CSM is described by $f = 0.1$. The degree of the asymmetry of the CSM of SN 2014C is still uncertain. Therefore, to take into account the possibility of different asymmetric scenario f is varied between 1.0 and 0.1 (238). The variation of the CSM density is proportional to f for Model B1, whereas it scales as $\sqrt{f}$ for Model B2. The asymmetry factor, f is multiplied to the CSM density to obtain its impact.

We assume that the CSM ends abruptly at the outer radius, r_o, for Models A and B. The location of the CSM over density is uncertain (207; 237; 238), hence we choose to keep the location unchanged in both models. Note that these CSM profiles are different with respect to the conventional wind one ($\propto r^{-2}$ (207)), which was considered in Chapter 3. Here we refer the reader to Ref. (241; 34) for dedicated work on the production of neutrinos and gamma-rays for the CSM wind profile.

4.3 Particle acceleration and Secondary production

As discussed in Chapter 3, the interaction material expelled by SN explosion with such CSM can form collisionless high speed shock leading to particle (protons) acceleration to high energies. The spectral energy distribution of accelerated protons is assumed to be a power-law distribution, $Q_p^{inj}(E_p, r) \propto E_p^{-\alpha} \exp\left[-E_p/E_{p,max}(r)\right]$, where α is the power law index (170; 244; 29; 35; 40; 36; 33). We consider $\alpha \in [2.0, 2.2]$ for our analysis (34; 245; 61; 62). The choice of α depends on the details of the shock acceleration mechanism, also responsible for efficiently

accelerating protons up to PeV energies. In particular, magnetic field amplification can be considered to be the primary requirement for efficient acceleration (246; 247). For example, plasma instabilities may give rise to small scale magnetic field (32). Non-resonant hybrid (NRH) instability (228; 248; 249; 250; 251) in YSNe is another possibility. Such instability investigated for SN remnants (228) shows that cosmic rays (CRs) in the upstream shock can excite turbulence amplifying the initial background magnetic field. Such amplification can lead to long confinement of CRs allowing for acceleration to very high energies. In the SN remnant environment, the interaction of the strong shock with the upstream CRs is considered to be the requirement for the NRH instability. Similar amplification in YSNe also becomes feasible due to the high shock speed ($\sim 0.1c$) produced by these objects, see e.g. Ref. (250) for more details.

The maximum proton energy, $E_{\rm p,max}(r)$, governs the shape of the proton spectra at higher energies. $E_{\rm p,max}(r)$ is determined by balancing the acceleration timescale with the cooling timescales, i.e., $t_{\rm acc}(r) = \min[t_{\rm ad}(r), t_{\rm pp}(r)]$, where $t_{\rm ad}$ and $t_{\rm pp}$ are the cooling timescales for adiabatic losses and $p-p$ collisions, respectively. The acceleration timescale is given by $t_{\rm acc} = 6E_{\rm p}c/eBv_{\rm sh}^2$ in the Bohm limit, where B is the magnetic field strength of the post shock CSM given by $B = 3/2[4\pi\varepsilon_{\rm B}m_{\rm p}n_{\rm CSM}(r)v_{\rm sh}^2]^{1/2}$ (35). The fraction, $\varepsilon_{\rm B}$, of the post shock thermal energy converted to magnetic energy (35) can be estimated from SN radio observations and is typically in the range 10^{-3}–10^{-2} (234; 207; 34; 241; 252). The shock velocity, $v_{\rm sh}$, slowly decreases as a function of the radius, therefore we assume that it is constant, $\mathcal{O}(10^4)$ km s^{-1} (38; 40; 252; 207; 237; 42; 238). For a typical LT YSN, with $n_{\rm CSM} \sim 10^6$ cm^{-3}, $v_{\rm sh} \sim 10^4$ km s^{-1}, $\varepsilon_{\rm B} \sim 10^{-2}$, and $B \sim \mathcal{O}(1)$ G. This large magnetic field can ensure long confinement of protons in the shocked CSM accelerating them to very high energies; see Refs. (253; 32). The acceleration timescale for YSNe remains competitive to the different loss timescales. In particular, the acceleration of protons may be limited by cooling process as well as dynamical losses. The cooling processes include inelastic $p-p$ interactions and different photo-hadronic interactions such as photopion and photopair production. However, it has been shown for YSNe that photo-hadronic interactions are suppressed due to the low energy of the target photons (253; 254; 35; 45). Hence, the only relevant loss timescales are dynamical or adiabatic and the $p-p$ collision timescales . The adiabatic timescale is defined as $t_{\rm ad}(r) \sim r/v_{\rm sh}$ and the $p-p$ interaction timescale is given by $t_{\rm pp}(r) = [\kappa_{\rm pp}\sigma_{\rm pp}n_{\rm CSM}(r)c]^{-1}$, where $\kappa_{\rm pp} = 0.5$ is the proton inelasticity and $\sigma_{\rm pp}$ is the $p-p$ interaction cross-section (29). For a typical LT YSN scenario (see Table 4.1), these timescales are $t_{\rm acc} \sim 6\times10^5(E_{\rm p}/{\rm PeV})$ s,

$t_{\rm ad} \sim 6 \times 10^7$ s, $t_{\rm pp} \sim 10^8$ s. In addition, the diffusion of particles may also affect the acceleration as well as the $p-p$ interaction. For a Kolmogorov like diffusion (255), the diffusion timescale is, $t_{\rm diff} \sim 10^9/\sqrt{E_{\rm p}/{\rm PeV}}$ s. This shows that the acceleration timescale for PeV protons is significantly smaller than the relevant loss timescales. Thus, the acceleration of protons to PeV energies in a LT YSN environment can be possible due to such short timescale i.e., a few years.

The dependence of the maximum proton energy, $E_{\rm p,max}(r)$ on the parameters discussed above can be obtained from the relation, $t_{\rm acc}(r) = \min[t_{\rm ad}(r), t_{\rm pp}(r)]$. In particular, $E_{\rm p,max}(r)$ depends on $\varepsilon_{\rm B}$, $v_{\rm sh}$ and $n_{\rm CSM}$. Larger $v_{\rm sh}$ and $\varepsilon_{\rm B}$ are responsible for larger $E_{\rm p,max}(r)$, while a denser CSM slows down the shock, leading to a smaller $E_{\rm p,max}(r)$. Other possible losses, such as synchrotron or inverse Compton losses, are negligible, see e.g. Ref. (241). In addition to these loss timescales, the confinement time of the protons needs to be larger than the acceleration timescale to prevent the particles from escaping the acceleration region. This requires the maximum wavelength of the scattering turbulence ($\lambda_{\rm max}$) to be larger than the gyro-radius ($r_{\rm g}$) of the particles (256). The turbulence could be caused by the interaction of the accelerated protons with the upstream CSM (228). However, if $\lambda_{\rm max} \ll r_{\rm g}$, the maximum proton energy, $E_{\rm p,max}(r)$ could be smaller than PeV (35). Hence, the detection of secondary signals (gamma-rays and neutrinos) and their energy will provide crucial information on the acceleration efficiency.

The accelerated protons colliding with the CSM can lead to inelastic $p-p$ interaction giving rise to secondaries such as gamma-rays and high energy neutrinos. The fluxes of these secondaries depend on the CSM density profiles as well as on the accelerated proton distribution. It is worthwhile to note that gamma-rays can suffer attenuation due to pair production losses on the thermal photons in the source, while neutrinos remain unaffected being weakly interacting. Thus, the estimation of gamma-ray flux requires consideration of these source absorption as well. For the details on the modelling of the fluxes of these secondaries, the reader is referred to Chapter 3 as well as Ref. (257).

Table 4.1: Characteristic model parameters of SN Ib/c emission, inspired by observations of SN 2014C. The second column lists the model parameter typical of the early phase with a wind density profile (r^{-2}) (241). The third column represents the parameter values for the LT emission. Uncertainties on the LT parameters are also reported in the fourth column.

Parameters	**Early phase**	**Typical value (LT)**	**Uncertainty range (LT)**
v_{sh} (km s^{-1})	2×10^4	10^4	$(4–45) \times 10^4$
r_i (cm)	3×10^{11}	6×10^{16}	$(5.5–6) \times 10^{16}$
r_o (cm)	6×10^{16}	2.5×10^{17}	$(1–2.5) \times 10^{17}$
n_{CSM} (cm^{-3})	2×10^{12}	2×10^6	—
ε_p	10^{-1}	5×10^{-2}	10^{-2}–10^{-1}
ε_B	10^{-2}	1.5×10^{-2}	10^{-3}–10^{-2}
D_L (Mpc)	14.7	14.7	14.1 – 15.3
Onset time	180 s	250 days	(100–400) days
Declination	34^o		—

4.4 Temporal evolution and energy distribution of neutrino and gamma-ray signals

Because of the LT CSM interaction, we expect copious production of gamma-rays and neutrinos about a year after the SN explosion, and the time evolution of the neutrino and gamma-ray signals should carry crucial information about the CSM properties. For the calculation of the gamma-ray and neutrino fluxes, our choice of the benchmark SN model parameters is motivated by the observations of SN 2014C (207; 42; 217) and summarized in Table 4.1. Note that the parameters in Table 4.1 are the ones common to all CSM models introduced in Sec. 4.2; the differences among the models are due to the radial evolution of the CSM density profile between r_i and r_o and the asymmetry parameter f.

Figure 4.1 shows the temporal evolution of the flux of gamma-rays (thick red) and muon neutrinos (thin blue) at Earth for SN Model B1 ($r^{-1.5}$ profile). The continuous and dashed lines show the cases of minimum ($f = 1$) and maximum ($f = 0.1$) asymmetry of the CSM, respectively (238). The initial emission (up to 250 days, left panel) is small as the CSM for

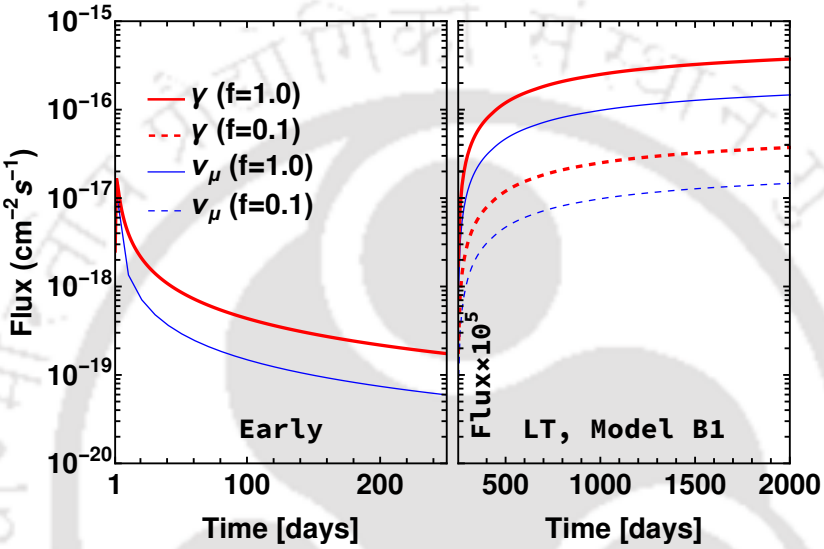

Figure 4.1: Temporal evolution of the flux of muon neutrinos (thin blue) and gamma-rays (thick red) at Earth from SN Model B1 (see also Table 4.1). The left plot extends up to 250 days and it shows the early emission from SN Ib/c; the right panel shows the LT emission, i.e. beyond 250 days. The y-axis of the right panel is rescaled by a factor 10^5 at 250 days. The continuous and dashed line styles represent the minimum ($f = 1$) and maximum ($f = 0.1$) CSM asymmetry, respectively. Note that the gamma-ray distributions do not take into account absorption. One can see that the early time emission from SNe Ib/c is significantly smaller than the corresponding LT emission. The other SN models (A and B2) show a similar temporal evolution and are therefore not shown.

SNe Ib/c is thin (241; 33). The sharp rise (note the re-scaling of the y-axis at 250 days, right panel) in the gamma-ray and neutrino spectra is due to the dense H-rich CSM. These fluxes are computed up to 2000 days that correspond to the outer radius r_o of the CSM.

The energy fluxes for SN Model B1, plotted in the top panel of Fig. 4.2 for gamma-rays (on the left) and muon neutrinos (on the right), reveal the dependence of the production mechanism on the SN model parameters. The curves in different colors and line styles represent fluxes at different time snapshots (255, 1000, 1500, and 2000 days), highlighting the flux variation over the LT phase. This panel also shows the flux averaged over 2000 days (black curve). Contrasting the flux at 255 days (corresponding to the onset of the shock-CSM interaction) with the one above 1000 days, one can see that the flux tends to increase with time. The maximum proton energy, $E_{\rm p,max}(r)$, fixes the spectral shape at higher energies as it acts as an exponential cut-off (see Sec. 4.3). Hence, the fluxes of both gamma-rays and neutrinos fall rapidly above 10^3 TeV.

The gamma-ray fluxes in the top left panel of Fig. 4.2 include absorption effects. In order to estimate the amount of absorption, the average energy and luminosity of thermal photons are assumed to be 0.05 eV and 5×10^{40} erg/s (42; 207). The gamma-ray fluxes show dips of different sizes due to pair production losses on the ambient thermal photons. The dips have different sizes as the optical depth $\tau^{\rm S}_{loss}(E'_\gamma, r)$ falls with the radius (241); this implies that the gamma-rays produced at larger radii have smaller attenuation. However, the attenuation during propagation due to the EBL is not significant since SN 2014C is at 14.7 Mpc (241); therefore we neglect this effect.

The bottom panel of Figure 4.2 shows the fluxes averaged over 2000 days for Model A, B1, and B2 (medium thick, thinnest and thickest, respectively). It is important to note that the fluxes for Model B depend on the CSM asymmetry factor f. The spectral shape remains the same for different f, but the normalization changes. For example, if we increase f to 1, the time-averaged flux of Model B1 would be larger than the ones of the other CSM models. Note that the time-averaged fluxes of gamma-rays and neutrinos (black curves) are smaller than the maximum fluxes (at 2000 days) by a few factors. Hence, in the following, we consider the time-averaged fluxes to be conservative estimates of the detection prospects of SN 2014C-like events.

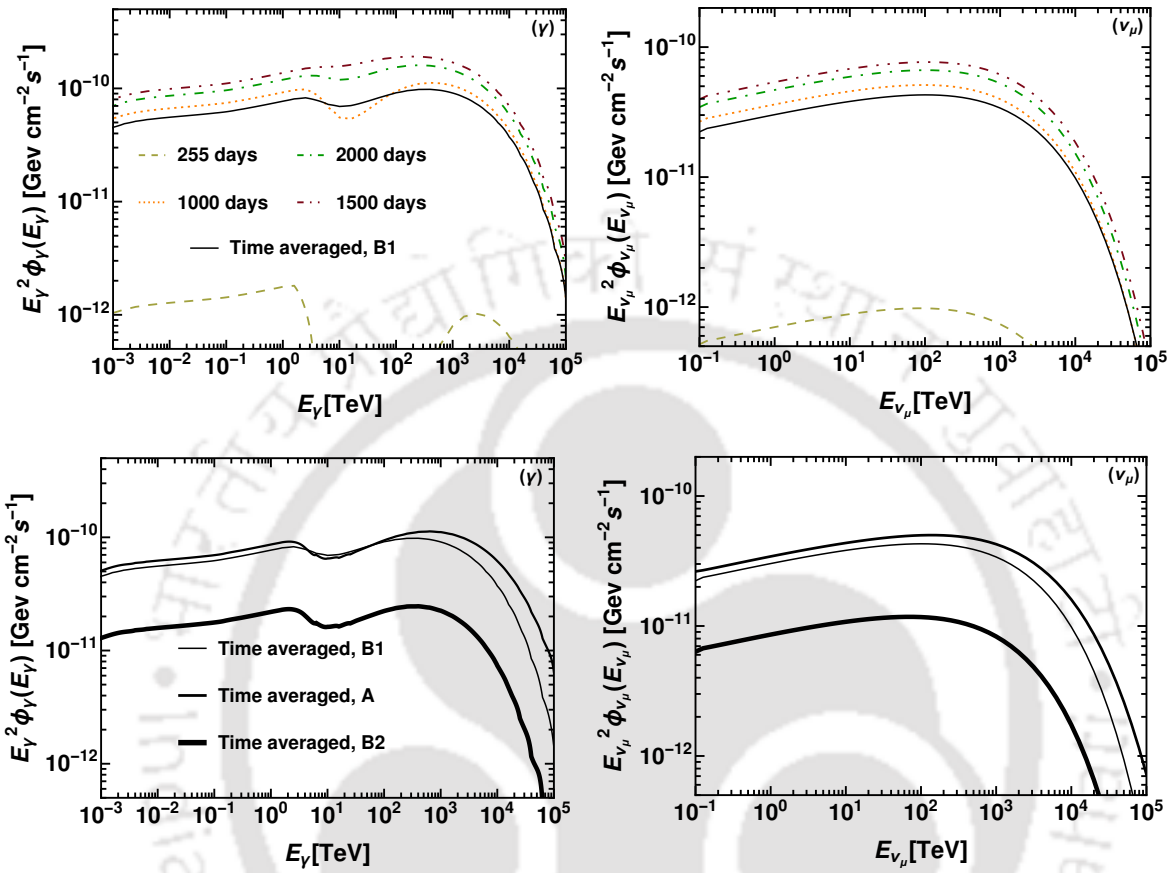

Figure 4.2: *Top:* Time snapshots of gamma-ray (on the left) and muon neutrino (on the right) fluxes as functions of the energy for SN Model B1 (see Table 4.1 for more details on the model parameters). The different curves indicate the flux at 255, 1000, 1500, and 2000 days. We consider the asymmetry factor to be $f = 0.5$ to describe the typical spectral variation over the late emission phase. After the onset of the LT interaction, the fluxes increase with time. The fluxes averaged over 2000 days has also been shown by the black curves. The gamma-ray fluxes between 1–10^3 TeV are attenuated by pair production on the SN thermal photons. The amount of absorption is initially large, but it becomes smaller with time as the thermal photon density falls rapidly with the radius. *Bottom:* The fluxes of gamma-rays (left) and neutrinos (right) averaged over 2000 days for Model A (medium thick), B1 (thinnest), and B2 (thickest) are shown for guidance.

4.5 Detection prospects for SN 2014C-like bursts

In this section, we explore the detection prospects of gamma-rays and neutrinos from SNe Ib/c LT with current and upcoming gamma-ray (Fermi-LAT and CTA) and high energy neutrino (IceCube, IceCube-Gen2 and KM3NeT/ARCA) detectors (30; 258; 25; 73; 259). For comparison, we consider Model B1 and Model B2 with CSM asymmetry $f = 0.5$.

Current and future detection prospects

The left (right) panel of Fig. 4.3 shows the gamma-ray (neutrino) flux for different models of the CSM, as well as the detection sensitivity of gamma-ray (neutrino) telescopes. The sensitivity curves of Fermi-LAT and CTA shown in the left panel correspond to 4 years and 50 hours of observation time, respectively. Whereas we show the 6 year sensitivities of the neutrino detectors in the right panel. The SN model parameters are plagued by various uncertainties. In order to take this into account, we consider a range of variability for the microphysical parameters that contribute to the largest uncertainty in the expected fluxes; we take α, ε_p and ε_B to vary in the range 2.0–2.2, 10^{-2}–10^{-1} and 10^{-3}–10^{-2}, respectively (234; 207; 34; 241). The shaded bands in both panels of Fig. 4.3 also take into account the uncertainties on the CSM profile and the asymmetry factor f. Note that the conventional wind profile (r^{-2}) with our benchmark parameters (Table 4.1) leads to fluxes similar to the ones of Model B1 with $f = 0.5$ (241). It is interesting to note that LHAASO holds sensitivity similar to CTA at around 100 TeV and hence, will be able to probe such gamma-ray fluxes (126). On the other hand, the sensitivity of HAWC is significantly lower in comparison to CTA and LHAASO.

While the detection prospects are less optimistic for Fermi-LAT, CTA may detect gamma-rays, if the CSM has a smaller asymmetry (i.e., $f \geq 0.5$) compared to the asymmetry for $f = 0.5$. On the other hand, the non-detection of gamma-rays with CTA may contribute to constrain the CSM asymmetry factor f. The forecasted neutrino flux is beyond reach for IceCube (6 years with 90% confidence level (CL), (258)), in agreement with the fact that SN 2014C was not detected in neutrinos—see e.g. Ref. (260). However, IceCube-Gen2 (6 years with 90% CL, (25)) will have a better sensitivity and be closest to the predicted flux. For bursts occurring

at closer distances than 15 Mpc, IceCube-Gen2 will have a reasonable prospect of detection. Interestingly, KM3NeT/ARCA (10 years with 90% CL, (259)) is expected to hold similar sensitivity as IceCube-Gen2 (6 years with 90% CL, (25)) and may probe similar SNe Ib/c LT objects. However, due to the limited availability of the KM3NeT/ARCA sensitivity for the energy bins over the point source observation time, it is difficult to make a precise estimate of the detector response and therefore we choose to do not explicitly show the detection prospects of KM3NeT/ARCA in Fig. 4.3. Also, any comparison of the detector sensitivities with the predicted neutrino fluxes only provides a broad idea about the detection prospects. This is because of the different sensitivities at different energy bins (261; 258). For a robust forecast, one should compute the number of events considering the impact of the backgrounds. Since our neutrino flux prediction has large astrophysical uncertainties, we only investigate the differential flux sensitivities of the detector to give an idea of the detection prospects.

The secondary fluxes for the asymmetric CSM models are computed by assuming that the disk (which gives rise to the asymmetry in the CSM) is aligned with the observer's line of sight. When the disk is not along the line of sight, the fluxes might be smaller than the ones shown in Fig. 4.3. However, this uncertainty lies within the uncertainty bands shown in Fig. 4.3.

Detection horizon

The detection prospects of SNe with LT emission depend on the rate of such events. In the local universe, we expect about 26% SNe Ib/c (240), of these about 10% should be Ib/c LT (207). Thus, the local rate of SNe Ib/c LT is about 2.6% of the local core collapse SN rate ($1.25 \pm 0.5 \times 10^{-4}$ Mpc^{-3}yr^{-1} (262)).

To investigate upcoming detection prospects, we consider SN 2014C as the benchmark SN Ib/c LT (Table 4.1, third column) and calculate the SN detection horizon defined as the distance at which the source should be located, for which the energy integrated flux (averaged over 2000 days) falls below the telescope sensitivity. The energy range for these integrated fluxes is optimized according to the telescope sensitivity. For Fermi-LAT and CTA, we consider 10^{-4}–10^{-2} TeV and 5×10^{-2}–5×10^{1} TeV respectively, whereas we focus on 10^{2}–10^{4} TeV for the neutrino telescopes. Note that the sensitivity for the neutrino telescopes depends on the

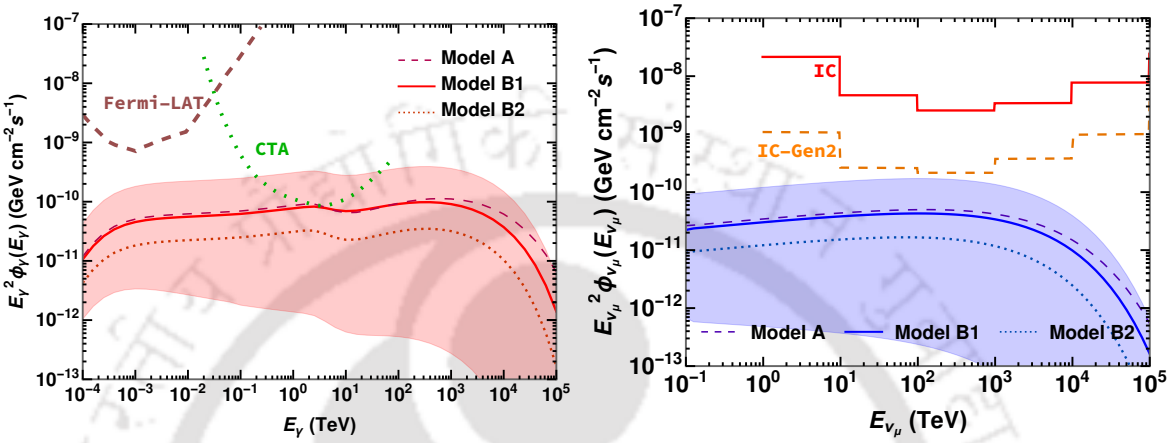

Figure 4.3: *Left:* Time averaged gamma-ray flux for different CSM models (see Table 4.1). The red band represents the time-averaged flux of SN Ib/c LT obtained considering the uncertainties in the model parameters ($\varepsilon_P \sim 10^{-2}$–$10^{-1}$, $\varepsilon_B \sim 10^{-3}$–$10^{-2}$ and $f \sim 0.1$–1), while the other model parameters are kept fixed as detailed in Table 4.1. The uncertainty band as been obtained as follows: for the upper limit, we take $\alpha = 2.0$, $\varepsilon_{\rm p} = 10^{-1}$, $\varepsilon_{\rm B} = 10^{-2}$ and $f = 1$ for Model B1; for the lower limit, we choose $\alpha = 2.0$, $\varepsilon_{\rm p} = 10^{-2}$, $\varepsilon_{\rm B} = 10^{-3}$, and $f = 0.1$ for Model B2. The red continuous and dotted curves show the fluxes for Model B1 and Model B2, respectively, for $f = 0.5$. The pink dashed curve represents the flux for Model A. The sensitivities of Fermi-LAT (4 years) and CTA (50 hours) are plotted in brown and green, respectively. CTA may be able to detect gamma-rays from SNe closer than $\simeq 15$ Mpc. *Right:* Corresponding neutrino flux and sensitivities of IceCube (6 years with 90% CL) (258), IceCube-Gen2 (6 years with 90% CL) (25). The blue band represents the uncertainty in the model parameters. The sensitivity chosen for IceCube corresponds to the one at the declination of 0° where IceCube is most sensitive. Neutrinos from SNe Ib/c LT may be detectable for bursts occurring closer than 15 Mpc.

declination (30; 258; 25). Hence, unlike the gamma-ray telescopes, we consider a maximum and minimum sensitivity resulting in a band.

Figure 4.4 shows the detection horizon for gamma-rays (left) and neutrinos (right). The left panel only shows the detection horizon of CTA; Fermi-LAT is not shown because of its weak sensitivity and different energy range compared to CTA (see Fig. 4.3). The gamma-ray fluxes for Model B1 and Model B2 are represented by red continuous and dotted curves respectively, while the pink dashed line shows the flux for Model A. The shaded bands in both panels correspond to the uncertainty in the parameters ($\alpha \in [2.0-2.2]$, $\varepsilon_P \in [10^{-2}, 10^{-1}]$ and $\varepsilon_B \in [10^{-3}, 10^{-2}]$) and CSM asymmetry factor ($f \in [0.1, 1]$) as in Fig. 4.3. The horizontal dotted line represents the sensitivity of CTA. The detection horizon for CTA extends up to 10 Mpc, while the detection horizon of Fermi-LAT is limited to 4 Mpc (results not shown here). Interestingly, the density profile of the CSM for SN (Model B1 and Model B2) plays an important role in the detectability of such SNe. For example, the detection horizon of CTA is about 10 Mpc for Model B1 and about 6 Mpc for Model B2. Note that the predicted gamma-ray flux is consistent with the upper limits on the diffuse gamma-ray flux at PeV energies from Carpet-2 experiment (263). For comparison, the upper limit on the diffuse flux at 10 PeV is about 10^{-7} GeV cm^{-2} s^{-1} sr^{-1}.

The detection horizons of current and upcoming neutrino telescopes are shown in the right panel of Fig. 4.4. The blue continuous and light-blue dotted lines show the integrated ν_μ flux as a function of the SN distance (Mpc) for SN Model B1 and Model B2, respectively, and the purple dashed line corresponds to Model A. The blue band takes into account the model uncertainties (α, $\varepsilon_{\rm p}$, $\varepsilon_{\rm B}$, f). The upper and lower limits of the sensitivity of neutrino telescopes depend on the SN declination angle and are shown as bands in Fig. 4.4. The most optimistic model prediction (upper limit of blue band) and most sensitive future telescopes (lower limit of orange and green bands) combination imply that SNe Ib/c LT may be detected up to 10 Mpc with IceCube-Gen2. On the other hand, the detection horizon of IceCube (red band) is limited to about 4 Mpc.

For guidance, we also show in Fig. 4.4 the gamma-ray and muon neutrino fluxes of SN 2014C that occurred at 14.7 Mpc as well as the ones of SN 2019yvr observed at 22 Mpc (218). The flux of SN 2014C (black inverted triangle) is obtained by relying on the same parameters as the ones of the blue line. As for SN 2019yvr, we have chosen $r_{\rm i} = 3 \times 10^{16}$ cm (264; 218), $\varepsilon_{\rm p} = 0.1$, and $\varepsilon_{\rm B} = 0.01$ to compute the flux upper limits. The other parameters for SN 2019yvr

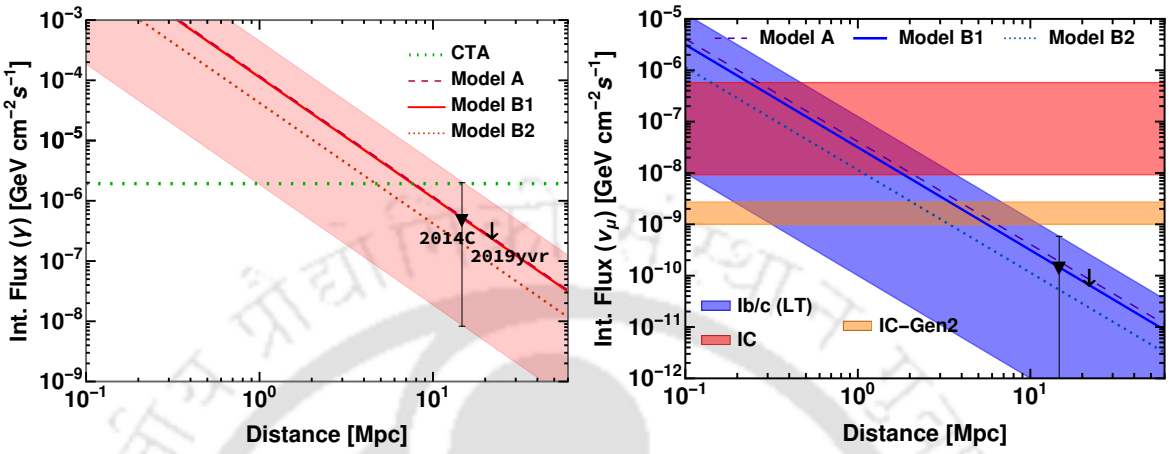

Figure 4.4: *Left:* Detection horizon (see main text for details) in gamma-rays for SNe Ib/c LT. The time-averaged gamma-ray flux has been integrated over energy in the range 5×10^{-2}–5×10^{1} TeV for SN Model B1 (red) and Modlel B2 (red dotted) for an asymmetry factor $f = 0.5$. The pink dashed line represents the flux for SN Model A, slightly overlapping with the SN Model B1 flux. The red band corresponds to the uncertainties in the parameters $\alpha \in [2.0 - 2.2]$, and $\varepsilon_P \in [10^{-2}, 10^{-1}]$ and $\varepsilon_B \in [10^{-3}, 10^{-2}]$, and $f \in [0.1, 1]$. The horizontal dotted line represents the CTA sensitivity. The detection horizon is about 10 Mpc. *Right:* Corresponding detection horizon for neutrinos. The blue band represents the time-averaged flux integrated in the range 10^2–10^4 TeV. The purple dashed, blue and light blue dotted lines show the fluxes for the SN Model A, Model B1 and Model B2 respectively. The 90% CL sensitivity bands of different detectors are obtained by considering the variation of the declination angle (δ) of the source. The band for IceCube corresponds to the minimum detector sensitivity for $\delta = -60^\circ$ (30) and maximum detector sensitivity, $\delta = 0^\circ$ (258). Similarly, we consider $\delta = 30^\circ$ (minimum) and $\delta = 0^\circ$ (maximum) for IceCube-Gen2 (25); IceCube-Gen2 has the potential to detect SNe Ib/c LT up to 10 Mpc, while IceCube can only probe SNe up to 3 Mpc. For guidance, the black data points in both panels show the fluxes of recent nearby SN Ib/c LTe: SN 2014C and SN 2019yvr.

are the same as in Table 4.1, due to limited information otherwise available for them. Both these events lie beyond the detection horizon of gamma-ray and neutrino telescopes. These findings are in agreement with the non-observation of neutrinos with IceCube and gamma-rays with Fermi-LAT from SN 2014C and SN 2019yvr. Similar LT shock-CSM interaction has been observed in other SNe Ib/c, such as SN 2003gk (estimated distance: 45 Mpc (265)), SN 2004dk (estimated distance: 21.05 Mpc (43)), SN 2004cc (estimated distance: 18 Mpc (266)), and SN 2004gq (estimated distance: 26 Mpc (266)). Due to their larger or comparable distances, we do not include them in Fig. 4.4, since we expect comparable or worse detection prospects. Using the local SN rate (262) and the fraction of Ib/c observed, one can estimate the rate of such Ib/c SNe within the detection horizon of the telescopes, i.e, within 10 Mpc. Thus, the rate of Ib/c within the detection horizon can be expected to be 0.01 per year.

In Chapter 3 (see also 241), the discovery horizon of IceCube-Gen2 for SN 2014C-like events was found to be about 6 Mpc. However, here we report a detection horizon of 10 Mpc. This is because the results in Chapter 3 were based on a wind-like CSM profile (r^{-2}) whereas we consider different CSM profiles in this chapter (see Sec. 4.2). In addition, the sensitivity of IceCube-Gen2 corresponding to 5σ CL considered in Chapter 3 is smaller than the 90% CL sensitivity considered in this work. This also holds for the detection horizons of IceCube and KM3NeT/ARCA. The discovery horizon of CTA for SN 2014C-like events was found to be about 2–6 Mpc in Ref. (34) depending on the energy of gamma-rays and considering the SN emission up to 396 days, for a dense wind-like CSM (207). These conclusions are in agreement with our findings.

4.6 Conclusion

In this chapter, we have computed the fluxes of gamma-rays and high energy neutrinos from SNe Ib/c LT, considering SN 2014C as the prototype SNe Ib/c with LT emission. Because of the uncertainties related to the properties of the CSM, we have considered three different CSM models: Model A (symmetric, $r^{-2.5}$), Model B1 (asymmetric, $r^{-1.5}$) and Model B2 (asymmetric, $r^{-2.4}$). According to the CSM profile, we predict a range of variability for the expected fluxes of neutrinos and gamma-rays.

Based on the observation of SN 2014C and the uncertainties in the model parameters, we have investigated present and future detection prospects of SNe Ib/c LT in neutrinos and gamma-rays. We find that the detection horizon for Fermi-LAT and CTA is 4 Mpc and 10 Mpc, respectively. Similarly, for neutrinos, the detection horizon of IceCube is about 4 Mpc, while IceCube-Gen2 and KM3NeT/ARCA can potentially detect SNe Ib/c LT up to 10 Mpc and 6 Mpc respectively. However, the detection horizon in neutrinos can vary up to a few Mpc depending on the source declination. The highly symmetric CSM models are found to have the best detection prospects while increasing the asymmetry in the CSM worsens the detection prospects. Our findings are in agreement with the non-detection of gamma-rays and neutrinos from SN 2014C and SN 2019yvr and other SN bursts with LT emission occurring at larger distances. Yet, upcoming detection of neutrinos and gamma-rays from local SNe Ib/c LT will be crucial to probe the CSM properties and the nature of such transients.

In the preceding chapters, we have explored the interaction of SN ejecta with dense CSM which leads to the production of gamma-rays and high energy neutrinos in YSNe. Given the occurrence of YSNe throughout the history of the Universe, they have the capability to generate diffuse backgrounds of gamma-rays and high-energy neutrinos. In the subsequent chapter, we will look into the assessment of these diffuse backgrounds and explore their potential implications in the realm of multi-messenger astrophysics.

This page was intentionally left blank.

Chapter 5

Diffuse gamma-rays and high energy neutrinos from young supernovae

In this chapter, we make an attempt to establish a connection between the High Energy Starting Events data of IceCube neutrino observatory and the Isotropic Gamma-ray Background detected by Fermi Large Area Telescope through a common origin i.e, the young supernovae. For this, we will use the model of high energy neutrino and gamma-ray emission in young supernovae developed in Chapter 3.

5.1 Observations

In the following, we will provide a brief introtuction to the diffuse gamma-ray background observed by Fermi-LAT and the diffuse neutrino flux detected by IceCube. These backgrounds serve as the key drivers behind the focus of this chapter.

5.1.1 Isotropic Gamma-ray Background: Fermi Large Area Telescope

The Isotropic Gamma-ray Background (IGRB) represents the diffuse component of the Extra-galactic Gamma-ray Background (EGB) (267). The EGB comprises of all possible Extra-galactic individual and diffuse gamma-ray sources in the observable Universe. These sources include Active Galactic Nuclei (AGN), star-forming galaxies (SFG) and gamma-ray bursts (GRB). The first attempt of measurement of the IGRB was carried out in the year 2009 by the Large Area Telescope (LAT) (74), an onboard instrument in the Fermi Gamma-ray Space Telescope using 10 months of all sky survey data in the energy range between 200 MeV and 100 GeV. Estimation of the IGRB was obtained by subtracting the individual source Gamma-ray background from the total EGB. Later in 2014, the Fermi-LAT collaboration reported an updated measurement of the IGRB using 50 months of data survey and extending the range from 100 MeV to 820 GeV (267). The measured IGRB spectrum has revealed an interesting feature, i.e., a power law behaviour with an exponential cut-off. The spectral index is found to be 2.32 ± 0.02, whereas the cut-off energy is (279 ± 52) GeV (267). The total intensity of the IGRB above 100 MeV has been found to be $(7.2 \pm 0.6) \times 10^{-6}$ cm^{-2} s^{-1} sr^{-1} (267). The gamma-ray emission from blazars provide a good explanation to this IGRB, however a small component at GeV energies remains unexplained (77; 47; 104). A recent study, (268) shows that galaxy clusters can account for this unexplained flux. On the other hand, a recent study has shown that SFGs alone can explain the IGRB (160). Although these analyses provide robust explanation regarding the origin of the IGRB, possibilities of contribution from other astrophysical sources such as GRB and SNe are still open.

5.1.2 High Energy Starting Events: IceCube

The IceCube neutrino observatory located deep within the Antarctic ice sheet has made several groundbreaking discoveries over a decade. These discoveries include the PeV neutrino event from the direction of Blazar (21), high energy neutrinos from the Galactic plane (269), and the diffuse high energy neutrino flux known as the High Energy Starting Events (HESE) (48). The HESE particularly refers to the events above energy 60 TeV within the fiducial volume of the

detector (48). There are mainly two different types of events observed by IceCube: cascade and tracks. The cascade events refer to the showers of secondary particles produced by interaction (both charged and neutral current) of high energy neutrinos with ice (nucleus or electrons). On the other hand, the track events are produced by charged current interaction of high energy muon neutrinos with nuclei in the ice. The advantage of track events is their high angular resolution (less than a few degrees), over cascade events with poor angular resolution (a few tens of degrees). Hence, the track events are useful for point source detection. The HESE data include both cascade and track events observed over 7.5 years. The HESE data being compatible with isotropic flux models hints at Extra-galactic origin of these neutrinos (48). An interesting feature of the HESE events is that they exhibit a power law behaviour with a spectral index of $2.87^{+0.020}_{-0.19}$ at 68.3% confidence interval. Even though several astrophysical flux models exist in the literature (48; 270; 271; 272; 273; 274) providing explanation to these HESE events, the origin of these events remain uncertain.

Thus both the Fermi-LAT's IGRB and the IceCube's HESE flux show certain similarities such as power law behaviours and Extra-galactic origin. These similarities in the data of two different experiments point at the possibilities of some common origin of these high energy particles. Hadronic interactions such as $p-p$ and $p\gamma$ in cosmic acceleration sites are regarded as prime sources of such common origin. In the following, we will investigate the diffuse backgrounds of gamma-rays and high energy neutrinos from YSNe as a possible origin to these groundbreaking observations.

5.2 Diffuse gamma-ray and neutrino backgrounds from young supernovae

In this Section, we first introduce the procedure adopted to compute the diffuse backgrounds of high-energy particles. Then, we present our results on the diffuse gamma-ray and neutrino backgrounds from YSNe. A discussion on the model uncertainties and comparison with existing data follows.

5.2.1 Diffuse flux and its ingredients

The differences among the different YSNe classes for what concerns the emission of secondaries give rise to interesting questions regarding the contribution of each YSN class to the diffuse emission of gamma-rays and neutrinos. In addition to the individual YSN fluxes, the diffuse flux of secondary particles embeds the contribution from the redshift dependence of the various YSNe Types [1]:

$$E_{\mathrm{j,obs}}^2 \phi_{\mathrm{j,diff}}(E_{\mathrm{j,obs}}) = \zeta \frac{c}{H_0} \int_0^{z_{\max}} \mathrm{d}z \frac{R_{\mathrm{CCSN}}(z) E_{\mathrm{j}}^2 \phi_{\mathrm{j}}^{\mathrm{s}}(E_{\mathrm{j}})}{\sqrt{\Omega_m (1+z)^3 + \Omega_\Lambda}} e^{-\tau_{\mathrm{j,EBL}}(E_{\mathrm{j}},z)} , \tag{5.1}$$

where, $\mathrm{j} = \nu$ or γ, $E_{\mathrm{j}} = (1+z)E_{\mathrm{j,obs}}$ and $\tau_{\mathrm{j,EBL}}(E_{\mathrm{j}},z)$ is optical depth of EBL. For neutrinos, $\tau_{\nu,\mathrm{EBL}} = 0$. For gamma-rays, the optical depth $\tau_{\gamma,\mathrm{EBL}}$ is taken from Ref. (165). We adopt the ΛCDM cosmological model, with $\Omega_m = 0.31$, $\Omega_\Lambda = 0.69$, and $H_0 = 68$ km s^{-1}Mpc^{-1} (276).

The fluxes of gamma-rays and neutrinos at source, $\phi_{\mathrm{j}}^{\mathrm{s}}(E_{\mathrm{j}})$ are computed with the recipe discussed in Chapter 3. The fraction of different SN Types may vary with redshift due to the change in density of stars and metallicity of the host galaxies seen at higher redshifts. However, unfortunately, the redshift distribution of SNe of different Types is quite uncertain, and limited information is available up to $z = 1$, for some SN Types, which is not sufficient for our purposes (275). Hence, we assume that all SN Types follow the core-collapse SN rate as a function of the redshift. In addition, in order to take into account that some SN Types are more common than others, we follow Ref. (231) and assume that the fraction of different core-collapse SN Types at $z = 0$ (ζ) holds at higher z as well. The fraction of different SN Types at $z = 0$ is shown in Fig. 5.1.

The rate of core-collapse SNe is given by (277; 278; 279):

$$R_{\mathrm{CCSN}}(z) = \int_{8M_\odot}^{125M_\odot} \mathrm{d}M R_{\mathrm{SN}}(z,M), \tag{5.2}$$

where

[1] We assume a constant luminosity function based on the benchmark parameters introduced in Table 3.1, in light of the existing observational uncertainties (231; 275).

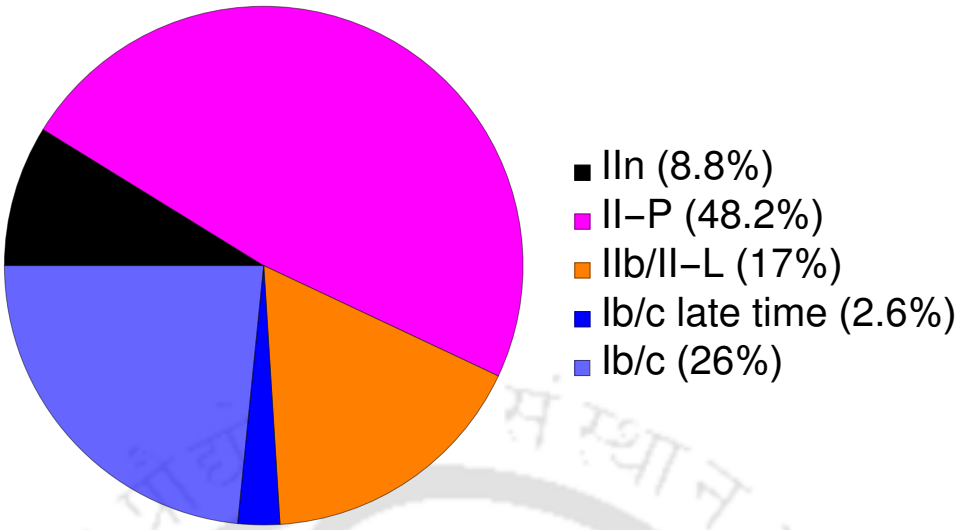

Figure 5.1: Local rate of core-collapse SNe (231). Type II-P SNe are the most abundant ones at $z = 0$. Type Ib/c and IIb/II-L SNe are also more frequent than Type IIn SNe. We assume Type Ib/c (LT) SNe to be 10% of SNe Ib/c (207); the total rate of SNe Ib/c (i.e., 26%) includes the one of Ib/c (LT) SNe.

$$R_{\rm SN}(z,M) = \frac{\eta(M)}{\int_{0.5M_\odot}^{125M_\odot} {\rm d}M M\eta(M)} R_{\rm SFR}(z), \tag{5.3}$$

with $\eta(M) \propto M^{-2.35}$ being the initial mass function (following the Salpeter law) (280). The star formation rate $R_{\rm SFR}$ is (281),

$$R_{\rm SFR}(z) = C_0 \left[(1+z)^{p_1 k} + \left(\frac{1+z}{5000}\right)^{p_2 k} + \left(\frac{1+z}{9}\right)^{p_3 k} \right]^{1/k}, \tag{5.4}$$

where $k = -10$, $p_1 = 3.4$, $p_2 = -0.3$ and $p_3 = -3.5$. The constant of proportionality C_0 is determined by normalizing the SN rate to the local SN rate as $\int_{8M_\odot}^{125M_\odot} {\rm d}M R_{\rm SN}(0,M) = 1.25 \pm 0.5 \times 10^{-4}$ Mpc^{-3}yr^{-1} (262).

5.2.2 Diffuse background of gamma-rays

The diffuse background of gamma-rays from YSNe can be computed by relying on Eq. 5.1. Because of $\gamma\gamma$ interactions occurring between YSN gamma-rays and the EBL, losses similar to the ones occurring in the source, and discussed in Sec. 3.2.2, can take place. Substantial EBL losses can affect the high-energy tail of the gamma-ray spectral distribution, while gamma-rays travel over large distances. For example, a 300 GeV gamma-ray photon would need to travel about 1 Gpc to be attenuated by an amount of $1/e$ (165).

In order to compute the amount of EBL absorption, one needs to know the redshift dependence of the EBL for different energies (181; 282; 165; 283). For this work, we model $\tau_{\gamma,\mathrm{EBL}}(E_\gamma)$ (see Eq. 5.1) following Ref. (165).

Fig. 5.2 shows the diffuse gamma-ray background for Type IIn YSNe ($\zeta \approx 0.9$, see Fig. 5.1) as a function of the observed photon energy. The red-dashed curve shows the gamma-rays produced through $p-p$ interactions (without any energy loss). The purple dot-dashed curve shows the diffuse flux with source absorption and EM cascade, where the small part of the flux at higher energies (above 10^3 GeV) for the purple dot-dashed curve is due to the $\gamma\gamma$ cross-section as discussed in Sec. 3.2.2. The red solid curve represents the gamma-ray flux after taking into account all the absorption (source+EBL) processes and EM cascades. The purple dot-dashed and red solid curves are larger than the dashed red curve (no absorption) below 100 GeV because of the additional cascaded flux.

The left panel of Fig. 5.3 displays the diffuse gamma-ray background for the different YSN Types by considering the benchmark values introduced in Table 3.1 and for $\alpha_{\mathrm{p}} = 2.0$. The largest contribution to the diffuse emission comes from Type IIn YSNe. The diffuse flux of Type II-P YSNe falls at around 20 GeV, i.e. at lower energies than Type IIn YSNe because the thermal photons of Type II-P YSNe have larger average energies than the ones of Type IIn YSNe ($\varepsilon_{av} = 1$ eV for IIn YSNe vs. $\varepsilon_{av} = 4.6$ eV for II-P YSNe). The diffuse flux of Type Ib/c (LT) YSNe falls at larger observed gamma-ray energies than the one of Type IIn YSNe because of the average energy of thermal photons. It has been found that Type II-P contributes small amount to the diffuse background at lower energies (below 10 GeV). Overall, the contribution of Type IIb/II-L, and Ib/c (LT) YSNe to the total diffuse gamma-ray background

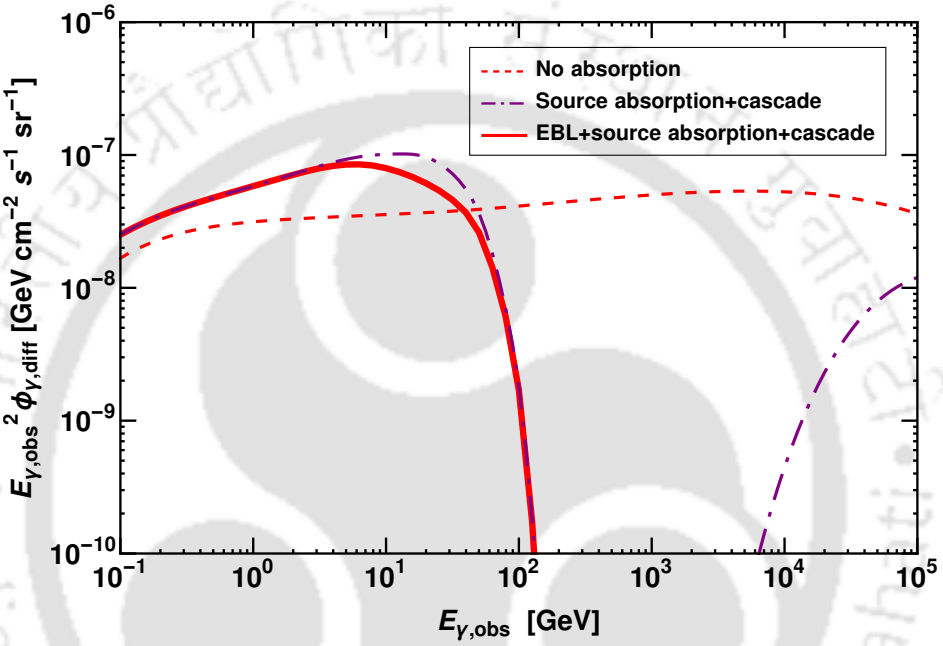

Figure 5.2: Diffuse gamma-ray flux at Earth for our benchmark Type IIn YSN (see Table 3.1). The red dashed curve corresponds to the diffuse gamma-ray flux without any absorption. The purple dot-dashed curve shows the diffuse flux after losses ($\gamma\gamma$ and Bethe-Heitler) and EM cascade at source. The final gamma-ray flux at Earth after EBL absorption is represented by the thick red solid curve. EBL absorption is more pronounced above 100 GeV. Moreover, the propagation loss in the diffuse flux has attenuated the higher energy tail above 10^4 GeV. Thus, the final diffuse flux peaks at around 10 GeV and ends abruptly around 100 GeV.

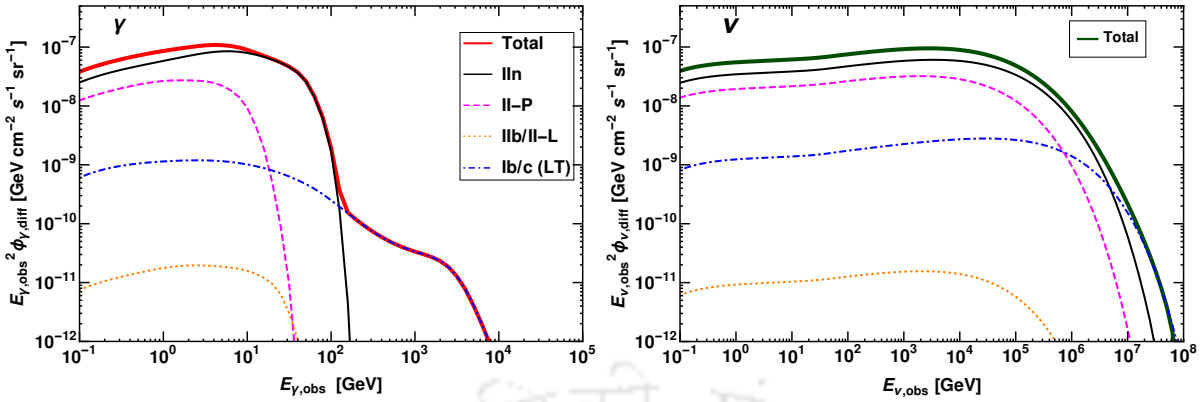

Figure 5.3: Diffuse gamma-rays (left) and all-flavour neutrinos (right) fluxes as functions of the observed particle energy for the different YSNe classes (see Table 3.1 for our benchmark model parameters). For both gamma-rays and neutrinos, Type IIn (black solid curves) YSNe contribute the most to the total diffuse emission, followed by Type II-P (magenta dashed curves) YSNe at lower energies. The contribution (despite being small) from Type Ib/c (LT) (blue dot-dashed curves) YSNe may show up above 10^2 GeV in gamma-rays, whereas in neutrinos above 10^7 GeV. Type IIb/II-L (orange dotted curves) YSNe contribute negligibly. The flux of Type Ib/c YSNe is not shown since it lies outside the plot range. The total diffuse gamma-ray and neutrino fluxes are plotted as thick red and thick green curves. It can be seen that IIn, II-P and Ib/c (LT) YSNe are the main contributors to the total diffuse spectra of both gamma-ray and neutrinos.

is negligible. However, a small diffuse flux of gamma-rays from Ib/c (LT) YSNe may show up above 10^2 GeV. Therefore, the total gamma-ray background (thick red curve) is mostly dominated by the contribution from Type IIn SNe.

5.2.3 Diffuse background of high-energy neutrinos

The diffuse background of high-energy neutrinos for the different YSN Types can be computed by relying on Eq. 5.1. The crucial difference with respect to the diffuse gamma-ray flux is the loss of the gamma-ray flux due to the propagation.

The diffuse background of high-energy neutrinos is shown in the right panel of Fig. 5.3 for our benchmark model parameters introduced in Table 3.1 and for $\alpha_{\mathrm{p}} = 2.0$. Similar to what

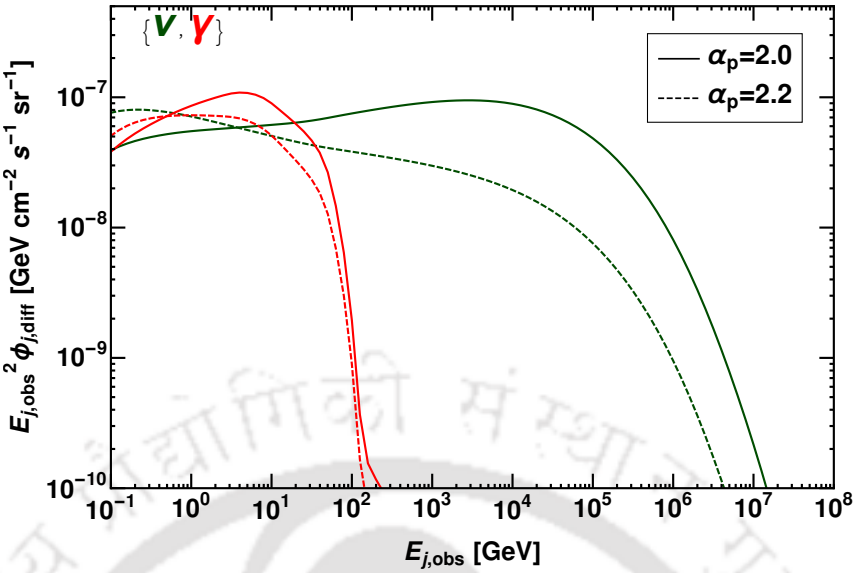

Figure 5.4: Diffuse backgrounds of gamma-rays (in red) and all-flavour neutrinos (dark green) for all YSNe Types as a function of the observed particle energy for $\alpha_{\rm p} = 2.0$ (solid) and $\alpha_{\rm p} = 2.2$ (dashed). The subscript j represents ν and γ. Larger values of $\alpha_{\rm p}$ are responsible for softer energy spectra for both gamma-rays and neutrinos; the dependence of the diffuse spectrum on α_p is more pronounced for neutrinos than for gamma-rays.

observed for gamma-rays (see left panel of Fig. 5.3), the contribution from Type IIn YSNe is larger than the one of Type II-P and Ib/c (LT) YSNe below $E_\nu = 10^7$ GeV. However, Type II-P YSNe also have significant contribution and their flux is smaller than IIn YSNe by about a factor of 2. The diffuse flux of Type Ib/c (LT) is small at lower energies but might show up above $E_\nu = 10^7$ GeV, this is due to the fact that the maximum proton energy of this YSN Type is large because of the larger shock velocity and shock radius (see also Fig. 6.3). Also note that the contribution of Type IIb/II-L YSNe to the total diffuse emission of high-energy neutrinos is negligible as the source flux of Type IIb/II-L YSNe is already quite small in comparison to the one of other Types of YSNe.

5.2.4 Model parameter uncertainties

The injection spectral index of protons crucially affects the high-energy diffuse backgrounds. Fig. 5.4 shows the total diffuse gamma-ray and neutrino backgrounds for $\alpha_{\rm p} = 2.0$ (solid curves)

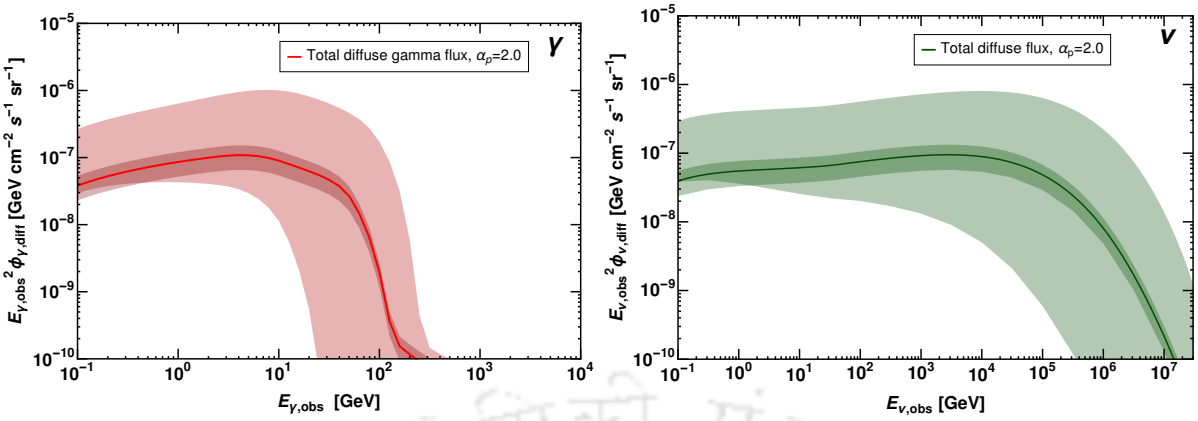

Figure 5.5: *Left panel:* Diffuse gamma-ray background from all Types of YSNe as a function of the observed gamma-ray energy. The solid red line indicated our benchmark diffuse emission for $\alpha_{\mathrm{p}} = 2.0$ and the other model parameters fixed as in Table 3.1. The band correspond to the uncertainties in shock velocity v_{sh}, power law α_{p}, fraction of kinetic energy ε_{p} and fraction of magnetic energy ε_{B} (see Table 5.1). The uncertainty associated to the local SN rate is represented by the thin band. *Right panel:* Correspondent diffuse all-flavour neutrino background. The uncertainty from model parameters is larger than the one from the SN rate.

and $\alpha_{\mathrm{p}} = 2.2$ (dashed curves). Both diffuse backgrounds are larger for $\alpha_{\mathrm{p}} = 2.0$ than that for $\alpha_{\mathrm{p}} = 2.2$. This is due to the hardness of the energy distribution for $\alpha_{\mathrm{p}} = 2.0$ at higher energies. Moreover, for gamma-rays, the EM cascaded flux of $\alpha_{\mathrm{p}} = 2.0$ is larger than that obtained by using $\alpha_{\mathrm{p}} = 2.2$. The dependence on α_{p} is more pronounced for neutrinos than for gamma-rays. This is because the higher energy part (above 100 GeV) of gamma-rays is heavily attenuated.

The left panel of Fig. 5.5 shows the total diffuse background of gamma-rays, including the contribution from all YSN Types. For reference, the diffuse background estimated for benchmark model parameters as in Table 3.1 and $\alpha_{\mathrm{p}} = 2.0$ is represented by the solid red curve. The uncertainty band results from the convolution of the uncertainties on the parameters listed in Table 3.1. In particular, the model parameters mostly affecting the spectral distribution are v_{sh}, ε_{p} and ε_{B}; the upper and lower limits of the parameters are reported in Table 5.1. Our choices on the upper limits for these model parameters are conservative compared to observations (37; 205; 206). The remaining model parameters (see Table 3.1) are instead kept fixed. Note that we have not considered uncertainties on the benchmark parameters of Type IIb/II-L YSNe because their contribution to diffuse backgrounds is negligible. The lower limit of the gamma-ray diffuse emission is instead obtained for $\alpha_{\mathrm{p}} = 2.2$ and shows a softer energy distri-

Table 5.1: Uncertainties on a selection of model parameters of different YSN Types (see Table 3.1 for the benchmark parameters). Uncertainties on the model parameters of Type IIb/II-L and Ib/c YSNe are not included because their contributions to diffuse backgrounds of high-energy particles is negligible.

Parameters	**Type IIn**		**Type II-P**		**Type Ib/c (LT)**	
	Upper	Lower	Upper	Lower	Upper	Lower
v_{sh} (kms^{-1})	9.5×10^3	5×10^3	2×10^4	8×10^3	2×10^4	5×10^3
ε_p	0.1	0.01	0.1	0.01	0.1	0.01
ε_B	10^{-2}	3×10^{-4}	3×10^{-2}	10^{-3}	3×10^{-2}	10^{-2}

bution. In addition, the uncertainty associated to the local SN rate (see Sec. 5.2) might also have important consequences on the diffuse background spectra of gamma-rays and neutrinos. This uncertainty is included in our benchmark diffuse spectra and shown by the thin band. Interestingly, the uncertainty in the diffuse background from the SN rate is smaller than the one from the model parameters. Analogously, the right panel of Fig. 5.5 shows the total diffuse background of high-energy neutrinos.

5.2.5 Discussion

Fig. 5.6 summarizes our findings on the gamma-ray and neutrino diffuse emission from YSNe. For reference, the data points of the Fermi-LAT Isotropic Gamma-ray Background (IGRB) between 100 MeV to 820 GeV are shown (267). Moreover, the unexplained IGRB component in the range 50–1000 GeV is plotted with the purple dashed line (47; 161). We also show the data points with error bars corresponding to 7.5 years by IceCube High-Energy Starting Event (HESE). The best fit to the IceCube data is represented by the black-dashed line; the related 68% confidence level uncertainty is plotted in cyan (48). The diffuse neutrino flux sensitivity at 68% confidence level for KM3NeT is shown in light blue (284).

As for gamma-rays, a large fraction of the IGRB observed by Fermi-LAT may be coming from blazars, although recent work shows evidence for star-forming galaxies as the dominant contributors to the IGRB (166; 285; 286; 287; 160). Our findings are in agreement with this

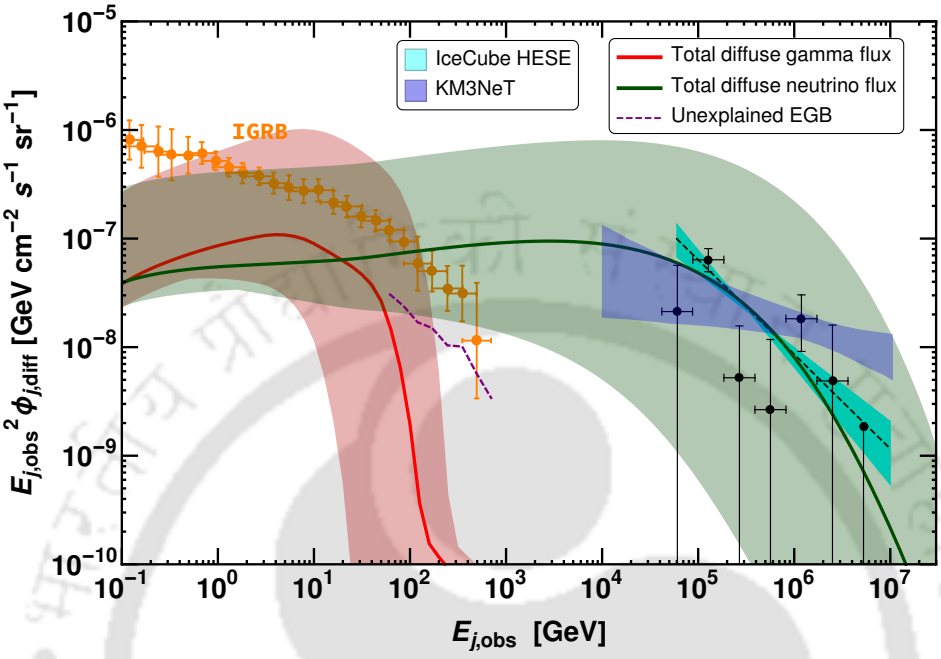

Figure 5.6: Total diffuse gamma-ray (in red) and all-flavour neutrino (in green) backgrounds from YSNe as functions of the observed particle energy, analogous to Fig. 5.5. The subscript j stands for ν or γ. For gamma-rays, the orange data points with error bars illustrate the diffuse gamma-ray background measured by Fermi-LAT (IGRB) (267). The purple dashed curve shows the unexplained portion of the IGRB (77; 47; 104). For neutrinos, the black-dashed line shows the IceCube (HESE) diffuse flux best fit for 7.5 years of data (black data points with error bars); the cyan band depicts the uncertainty on the IceCube diffuse flux at 68% confidence level (48). The diffuse flux sensitivity of the future neutrino experiment KM3NeT is also shown by the light blue band (284). It is evident that part of the parameter space considered for YSNe is ruled out from multi-messenger constraints from Fermi-LAT and IceCube. Nevertheless, our benchmark YSN parameters (Table 3.1) can very well explain part of the IceCube diffuse flux without the correspondent gamma-ray emission being in tension with the Fermi-LAT gamma-ray data. KM3NeT will further probe the diffuse neutrino flux from YSNe in the energy range 10^4-10^6 GeV.

picture on the IGRB composition. In fact, our benchmark YSN gamma-ray background (red solid line) is severely attenuated above 100 GeV and not in tension with blazar unexplained flux (purple dashed line). Moreover, the gamma-ray diffuse emission from star-forming galaxies should originate from the collisions of the SN accelerated protons with molecular clouds (ISM) in these active galaxies (274; 288) and therefore include the contribution of YSNe as well. However, the gamma-rays created in YSNe undergo larger attenuation (due to the dense CSM environment) than gamma-rays created in a thin ISM (160). By comparing the diffuse gamma-ray emission predicted in this work with the Fermi-LAT data in Fig. 5.5, it is evident that our benchmark diffuse gamma flux is smaller than the Fermi-LAT IGRB and thus might negligibly contribute to the total SBG flux.

As for high-energy neutrinos, our benchmark YSN neutrino background is in good agreement with the IceCube HESE data below 10^6 GeV. Intriguingly, the YSN neutrino background at low energies (10^4–10^5 GeV) is significantly large and can explain the HESE concentration at these energies, in alternative to dark sources or hypernovae (270; 271; 272; 273; 274). Within the YSN interpration, the low-energy component of the neutrino diffuse background may originate from Type IIn SNe, whereas the neutrino diffuse background above 10^5 GeV may also have contributions from II-P and Ib/c (LT) SNe. This multi component interpretation, in addition to likely contributions to the neutrino diffuse emission from other sources, can accommodate possible different power laws in different energy ranges in future data fits of IceCube data (48). The KM3NeT sensitivity shows that it will be able to probe the diffuse flux of neutrinos from YSNe in the energy range 10^4–10^6 GeV.

The contribution of YSNe may be subleading (e.g. for our benchmark model parameters) to the IGRB, however it could explain very well the observed IceCube diffuse emission below 10^6 GeV, relaxing the tension between gamma-ray and neutrino data for hadronic sources invoked as motivation for "hidden" sources (270). Interestingly, part of the YSN parameter space allowed by multi-wavelength electromagnetic observations (see Table 5.1) may overshoot the Fermi-LAT and IceCube data, as shown by the bands in Fig. 5.6. This suggests that YSNe with such extreme model parameters are not representative of the YSN population.

The green and red solid curves in Fig. 5.6 have been obtained for $\varepsilon_p = 0.01$ for Type IIn SNe. The maximum value allowed by the IGRB data is $\varepsilon_p \simeq 0.03$, for which the corresponding neutrino background is enhanced by a factor of 3. Kinetic simulations predict ε_p as large as

0.2 (173), which may be in conflict with the high-energy diffuse backgrounds, if representative of the whole Type IIn YSN population.

The diffuse neutrino flux from Type IIn SNe reported in Ref. (36) relies on $\varepsilon_p \sim 0.2$, which may be in tension with the Fermi-LAT IGRB. On the other hand, the Monte-Carlo simulations of Ref. (36) for randomly distributed ε_p in the range $[0.01, 0.1]$ produced a smaller diffuse flux, contributing up to 10% to the IceCube HESE flux. We find that the IceCube HESE data can be accommodated by smaller values of ε_p, thus remaining consistent with the IGRB data. In our case, the smaller ε_p is allowed as the total diffuse background also includes non-negligible contributions from Type IIP and Ib/c (LT) YSNe. In particular, Ib/c (LT) YSNe having the harder spectra dominate the higher energy tail above 1 PeV.

Our findings are also in agreement with the ones of Ref. (289), which estimated the neutrino and gamma-ray emission from a range of non-relativistic shock powered transients, concluding that the observed neutrino emission may come from gamma-ray dim sources. However, their model is based on optical observations of these transients, while we relied on YSN model parameters coming from a wide range of multi-wavelength surveys.

Upper limits on the high-energy diffuse neutrino background from SNe have been provided in Refs. (242; 290), which found that the diffuse neutrino background is dominated by SNe II-P, followed by SNe IIn and Ib/c. These findings are in contrast with ours because of the different choices of the local SN rates (Ref. (242) assumes $\xi = 52.4\%$ for SNe II-P, 6.4% for SNe IIn, and 25% for SNe Ib/c, while we considered the YSN fractions summarized in Fig. 5.1). In addition, Refs. (242; 290) do not take into account gamma-ray constraints.

We note that the larger mass loss rates of SNe II-P reported in Refs. (199; 198) (see also Sec. 3.3) can produce a diffuse emission from YSN II-P comparable to that of Type IIn SNe. This, in turn, may further constrain the parameters characteristics of the SN IIn population.

5.3 Conclusions

In this chapter, we have computed the diffuse backgrounds of gamma-rays and high energy neutrinos produced by YSNe as a result of interaction of SN ejecta with dense CSM. Despite intense

research activity, the origin of the bulk of the diffuse high-energy neutrino background observed by the IceCube Neutrino Observatory as well as the the Isotropic Gamma-Ray Background detected by Fermi-LAT is yet unknown. Our benchmark (intermediate) diffuse neutrino emission from YSNe is in excellent agreement with the IceCube HESE data and suggests that YSNe could constitute the bulk of the high-energy diffuse neutrino emission observed by IceCube below 10^6 GeV, while being dim enough in gamma-rays to avoid any conflict with Fermi-LAT data.

The largest contribution to the diffuse neutrino emission mainly comes from Type IIn YSNe, followed by II-P and Ib/c (LT) YSNe, with Type IIn YSNe dominating the overall neutrino diffuse emission up to 10^7 GeV. Type Ib/c (LT) YSNe populate the diffuse neutrino emission above 10^7 GeV. The Type II-P YSN contribution is also significant, but smaller than the Type IIn SN one. Similar findings also hold for the diffuse gamma-ray background, after including all attenuation effects taking place both in the source and en route to Earth.

Intriguingly, the uncertainty bands obtained for the diffuse high-energy backgrounds by taking into account the uncertainties on the shock velocity, injection spectral index of protons, the kinetic and magnetic energy fractions, and the YSN rate suggest that a large fraction of the YSN parameter space inferred from multi-wavelength electromagnetic observations of YSNe is excluded by Fermi-LAT and IceCube HESE data.

To conclude, the high-energy neutrino emission (especially coming from Type IIn, II-P and Ib/c (LT) SNe) can be a strong contender to explain the low-energy IceCube HESE dataset. The corresponding diffuse gamma ray emission is not in tension with the IGRB data from Fermi-LAT as YSNe gamma-rays are heavily attenuated and effectively "hidden." The detection of high-energy particles from young supernovae will provide new insights on the processes linked to particle acceleration in young SNe.

This page was intentionally left blank.

Chapter 6

Ultra-high energy cosmic rays: production and propagation of GZK fluxes

In this chapter, we discuss the production and propagation of GZK secondaries such as GZK protons, GZK photons and GZK neutrinos which are created by the interaction ultra-high energy cosmic rays with the cosmic microwave background. We also discuss the dependence of these secondary fluxes on various UHECR source properties.

6.1 The GZK process

Soon after the discovery of the cosmic microwave background (CMB), Greisen (8), Zatsepin and Kuzmin (9) (GZK) in 1966 suggested that the UHECR protons can interact with CMB photons via $\Delta^\star$ resonance ($E_{th} \sim 4 \times 10^{19}$ eV) and get attenuated if they originate in sources more distant than 10 Mpc.

The GZK interaction ($p + \gamma_{CMB}$) yields charged pions ($\pi^{\pm}$) and neutral pions (π^0) that subsequently decay to produce high energy neutrinos (GZK or cosmogenic neutrinos) and gamma

rays (GZK photons) as secondaries. However, the UHECR spectrum extending well beyond the GZK cut-off (the trans-GZK UHECRs) opens up new window to our understanding about the origin and propagation of these UHECRs (5; 6; 7; 291). One possible reason for this could be attributed to the piling up of UHECR protons around the GZK cut-off due to energy losses (see 292, for details). In order to resolve this puzzle, one needs to probe the sources and production mechanism of these UHECRs. Concerning the production of these UHECRs, there are two broad classes of models : bottom-up and top-down. In the bottom-up model, the initial UHECRs at the source can be produced by accelerating low energy particles. Charged particles, such as protons and electrons can be efficiently accelerated to extreme energies (around 10^{20} eV) via Fermi's diffusive shock acceleration mechanism (1). The acceleration depends on the size of the acceleration region, forward shock speed and the magnetic field strength (1). Thus, for production of UHE particles, one needs large sources with fast shock and strong magnetic fields. Possible sources of UHECRs include Active Galactic Nuclei (AGN) such as blazars or quasars, radio galaxies, pulsars and Gamma-ray bursts (GRB). Recent detection of a PeV neutrino event by IceCube neutrino observatory from the direction of the blazar TXS 0506+056 provides us with an indirect evidence of particle acceleration to very high energies (21). UHECRs detected by various cosmic ray experiments such as Akeno Giant Air Shower Array (AGASA), High Resolution Fly's Eye (HiRes), Pierre Auger Observatory (Auger) and Telescope Array support the idea that UHECRs could emanate from these sources. Note that shock waves produced in supernova explosion could also produce high energy protons upto a few $\mathcal{O}(10$ PeV) (45; 154; 257; 35; 36). In contrast to the bottom-up model, the top-down model leads to the production of UHECRs via exotic sources (293) such as decay of heavy dark matter particles (294; 3; 295; 296; 50; 297), topological defects, cosmic strings etc (see Ref. 3, for details). The generic prediction of this class of models is that photons should dominate over nucleons but this is not supported by Auger data (52). Thus, the top-down models are currently disfavoured. In what follows, we shall consider the bottom-up model i.e., shock accelerated origin of UHECRs.

In addition to directly probing the UHECR primaries, we can also probe the secondaries such as cosmogenic or GZK neutrinos and GZK photons which are expected to be produced in the GZK process (298; 299; 300; 301; 302; 303; 304). With the advancement in detection prospects of high energy neutrinos and gamma rays, the possibility of probing the origin of UHECRs (trans-GZK) via multi-messenger approach opens up.

The GZK neutrinos, being weakly interacting, are not impacted by the propagation effects and can reveal useful information about the source spectrum of the UHECR primaries. On the other hand, the GZK photons are expected to suffer attenuation due to pair production loss on the CMB and the extra-galactic radio background (ERB). Apart from the pair production loss, other propagation effects like inverse Comptonisation of these background photons can also affect the GZK photon flux. The attenuation of GZK photon flux by the CMB is well-estimated as the CMB spectrum is well-described by a thermal distribution (305) However, the attenuation of GZK photons by the ERB is not very well-estimated, primarily because models describing the ERB spectrum have large uncertainties. (306; 307). These model uncertainties can cascade to the GZK photon flux prediction and can give rise to the substantial uncertainties (10; 65; 308). Apart from these uncertainties, the ARCADE2 experiment (309) has detected an excess ERB at GHz frequencies and can influence the prediction of the GZK photon flux.

In the following, we discuss the properties of the primary UHECR spectrum and the subsequent production of GZK secondaries: protons, photons and neutrinos. We also discuss the propagation of these secondaries and their dependence on the primary UHECR properties.

6.2 GZK flux: Production and Propagation effects

UHECRs upto 10^{20} eV have been detected by CR observatories (5; 6; 7). These UHECRs are believed to be produced in high energy astrophysical environments through the mechanism of diffusive shock acceleration (1). The diffusive shock acceleration results in a power law distribution of CRs with a cut-off at higher energies related to the maximum CR energy (3). This power law behaviour is also well-motivated from the CR observations (5; 6). Thus, we can model the primary UHECR proton spectrum to be a power law with an exponential cut-off (310),

$$J_{\rm p}(E_{\rm p}) = \frac{{\rm d}N_{\rm p}(E_{\rm p})}{{\rm d}E_{\rm p}} \propto \begin{cases} \left(\frac{E_{\rm p}}{E_{\rm p,min}}\right)^{-\alpha}, & E_{\rm p} \leq E_{\rm cut} \\ \left(\frac{E_{\rm p}}{E_{\rm p,min}}\right)^{-\alpha} \exp\left(1 - \frac{E_{\rm p}}{E_{\rm cut}}\right), & E_{\rm p} > E_{\rm cut}\ , \end{cases} \tag{6.1}$$

where, $E_{\rm p,min}$ is the minimum energy of the UHECR protons and α is the power-law index. The spectrum falls rapidly for energies larger than the cut-off energy, $E_{\rm cut}$. The standard diffusive shock acceleration theory predicts α to be around 2 (1; 311). However, complex nature of shock acceleration, magnetic field amplification and effect of cosmic ray pressure can lead to deviations from 2 (312; 313). Both $\alpha < 2$ and $\alpha > 2$ have been indicated by secondary high energy particles considered to be originated from parent CRs. For example, Galactic PeV gamma-ray observations ($\alpha < 2$) (22; 28; 154), the diffuse neutrino background at IceCube ($\alpha > 2$) (314), and the diffuse CR spectra ($\alpha \neq 2$) (315; 5). The underlying acceleration mechanism determines the power law and changes from object to object. Our focus is on the UHE part of the CR spectra. At these energies, the UHECR observations suggest α to be larger than 2 and in the range, $[2.0-2.7]$. Note that the spectral index at source might differ from the observed spectral index as CR interaction within source as well as during propagation could influence the spectral index (79). Therefore, we assume α in the range $[2.0-2.7]$ for our analysis. The other source parameter, $E_{\rm cut}$ also depends on the source environment and the confinement duration of CRs in the source environment. These CRs escaping the confinement zone due to dynamical and/or advective and/or diffusion losses can make the acceleration at very high energies inefficient (3; 1). Thus, the CR spectrum is expected to fall rapidly at very high energies resulting in a cut-off energy $E_{\rm cut} \sim \mathcal{O}(10^{20})$ eV (10; 3). Note that, the Eq. 6.1 is not normalised. The normalization is fixed from the cosmic ray data above 10^{17} eV (5; 6; 7), thus fixing the minimum proton energy, $E_{\rm p,min} = 10^{17}$ eV.

Fig. 6.1 shows the dependence of the primary UHECR spectrum (in arbitrary units (a.u.)) of a point source on the different model parameters. The left panel shows CR spectra for three values of the spectral index, $\alpha = 2.0,\ 2.4,\ 2.7$ with a fixed cut-off energy, $E_{\rm cut} = 10^{22}$ eV, while the right panel displays CR spectra for different cut-off energies, $E_{\rm cut} = 10^{20},\ 10^{21},\ 10^{22}$ eV with $\alpha = 2.0$. It is clear that smaller spectral index produces harder spectra. As discussed above, the cut-off energy plays an important role in determining the spectral shape at very high energies, evident in our model spectra. The spectra in the right panel shows that the CR spectrum falls rapidly for energies $E_{\rm p} > E_{\rm cut}$.

Based on this primay UHECR spectra modelling, one may estimate the CR and secondary fluxes and compare with observational limits. As mentioned above, secondary particles such as photons and neutrinos are produced as a result of interaction of UHECR above a certain

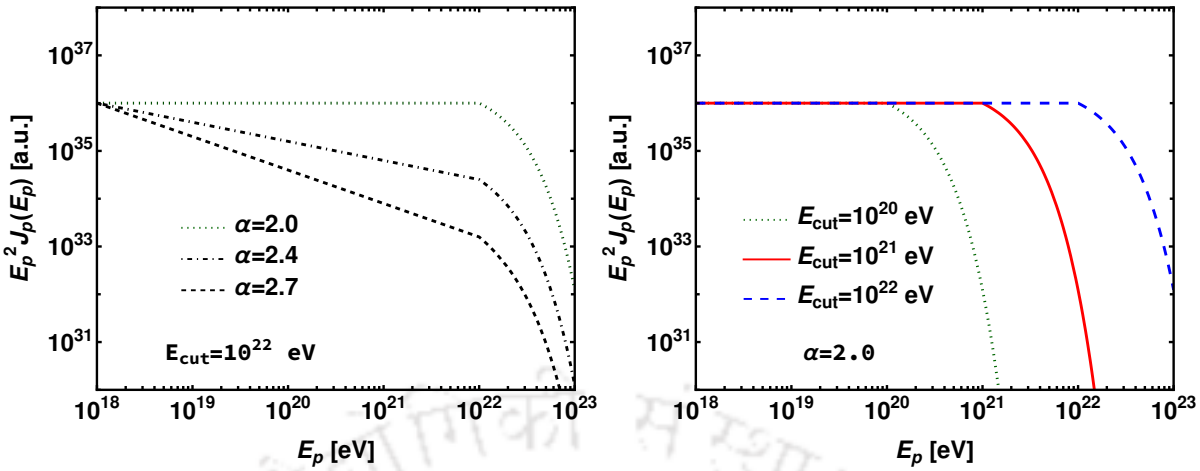

Figure 6.1: UHECR proton spectra at the source for different values of power law index, α and cut-off energy, $E_{\rm cut}$. The left panel shows the UHECR spectra for three different power laws, $\alpha = 2.0$ (green dotted), $\alpha = 2.4$ (black dot-dashed) and $\alpha = 2.7$ (black dashed) with fixed cut-off energy $E_{\rm cut}$. Effect of variation in $E_{\rm cut}$ on the UHECR spectrum for fixed power law index, $\alpha = 2.0$ is shown in the right panel by choosing the $E_{\rm cut}$ as 10^{20} eV (green dotted), 10^{21} eV (red solid) and 10^{22} eV (blue dashed). The cut-off energy ensures the UHECR spectrum falls rapidly above $E_{\rm cut}$.

threshold energy with the CMB photons. We next describe the GZK process and the production of secondaries. We also discuss the reach of upcoming UHE neutrino and photon detectors.

6.2.1 The GZK effect and secondary production

Greisen, Zatsepin and Kuzmin (8; 9) proposed that the UHECR spectrum beyond $E_{th} \simeq 4 \times 10^{19}$ eV should be suppressed due to the interaction of CR particles (protons or nuclei) with the low energy photons of the CMB primarily due to the $\Delta^\star$ resonance. For protons, the pion photoproduction produces neutral or charged pions,

$$p + \gamma_{\rm CMB} \quad \rightarrow \quad \Delta^\star \quad \rightarrow N + \pi^{\pm}(\pi^0) \tag{6.2}$$

The pions produced in the GZK process (Eq. 6.2) decay to give rise to secondaries (49) which include electrons, neutrinos and photons. The charged secondaries (electrons, positrons) from

GZK process can not reach Earth due to interaction with inter-galactic magnetic field and ambient matter (10). The neutral pions decay to produce “GZK photons" and charged pions decay to produce “GZK or cosmogenic neutrinos",

$$\begin{aligned} \pi^0 &\rightarrow \gamma + \gamma \\ \pi^{\pm} &\rightarrow \mu^{\pm} + \bar{\nu}_{\mu}(\nu_{\mu}) \\ &\hookrightarrow e^{\pm} + \nu_e(\bar{\nu}_e) + \bar{\nu}_{\mu}(\nu_{\mu}) \ . \end{aligned} \tag{6.3}$$

The CMB spectrum follows a blackbody distribution with a mean temperature of 2.7 K and peaks at around 4×10^{-4} eV. Using this, we can estimate the cut-off energy of the protons to be $\sim 4 \times 10^{20}$ eV. This is referred to as the GZK cut-off. The UHECR protons observed above the GZK cut-off are termed as “GZK protons". While the charged secondaries get deflected and can not reach Earth, the neutral ones, GZK photons and GZK neutrinos have promising detection prospects.

The GZK photons and GZK neutrinos propagate through the intergalactic space filled with low energy photon backgrounds, i.e., CMB and ERB. These backgrounds are crucial for the propagation of GZK photons as they can take part in interactions such as pair production and inverse Compton. In order to estimate the impact of CMB and ERB on the propagation of GZK photons, one needs a proper estimate of the background photons (ERB and CMB). While the CMB is well-described by a blackbody spectrum (316) as mentioned above, understanding of ERB is not at the same level. The models describing the ERB spectrum, in general, have large uncertainities and therefore the attenuation of GZK photons by the ERB is not very well-estimated. In the following, we shall adopt a model of ERB to demonstrate the impact of ERB on GZK photon propagation (306). It should be noted that the GZK neutrinos do not suffer propagation losses, owing to their weakly interacting nature.

6.2.2 Extra-galactic radio background and secondary propagation

The ERB comprises of radio photons of KHz-GHz frequencies emitted by radio galaxies and star forming galaxies (306; 307; 317). These radio photons are produced through free-free

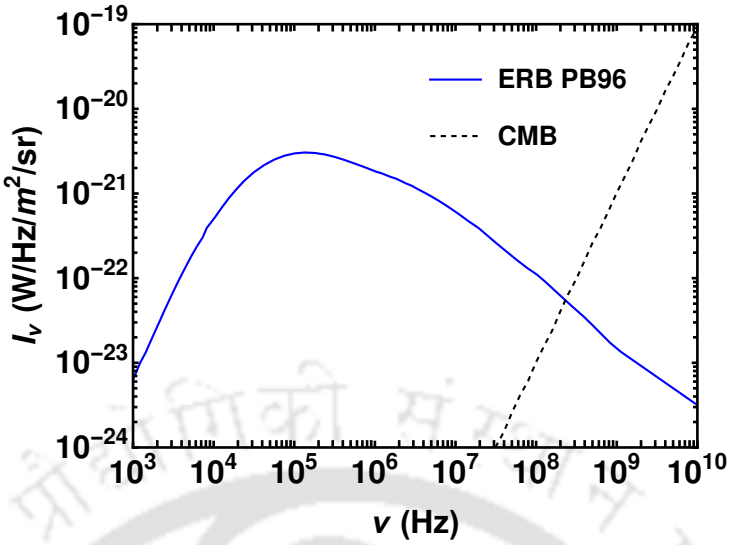

Figure 6.2: The figure shows the intensity (I_ν) of ERB photons as a function of frequency (ν) for the Protheroe and Biermann model (306). The black-dashed line shows the CMB intensity for comparison.

emission of thermal electrons and synchrotron radiation of high energy electrons (307). At high frequencies (GHz), the ERB is dominated by the radio galaxies, whereas at low frequencies (below MHz), the contributions from star forming galaxies are more pronounced. Both radio and star forming galaxies contribute almost equally to the ERB in the intermediate frequencies, i.e., MHz-GHz. The intensity of this ERB can be estimated by using observed luminosity functions of star forming and radio galaxies (306; 307). This estimation also requires radio emission of individual galaxy which can be obtained by modeling the thermal and non-thermal electron densities of the galaxy. Two models of ERB are available in the literature, namely the Protheroe and Biermann (PB96) and Nitu et. al. (Nitu21) (306; 307). These models shall be discussed in detail in Sec. 7.1. Fig. 6.2 shows the lower estimate of ERB PB96 (306). This shows that the ERB peaks at around 100 KHz frequency and then falls rapidly. Note that various sources of uncertainty such as luminosity function and electron density impact the ERB estimate. Also, the predictions of the two ERB models (306; 307) have substantial difference. To demonstrate the role of ERB on GZK photon propagation, we choose the conservative estimate of ERB from the literature as shown in Fig. 6.2 (306). We also show the CMB intensity in Fig. 6.2 for comparison. In Sec. 7.1, we provide a detailed discussion on the different ERB models, their associated uncertainties and the effect of these on the GZK photon flux propagation.

Now with the above ERB model, one can estimate the GZK photon flux at Earth for sources of interest, i.e., point or diffuse. Note that we focus on diffuse flux prediction in this study. The estimation also depends on the properties of primay UHECRs producing these GZK photons along with GZK neutrinos through the GZK process. In the following, we discuss the methodology adopted for the estimation of GZK particles, i.e., protons, photons and neutrinos.

6.3 GZK flux: Estimation

Detection of GZK photon and neutrino flux produced in photo-hadronic interaction in point sources may reveal properties of the source and the propagation characteristics (49). Estimating the GZK photon flux at Earth includes various propagation effects like pair production, subsequent cascading and inverse Compton on different photon backgrounds like CMB, ERB and Extra-galactic Background Light (EBL) (10). The effects of EBL dominate at lower energies around 100 TeV. Hence, we will not discuss the EBL effects in the subsequent sections. Contrary to the GZK photons, the GZK neutrinos come un-attenuated due to their weakly interacting nature. In this work, we focus on the diffuse background of GZK photons and neutrinos coming from a large number of sources distributed across the Universe. An estimate of these diffuse fluxes after incorporating propagation details is complicated and time-consuming. We employ the public Monte-Carlo simulation code CRPropa 3.2, (310; 318) to estimate the diffuse GZK photon and neutrino flux. CRPropa 3.2 is primarily written in C++ interfaced to Python. CRPropa 3.2 contains different modules for the aforementioned propagation effects that allow the evaluation of these processes independently. The code also allows distributing sources across a large length scale (upto Gpc) to compute the diffuse spectra of UHECR.

In order to demonstrate the GZK proton and secondary production, we compute the fluxes of GZK protons, photons and neutrinos for a point source at 50 Mpc using 1D simulation in CRPropa 3.2. The point source fluxes are plotted in arbitrary units in the left panel of Fig. 6.3. The source proton spectrum is described by Eq. 6.1 with the parameters $\alpha = 2.0$ and $E_{\rm cut} = 10^{22}$ eV, shown as dashed black line in the left panel of Fig. 6.3. The interaction of these protons with CMB photons creates the resultant GZK protons (black solid curve). The sudden attenuation of the GZK proton flux above $\sim 10^{20}$ eV is due to the GZK effect. Among the GZK secondaries,

the GZK photons will suffer attenuation due to their interaction with the CMB and ERB. The secondary GZK photon flux without these propagation losses is shown by the red dotted curve in the left panel of Fig. 6.3. To understand the propagation effect on the GZK photons, we first study the attenuation on the CMB and then add the ERB effect. The red dashed curve in the left panel of Fig. 6.3 shows the sole effects of CMB on the GZK photon flux. The relevant interactions for CMB are pair production and Inverse Compton. The ERB also impacts the GZK photon flux and is dominated by pair production loss on ERB at energies above 10^{19} eV (10). The attenuation would be minimum for the lower estimates of ERB. Therefore, we consider the lower estimate of PB96 ERB model for conservative prediction of the GZK photon flux. The resultant GZK photon flux including attenuation on ERB is shown by the red solid curve in the left panel of Fig. 6.3. This flux shows that the effect of the ERB is significant at energies above 10^{19} eV. On the other hand, the GZK neutrino flux remains unaffected by these backgrounds and only undergo flavour equalisation $(1:1:1)$ during propagation (319). The GZK neutrino flux (single flavour) is shown by the blue curve in the left panel of Fig. 6.3.

We now compute the diffuse flux of GZK protons, photons and neutrinos. The individual source proton spectrum is described by Eq. 6.1, and we choose the benchmark parameter values as $E_{\rm cut} = 10^{22}$ eV and $\alpha = 2.0$. The sources are assumed to be distributed in the range of 0.1 Mpc to 10 Gpc. The simulation results in the diffuse flux of GZK protons at Earth and depends on the normalization of the individual source proton spectra. This is taken care by normalizing the GZK proton flux with the observed CR data (6; 5; 7).

The right panel of Fig. 6.3 shows the diffuse fluxes of primary UHECR proton, GZK protons, GZK photons (with and without propagation effects) and GZK neutrinos as a function of energy. The source spectra appear as a horizontal flat line (black dashed) as the spectral index is $\alpha = 2.0$. These protons undergo attenuation due to the GZK effect. The resultant GZK protons at Earth are shown by the black curve. The GZK proton flux is normalized to the observed cosmic ray data at energy black 4×10^{19} eV (6; 5; 7). The magenta data points show the Auger data (5), whereas the gray data points represent the HiRes data (6). The corresponding secondaries have also been scaled with this normalization to obtain the GZK photons (red curve) and GZK neutrinos (blue curve) at Earth.

The diffuse flux of GZK photons without any propagation effects is shown by the dotted red curve in the right panel of Fig. 6.3. The diffuse photon flux undergoes substantial losses on

CMB and ERB. Out of these photon backgrounds, while CMB is known precisely, the present ERB estimates have a large uncertainty (306; 307). The uncertainty in ERB can significantly affect the prediction of GZK photons, especially at the ultra-high energies ($> 10^{19}$ eV) as shown in the case of point source above. The attenuation of the GZK photon flux due to CMB is shown by the red dashed curve in the right panel of Fig. 6.3. The resulting diffuse GZK photon flux after interaction with ERB is shown by the red solid curve in the right panel of Fig. 6.3. Clearly, the effect of ERB becomes important above energies 10^{19} eV as in the point source case.

So far we have discussed the impact of background photons (CMB and ERB) on the GZK primary and secondaries. We next discuss the dependence of the fluxes of GZK protons, GZK photons and GZK neutrinos on the different source properties. We also study the effect of different ERB models on the GZK photon flux.

6.4 GZK flux: Dependence on source properties

The properties of the primary UHECRs at the source impact the estimation of the secondary GZK photon and GZK neutrino fluxes at Earth. These properties depend on the acceleration mechanism producing these UHE particles. The primary UHECR proton spectra described by Eq. 6.1 depend on various parameters like spectral index, α and the cut-off energy, $E_{\rm cut}$. These parameters depend on the acceleration mechanism at the source. In addition, the estimation of these fluxes depends on the distribution of these sources. The attenuation of the GZK photon flux depends on the propagation length. The UHECR sources are modelled to be distributed over the space in the region $d_{\rm min} \leq d \leq d_{\rm max}$, where $d_{\rm min}$ and $d_{\rm max}$ are the minimum and maximum distances to the source. Since, the likely sources of UHECRs are extra-galactic, we choose to vary $d_{\rm min}$ in the range $[0.1, 100]$ Mpc. On the other hand, we fix $d_{\rm max}$ to be 10 Gpc which corresponds to a redshift of 1.4. Further, for the propagation of GZK photons, the choice of ERB model is crucial and we choose ERB PB96 for our analysis (306).

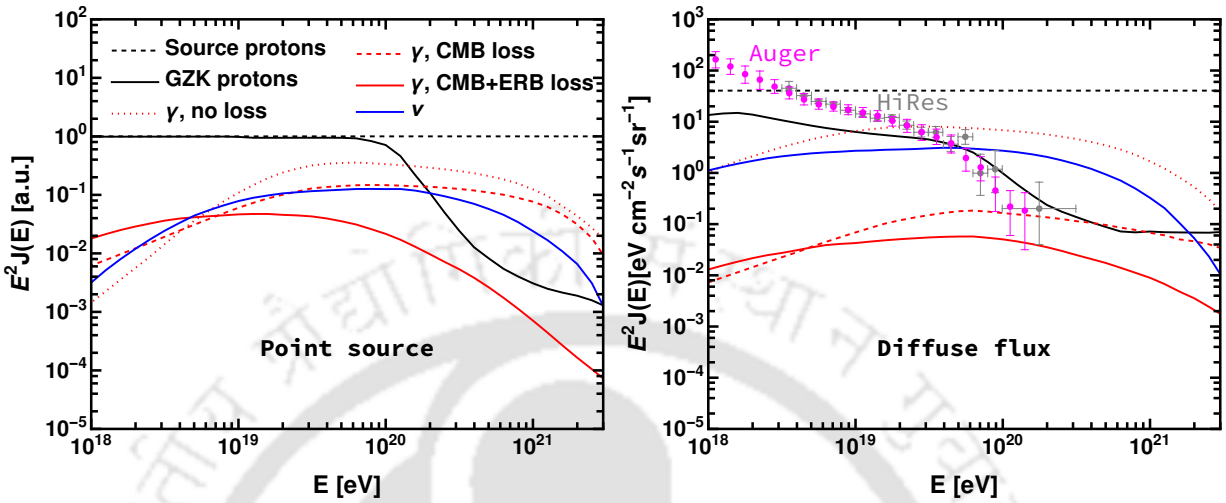

Figure 6.3: *Left:* Fluxes of GZK protons (black solid), GZK photons (red) and GZK neutrinos (blue, single flavour) for a point source at 50 Mpc. The primary UHECR spectrum (black dashed) parameters are, $\alpha = 2.0$, $E_{\rm cut} = 10^{22}$ eV. The red dotted and blue curves show the gamma-rays and neutrinos (single flavour) without propagation effects respectively. The gamma-rays after interaction with CMB is shown by the red dashed curves, whereas the red solid curve shows the effects of both CMB and ERB. The neutrinos do not suffere any losses. *Right:* Diffuse fluxes of GZK protons, GZK photons and GZK neutrinos produced by interaction of UHECR protons with CMB photons. The parameters are chosen as $\alpha = 2.0$, $E_{\rm cut} = 10^{22}$ eV and $d_{\rm min} = 0.1$ Mpc. The black dashed line represents the primay UHECR proton spectrum. The sources are assumed to be distributed between 0.1 Mpc to 10 Gpc. The black solid curve shows the diffuse GZK proton flux and normalised with the observed cosmic ray data by Auger (magenta data points) (5) and HiRes (gray data points) (6). The corresponding GZK photon and GZK neutrino (single flavour) fluxes (without propagation effects) produced in photo-hadronic interaction are shown by the red dotted and blue curves respectively. The red dashed and red solid curves correspond to propgation loss on CMB and CMB with ERB respectively. Both the panels show that the effect of CMB on GZK photons is more pronounced at lower energies, whereas the effect of ERB is crucial at higher energies.

6.4.1 Dependence on the spectral index (α)

The spectral index (α) is crucial to estimate the UHECR flux at highest energies and is predicted to be about $\alpha = 2$ (1) from the diffusive shock acceleration theory. However, several indirect galactic and extra-galactic evidences suggest substantial deviation from this standard theory (312; 313; 315). The observed CR spectrum in fact hints at power law index of about 2.7 (315). Due to the existence of the knee and ankle, the observed CR spectrum may also incorporate multiple spectral indices (1; 65; 320). Therefore, we vary α in the range $[2.0, 2.7]$ to illustrate the effect of α on the fluxes of GZK protons, GZK photons and GZK neutrinos.

Fig. 6.4 shows the fluxes of GZK protons (left panel), GZK photons (red curves in right panel) and GZK neutrinos (blue curves in right panel) for three different values of α. The dotted curves correspond to $\alpha = 2.7$, the solid curves represent $\alpha = 2.0$ and the dashed curves show the fluxes for $\alpha = 2.4$. The other parameters are kept fixed, $E_{\rm cut} = 10^{22}$ eV and $d_{\rm min} = 0.1$ Mpc. We also depict the observed CR data by HiRes and Auger (6; 5) for comparison. Clearly, smaller spectral index produces harder spectra. For $\alpha = 2.4$ and $\alpha = 2.7$, the GZK proton spectrum produces a good fit to the HiRes and Auger data. However, $\alpha = 2.0$ doesn't yield a reasonable fit to the data. This shows that different values of α are possible for the primary UHECR spectrum. The variation of α also results in significantly different secondary fluxes. The dependence of GZK photon and GZK neutrino flux on α is shown in the right panel of Fig. 6.4. As expected, the fluxes of GZK neutrinos are much larger than GZK photons. The difference due to variation of α is more prominent at higher energies. Thus, detection of the associated GZK photons and GZK neutrinos can indirectly allow us to probe the spectral index.

The harder spectra corresponding to lower values of α ($\lesssim 2$) find can not explain the observed UHECR data. For the rest of the discussion, we focus on $\alpha > 2$ as the diffuse CR flux observations above 10^{17} eV point towards softer fluxes at the highest energies, i.e., $\alpha \sim 2.5 - 2.7$ (5; 6; 7). In order to probe the effect of spectral index variation, we shall consider α in the range between 2.2 and 2.7.

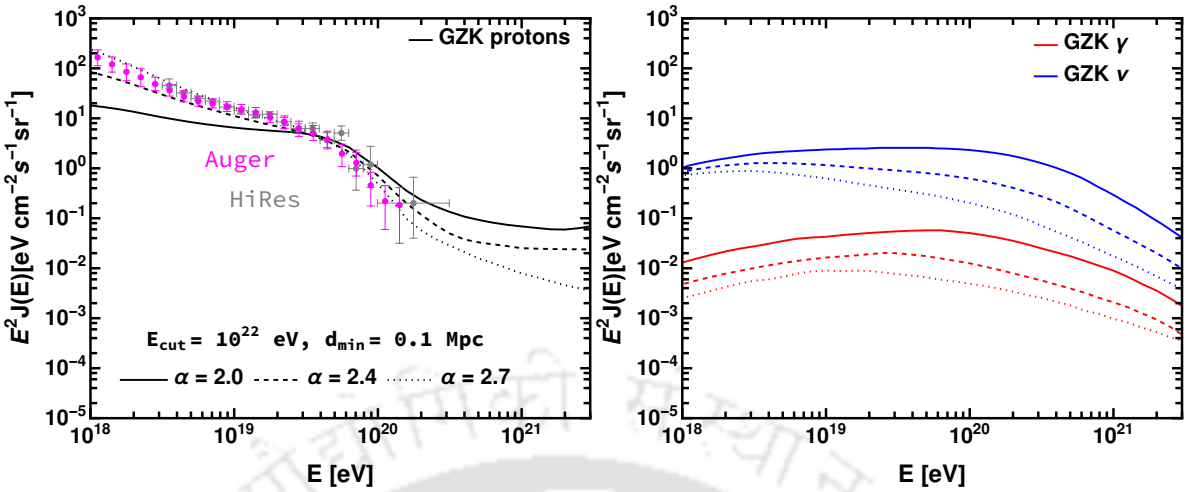

Figure 6.4: Diffuse fluxes of GZK protons, GZK photons and GZK neutrinos (single flavour) for different power law indices, i.e., $\alpha = 2.0$ (solid), $\alpha = 2.4$ (dashed) and $\alpha = 2.7$ (dotted). The remaining parameters are kept fixed as $E_{\rm cut} = 10^{22}$ eV and $d_{\rm min} = 0.1$ Mpc. The left panel shows the GZK protons fluxes for different α normalised to Auger and HiRes data. The corresponding normalised GZK photon flux (red curves) and the GZK neutrino flux (blue curves) are shown in the right panel. These plots show that smaller α produces harder fluxes at high energies.

6.4.2 Dependence on the composition of UHECR

So far, the UHECR primary is taken to be proton. The recent data by Auger (321; 5) suggests that the UHECR could be composed of heavy elements but the fractional component of these heavy elements is still debatable (65; 322; 323). The presence of heavy elements along with protons would lead to lowering of the fluxes of GZK neutrinos and GZK photons (324; 325; 326). In order to illustrate the impact of heavy elements in the UHECR primary, we consider a hypothetical scenario where the UHECR is composed of 100 % iron nuclei. Fig. 6.5 describes the effect of heavy nuclei on the GZK proton flux, GZK photon flux and GZK neutrino flux at Earth. In the left panel of Fig. 6.5, we show a comparison of the two constituents (protons and iron) at the source. The pure proton UHECR spectra is shown as black solid line and pure iron UHECR spectra is shown as black dashed line in the left panel. In the right panel, we show the secondary spectra of GZK neutrinos (blue solid line) and GZK photons (red solid line). We note that GZK neutrinos and GZK photons are an order of magnitude smaller than the corresponding flux for pure proton case. In turn, this would impact the detection prospects of

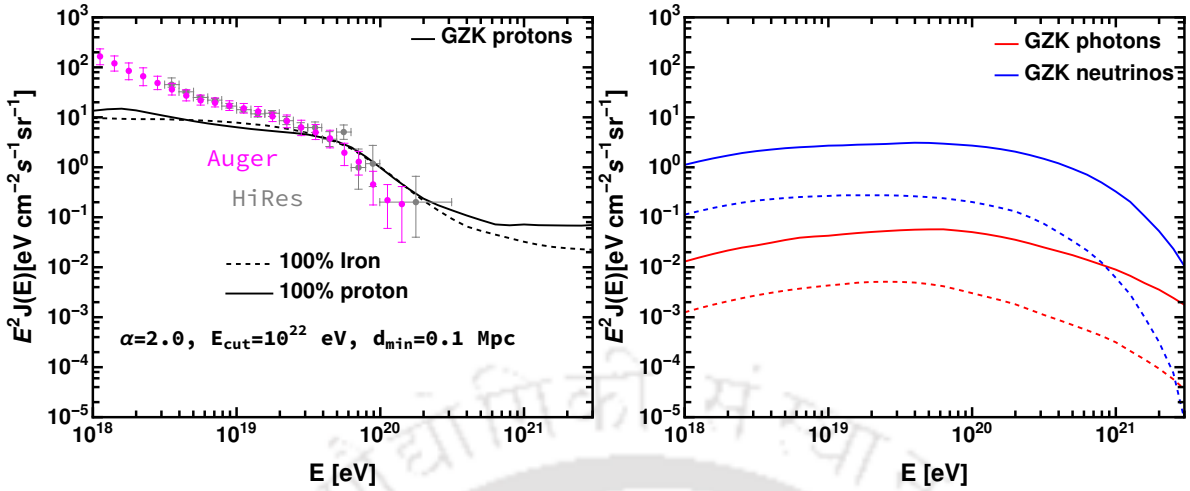

Figure 6.5: Effect of heavy elements in the primay UHECR spectrum on the GZK protons, GZK photons and GZK neutrinos (single flavour). The primay UHECR is assumed to be composed of pure Iron. The left panel shows the UHECR flux at Earth for pure proton (black continuous) and pure Iron (black dashed). The corresponding GZK neutrinos (blue) and GZK photons (red) for each case are shown in the right panel. This shows that presence of heavy elements might result in significantly lower flux of GZK secondaries.

these GZK neutrinos and GZK photons. We would like to remark that in all our computations, we consider UHECR to be composed of protons only. As a result, our flux estimates represent the upper limits of the fluxes of the secondaries produced via the GZK interaction.

6.4.3 Dependence on the cut-off energy ($E_{\rm cut}$)

The spectra of primary UHECRs is expected to fall-off rapidly at higher energies due to the maximum energy of the CRs (10). This effect is implemented to the UHECR spectrum via the cut-off energy, $E_{\rm cut}$ as defined in Eq. 6.1. This cut-off energy also influences the fluxes of GZK protons, GZK photons and GZK neutrinos. The observation of CRs above 10^{20} eV hints at possibility of $E_{\rm cut} > 10^{20}$ eV. The conventional diffusive shock acceleration theory also allows acceleration of CRs upto energies larger than 10^{20} eV (3). However in this section, to demonstrate the effect of $E_{\rm cut}$ we vary $E_{\rm cut}$ in the range $[10^{20}, 10^{22}]$ eV. The left panel of Fig. 6.6 shows the GZK proton fluxes for three values of $E_{\rm cut}$ i.e., 10^{20} eV (dashed), $10^{10^{21}}$ eV

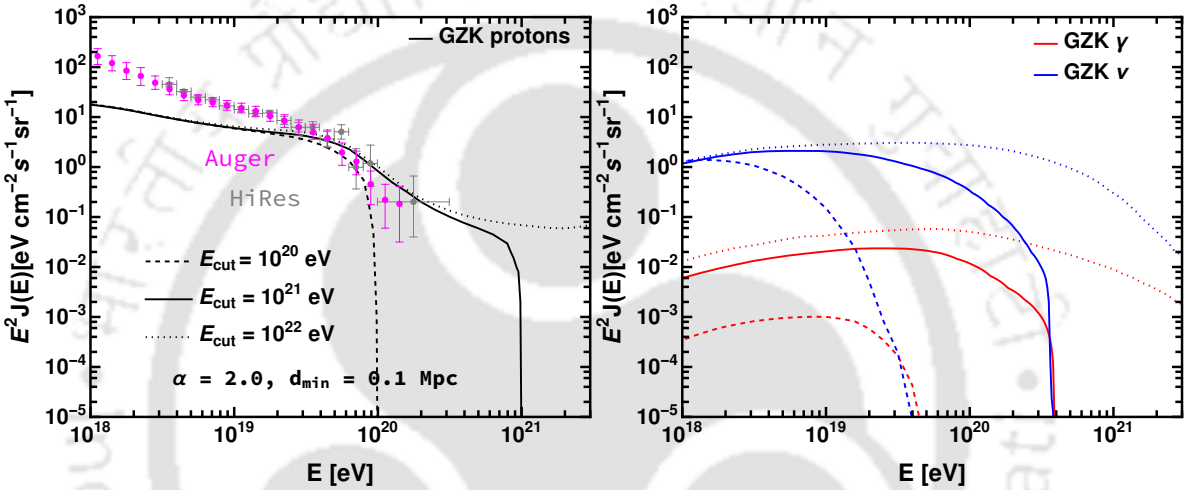

Figure 6.6: Diffuse fluxes of GZK protons, photons and neutrinos (single flavour) for different cut-off energies, i.e., $E_{\rm cut} = 10^{20}$ eV (dashed), $E_{\rm cut} = 10^{21}$ eV (solid) and $E_{\rm cut} = 10^{22}$ eV (dotted). The remaining parameters are kept fixed as $\alpha = 2.0$ eV and $d_{\rm min} = 0.1$ Mpc. The left panel shows the GZK protons fluxes for different $E_{\rm cut}$ normalised to Auger and HiRes data. The corresponding normalised GZK photon flux (red curves) and the GZK neutrino flux (blue curves) are shown in the right panel. These plots show that larger $E_{\rm cut}$ produces harder fluxes at high energies.

(solid) and 10^{22} eV (dotted). The other parameters are chosen as $\alpha = 2.0$ and $d_{\rm min} = 0.1$ Mpc for all $E_{\rm cut}$ values. The spectral shapes of all the fluxes are similar except for a sharp cut-off corresponding to $E_{\rm cut}$. The fluxes of GZK photons and GZK neutrinos corresponding to these $E_{\rm cut}$ are shown in the right panel of Fig. 6.6. The variation of $E_{\rm cut}$ produces large differences between the fluxes of different $E_{\rm cut}$. For lower values of $E_{\rm cut}$ for instance, $E_{\rm cut} = 10^{20}$ eV, both GZK photons and GZK neutrinos produce softer spectra at higher energy and fluxes fall rapidly at energies larger than 10^{20} eV. However, higher $E_{\rm cut}$ yields harder spectra at higher energies. Thus, to probe the cut-off energy in the source spectra, one needs to look at the GZK photon and GZK neutrino fluxes at higher energies.

Clearly, the observation of CR fluxes extending above 10^{20} eV suggests that the cut-off of primary UHECR must be larger than 10^{20} eV (6; 7; 5). Therefore, while studying the detection prospects, we shall consider the lower limit of the cut-off energy, $E_{\rm cut}$ to be 5×10^{20} eV. However, the conventional CR acceleration theory allows $E_{\rm cut}$ to be as large as 10^{22} eV depending on the nature of the CR source. Thus, we shall vary the $E_{\rm cut} \in [5 \times 10^{20} - 10^{22}]$ eV in order to the acceleration mechanism at the highest energies.

6.4.4 Dependence on minimum distance to source ($d_{\rm min}$)

The minimum distance to the source, $d_{\rm min}$ is also an important parameter and can effect the UHECR spectra. There are no known sources in the Milky way or any nearby galaxies that are capable of producing CRs upto energies as large as 10^{18} eV (3) . In fact, such CR accelerators might be located very far away from Earth. Thus, this is encoded in $d_{\rm min}$. The nearest galaxy (M31) to Milky way is about 1 Mpc away, this can be treated as a reasonable choice for $d_{\rm min}$. To study the effect of $d_{\rm min}$, we take the lowest value of $d_{\rm min}$ to be 0.1 Mpc. The highest value of the $d_{\rm min}$ is taken to be 100 Mpc (10). The left panel of Fig. 6.7 shows GZK proton fluxes for three different $d_{\rm min}$ i.e., 0.1 Mpc (solid curve), 50 Mpc (dashed curve) and 100 Mpc (dotted curve). The flux corresponding to $d_{\rm min} = 0.1$ Mpc has the maximum flux, i.e., minimum loss above the GZK cut-off due to the close proximity of sources. On the other hand, the flux for $d_{\rm min} = 100$ Mpc has the minimum flux estimate as the propagation loss is larger for the far away sources. Thus, we see that the GZK suppression is more pronounced (less pronounced) for larger values (smaller values) of $d_{\rm min}$, and the smaller $d_{\rm min}$ have lower attenuation.

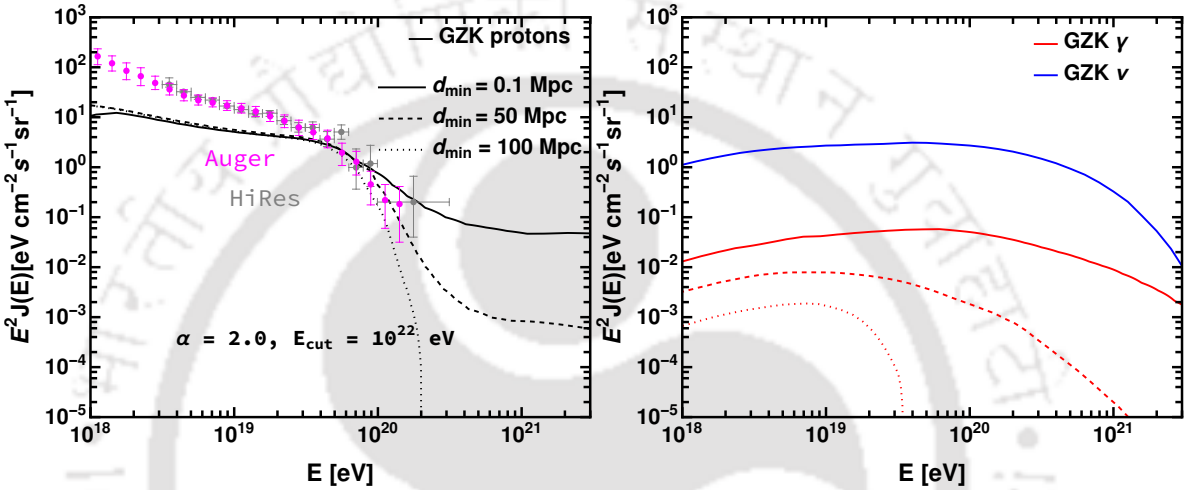

Figure 6.7: Diffuse fluxes of GZK protons, photons and neutrinos (single flavour) for different minimum distances, i.e., $d_{\rm min} = 0.1$ Mpc (solid), $d_{\rm min} = 50$ Mpc (dashed) and $d_{\rm min} = 100$ Mpc (dotted). The remaining parameters are kept fixed as $\alpha = 2.0$ eV and$E_{\rm cut} = 10^{22}$ eV. The left panel shows the GZK protons fluxes for different $d_{\rm min}$ normalised to Auger and HiRes data. The corresponding normalised GZK photon flux (red curves) and the GZK neutrino flux (blue curves) are shown in the right panel. These plots show that larger $d_{\rm min}$ produces softer proton and photons fluxes at high energies. However, the neutrino fluxes do not depend on $d_{\rm min}$ as neutrinos do not suffer losses during propagation. Therefore, the neutrino fluxes overlap for all $d_{\rm min}$.

The effect of $d_{\rm min}$ on diffuse flux of GZK photons (red) and GZK neutrinos (blue) is shown in the right panel of Fig. 6.7 for the three different values of $d_{\rm min}$, i.e., 0.1 Mpc (solid), 50 Mpc (dashed) and 100 Mpc (dotted). We note from Fig. 6.7 (right panel) that the variation of $d_{\rm min}$ does not play any role in case of diffuse flux of GZK neutrinos. This is because neutrinos are weakly interacting in nature. In contrast, the diffuse flux of GZK photons depends on $d_{\rm min}$. The larger the value of $d_{\rm min}$, the larger are the losses. Note that the suppression is more visible at higher energies and this is due to the fact that ERB is more sensitive to GZK photons at higher energies and this causes more attenuation for larger values of $d_{\rm min}$.

6.5 Conclusion

In this chapter, we have discussed the interaction of UHECR with CMB, i.e., the GZK process and subsequent production of GZK secondaries such as photons and neutrinos. We have also discussed the propagation of these secondaries through inter-galactic medium. The GZK photons are attenuated severely during propagation due to pair production losses on low energy photon backgrounds: CMB and ERB. On the other hand, the GZK neutrinos travel uninterrupted due to their weakly interacting nature. We have analysed these propagation effects on the GZK photon flux. In addition, we have discussed the dependence of the GZK photon and GZK neutrino flux on various properties of the primary UHECR spectrum.

Due to the propagation effects, the computation of GZK flux is complicated and time consuming. We have employed the public code CRPropa3.2 to estimate the fluxes of the GZK particles. We have assumed the primary UHECR spectrum to be a power law distribution with an exponential cut-off. The power law index and the cut-off energy is considered to be in the range, $(2.0-2.7)$ and $(10^{20}-10^{22})$ eV, respectively. In principle, the spectrum of UHECRs can consist of different elements together with protons. Hence, the composition of the UHECR primaries plays a crucial role in the prediction of GZK secondary fluxes. In addition to these parameters, the spatial distribution UHECR is crucial for the prediction of the GZK fluxes. Thus, the UHECR sources are considered to be distributed up to 10 Gpc. The fact that there are no known sources in the Milky-way or in its vicinity, sets up the minimum distance to the sources to be larger than 0.01 Mpc. Hence, we vary the minimum distance to the source in the

range $(0.1 - 100)$ Mpc.

We have analysed the effect of these four parameters (power law index, source composition, cut-off energy and minimum distance to the sources) on the GZK photon and GZK neutrino fluxes. The variation of the power law index has shown that smaller power law index produces harder flux at higher energies for both GZK photons and GZK neutrinos. The presence of any heavier elements in the UHECR primaries can result in lower fluxes of GZK photons and GZK neutrinos compared to the pure proton composition. The cut-off energy of the UHECRs gives rise to an exponential cut-off to the GZK photon and GZK neutrino fluxes. This exponential fall in the secondary fluxes appears at energy smaller than the primary UHECR cut-off energy. For example, for a cut-off energy of 10^{20} eV, the fluxes of the GZK photons and GZK neutrinos would fall at energies smaller than 10^{20} eV. The effect of the minimum distance to the source is found to be negligible to the GZK neutrinos due to their weakly interacting nature. However, it is found to have strong effects on the GZK photons as well as the GZK protons. Larger the minimum distance to the source, larger would be the GZK suppression in the UHECR flux at Earth (GZK protons). The GZK photon flux for large minimum distance to the source, also undergoes severe attenuation during propagation.

The GZK photon and GZK neutrino fluxes are found to have strong dependence on the UHECR source characteristics as well as the location of the UHECR sources from Earth. Hence, it is clear that estimation of these fluxes requires reasonable understanding of these characteristics. In the next chapter, we make an estimation of the GZK photon and GZK neutrino fluxes and analyse their detection prospects with multi-messenger approach.

This page was intentionally left blank.

Chapter 7

GZK fluxes and ERB: multi-messenger analysis

This chapter is dedicated to the detection prospects of the GZK photon and GZK neutrino fluxes and plausible multi-messenger implications from the detection of these GZK fluxes. The prediction of the GZK photon flux depends on the different ERB models. Hence, we start this chapter with a detail discussion on the impact of different ERB models and their uncertainties on the GZK photon flux.

7.1 Dependence of the GZK photon flux on ERB

The ERB is distributed over seven decades in frequency and impacts significantly the GZK photon flux. Any reasonable prediction of the GZK photon flux requires a good understanding and estimation of the ERB. We consider the two models in literature, PB96 (306) and Nitu21 (307). The observational constraints on ERB is only available in certain ranges of the frequencies. The ERB in the frequency range of $0.1 - 1$ GHz is constrained by radio source counts (307).

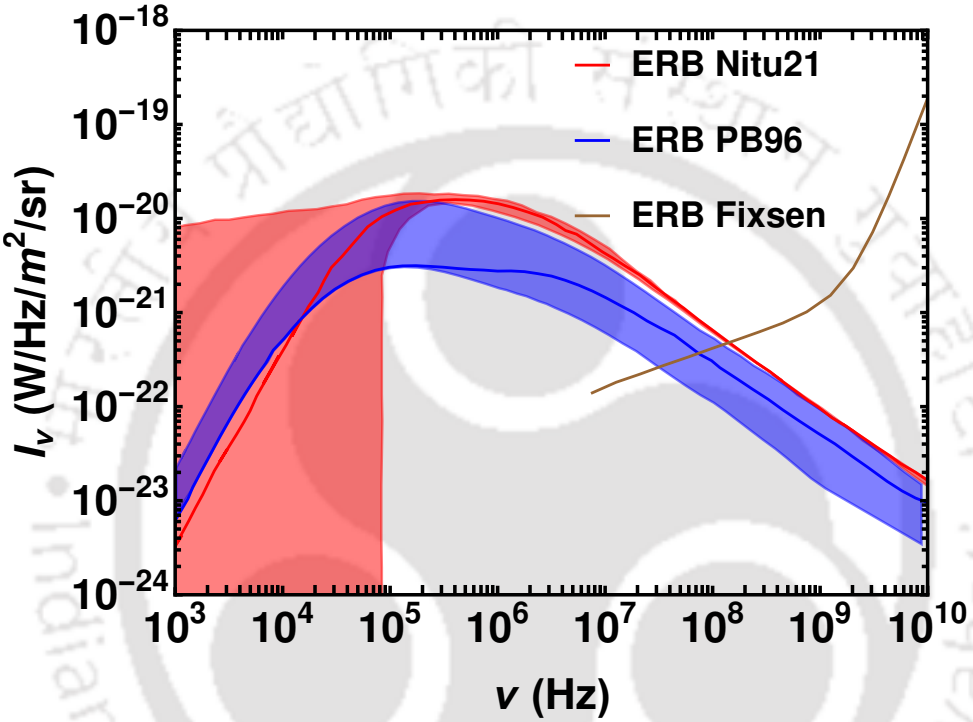

Figure 7.1: The figure shows the intensity (I_ν) as a function of frequency (ν) of different ERB models. The red curve and the red band together shows the ERB model of Nitu et al., (ERB Nitu21) (307). The red curve represents the best fit estimates, whereas the red band shows the associated uncertainty. The ERB model of Protheroe and Biermann (ERB PB96), (306) is shown in blue colour. The blue curve corresponds to the mid estimate of ERB PB96 and blue band shows the associated uncertainty. The ERB measured by the ARCADE2 experiment has been shown by the brown curve (ERB Fixsen) (309).

However, uncertainties due to unresolved radio sources cannot be ignored (327). Both the ERB models have adopted a similar approach for the estimation of ERB. The estimation is based on the modelling of radio emission of individual galaxies. Based on this individual galaxy emission model the ERB from all possible sources (radio and star forming galaxies) is obtained by using luminosity functions (306; 307). Below 100 MHz, there is significant uncertainty due to the uncertainty in the evolution of luminosity functions of radio and normal galaxies (306). On the other hand, the galactic foreground emission severely distorting the ERB produces extremely large uncertainties at KHz frequencies (307). Note that, these uncertainties at low frequencies might also get significantly impacted by different competing radiative processes such as free-free emission, synchrotron self-absorption (328; 329). Note that the ERB intensity evolves with redshift due to the evolution of the luminosity fuctions. The redshift evolution of the luminosity fuctions is of the for $(1+z)^4$.

In addition to these uncertainties, ARCADE2 experiment has reported an excess in the ERB (309). This excess was realised through the measurement of absolute sky temperature at different frequencies (3, 8, 10, 30 and 90 GHz). This analysis estimated the excess temperature, $T = 24.1 \pm 2.1$ (K) $(\nu/\nu_0)^{-2.599\pm0.036}$ ($\nu_0 = 310$ MHz) in the frequency range of 22 MHz$-$10 GHz in addition to the CMB temperature of 2.725 ± 0.001 K. The origin of this excess is not well understood. A possible explanation could be attributed to the unresolved radio sources (327). The authors in (330) adopted a simple geometry (plane parallel slab) to model the Galactic emission and estimated the extragalactic contribution. The residual ERB component is found to exceed the integrated contribution of the known population of extragalactic radio sources by factors of five or more (309; 331). However, it was shown that (332), a more realistic modeling led to estimates for the uniform extragalactic brightness that were consistent with expectations from known extragalactic radio source populations. The excess ERB has motivated dark matter interpretations for its origin (333) and could be a consequence of gravitational wave modeling for dark energy (334). Note that the CMB component at GHz frequencies dominates over the ERB component. However, excess measured by ARCADE2 experiment is still larger than the CMB. Note that observation of radio sources across a wide range of frequencies with telescopes like Low frequency Array (LOFAR) (335) and the upcoming Square Kilometer Array (SKA) (336; 337) might help to resolve this issue.

Fig. 7.1 shows two different ERB models, PB96 (306) and Nitu21 (307) with their associ-

ated uncertainties. The red curve shows the best-fit ERB spectra corresponding to ERB Nitu21 model along with the associated uncertainties shown as red band. Similarly, the blue curve and the blue band depict the typical estimate and the uncertainties of ERB PB96 model, respectively. The excess detected by ARCADE2 has also been depicted by the brown curve (ERB Fixsen). This shows that ERB has large uncertainties at both low and high frequencies which impact the prediction of the GZK photon flux (see Sec. 6.2.1 for details). Therefore, in what follows, we analyse the effect of the ERB uncertainties and the ARCADE2 results on the GZK photon flux.

The GZK neutrinos do not interact with ERB and are insensitive to the ERB. The propagation of GZK protons is impacted by CMB only and effect of ERB is negligible in the energy range our interest. Fig. 6.3 shows that the ERB plays a crucial role in the propagation of high energy (above 10^{18} eV) GZK photons and the uncertainty in the ERB leads to variation in the estimated GZK photon flux.

The effect of the above ERB models (PB96 and Nitu21) and the ARCADE2 results on the GZK photon flux are shown in the left panel of Fig. 7.2. For this, we have adopted the GZK photon flux corresponding to a primary UHECR spectra with $\alpha = 2.0$, $E_{\rm cut} = 10^{22}$ eV and $d_{\rm min} = 0.1$ Mpc. The GZK proton flux at Earth, normalized to Auger and HiRes data, is also shown on the plot. The solid blue curve shows the GZK photon flux with the medium estimate of PB96 (see Fig. 7.1), whereas the solid red curve depicts the GZK photon flux for the best-fit ERB model of Nitu21. The ERB measured by ARCADE2 at high frequencies can create additional GZK photon absorption. Thus, the effect of ARCADE2 ERB (in addition to ERB Nitu21) is shown by the brown curve. Note that the ERB models have large effect at energies above 10^{18} eV.

The ERB models of PB96 and Nitu21 have associated uncertainties as shown in Fig. 7.1 that can result in uncertainty in GZK photon flux as well. The right panel of Fig. 7.2 shows the uncertainty in the GZK photon flux due to the ERB models. The blue band shows the uncertainty due to ERB model of PB96. The lower edge in this band comes from the upper estimate of PB96, whereas the upper edge is due to the lower estimate of PB96. Similarly, the uncertainty in the GZK photon flux due to ERB Nitu21 is shown by the red band. Clearly, the uncertainty due to ERB Nitu21 is smaller than that of PB96. This is because the ERB above frequency 10^5 Hz mostly contributes to this uncertainty and at those frequencies, the uncertainty in Nitu21 model is smaller than that of PB96. The ARCADE2 results along with the upper limit

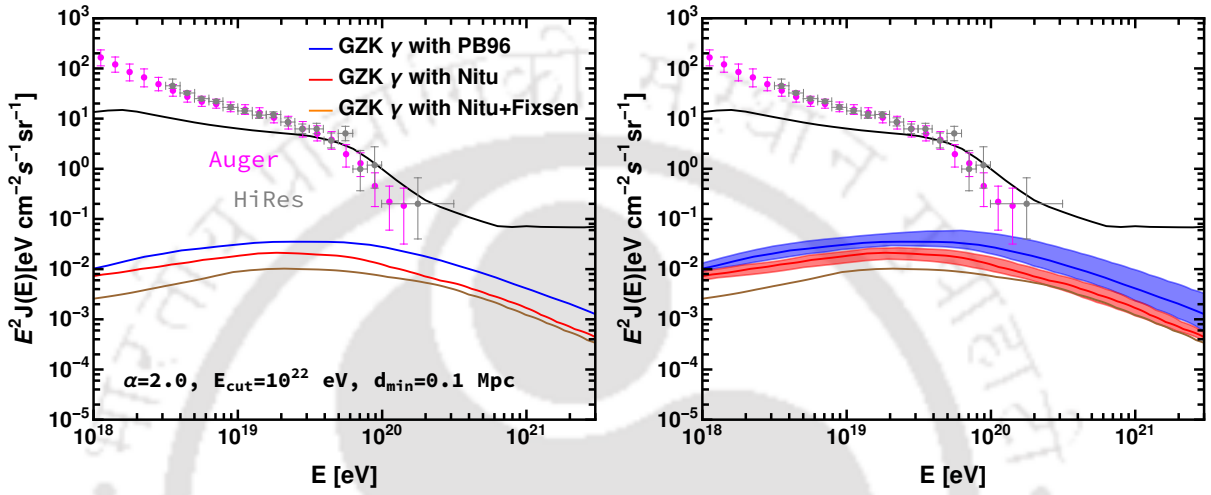

Figure 7.2: Effect of different ERB models on GZK photon propagation. The model parameters are chosen as $\alpha = 2.0$, $E_{\rm cut} = 10^{22}$ eV and $d_{\rm min} = 1$ Mpc. The left panel shows the GZK photon flux with different ERB models: PB96 (blue), Nitu21 (red) and Fixsen (brown). The blue and red curves represent the GZK photon flux with the medium estimate of PB96 and the best estimate of Nitu21 respectively. Lower ERB yields larger GZK photon flux and vice-versa. The effect of ARCADE2 ERB results (ERB Fixsen) on GZK photon flux in addition to the effect of ERB Nitu21 is also shown by the brown curve. The right panel shows uncertainty in the GZK photon flux due to the model uncertainty. The blue band shows the uncertainty in the ERB model of PB96 whereas the red band shows the uncertainty in the model of Nitu21. This shows the uncertainty in the ERB models gives rise to large uncertainties in the GZK photon flux. Note that we also plot the UHECR flux with the CR data for reference.

of ERB Nitu21 gives rise to a lower GZK photon flux as shown by the brown curve. All these ERB model estimates together with the model uncertainties yield a large (about an order of magnitude) uncertainty for the GZK photon flux. A proper understanding of these uncertainties is crucial for the detection of the GZK photon flux.

Note that, the large ERB uncertainties at low frequencies (Fig. 7.1) may not yield significant effect on the GZK photon flux. This is because the threshold energy of GZK photons for pair production on such low energy ERB photons is above 10^{21} eV. The primary cosmic ray flux above these energies ($E_{\rm cut} \sim \mathcal{O}(10^{22}$ eV)) being extremely small, the low energy ERB impact is much below the sensitivity limitations of various UHE photon and UHE neutrino detectors.

7.2 Detection prospects: multi-messenger approach with GZK photons and GZK neutrinos

As pointed out before, along with the flux of UHECRs there is a guaranteed flux of GZK neutrinos and GZK photons. Naturally, measuring the flux of these different messengers at UHE would allow us to probe the nature of these UHECRs and their sources much better. As far as the detection of UHECR and GZK photons is concerned, we have the currently operational UHECR detectors such as the Pierre Auger Observatory (Auger) (52; 319; 5; 321), Telescope Array (TA) (53) as well as proposed detectors such as Giant Radio Array for Neutrino Detection (GRAND) [1] (338; 27). In addition, for the GZK neutrino detection, we also have Antarctic Impulsive Transient Antenna (ANITA) (339), the IceCube neutrino observatory (IceCube and upcoming IceCube-Gen2) (314; 25), the Askaryan Radio Array (ARA) (51), the Radio Ice Cherenkov Experiment Observatory (RICE) (340). These neutrino experiments rely on the principle of Askaryan effect (339; 51; 27; 25). Using lunar Cherenkov technique, SKA will also be able to detect the GZK neutrinos. For a comparison of sensitivities of different detectors, see (319; 25).

In Fig. 7.3, we show the flux of GZK photons (left panel) and GZK neutrinos (right panel) as a function of energy for the benchmark values of parameters given in Table 7.1, considering UHECR primaries to be protons only. The units of the fluxes in each plot are appropriately

[1] Auger and GRAND can also detect UHE neutrinos along with the UHECRs.

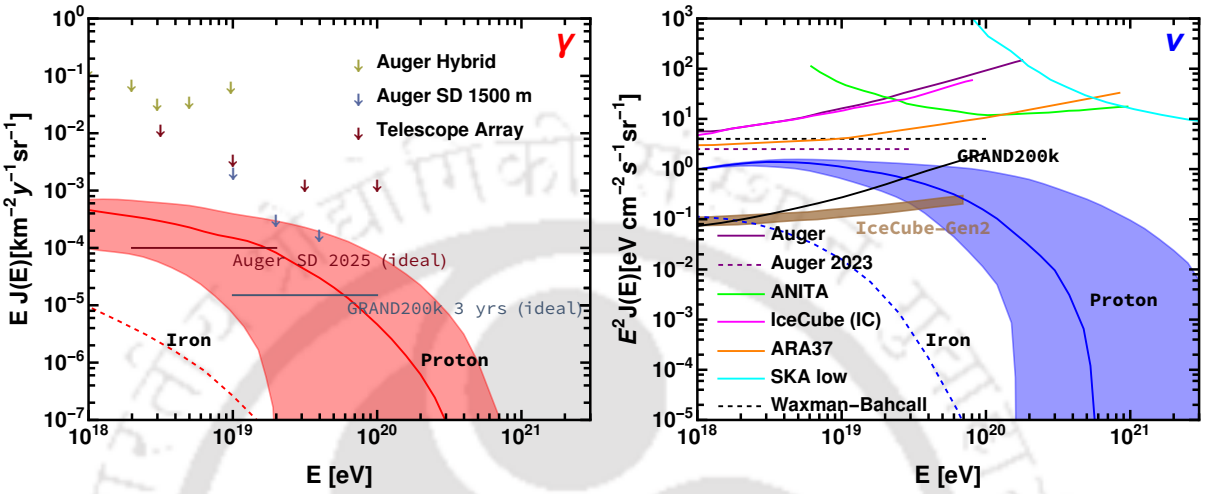

Figure 7.3: Detection prospects of GZK photon (left) and single flavour neutrino (right) fluxes. The left (right) panel shows the typical estimate of GZK photon (neutrino) flux by the red (blue) curve with associated uncertainty in red (blue) band. The typical estimate is obtained by choosing the parameters as $\alpha = 2.4$, $E_{\rm cut} = 10^{21}$ eV and $d_{\rm min} = 1$ Mpc with minimum estimate of ERB PB96. For the upper limit of the band, we take $\alpha = 2.2$, $E_{\rm cut} = 10^{22}$ eV and $d_{\rm min} = 0.1$ Mpc with minimum estimate of ERB PB96, while for the lower limit, we choose $\alpha = 2.7$, $E_{\rm cut} = 5 \times 10^{20}$ eV and $d_{\rm min} = 100$ Mpc with ERB Fixsen and the maximum estimate of ERB Nitu. The sensitivities of the UHE photon and neutrino detectors have also been also plotted. The flux predictions are consistent with the experimental limits (Auger, TA) and theoretical limit i.e, Waxman-Bahcall for neutrino. Most of the present detectors are not sensitive to the fluxes. However, future proposals will have sensitivity for detection like Auger 2023 for photon, GRAND for photon and neutrino, IceCube-Gen2 for neutrino. We have also shown the lower limit of the fluxes of GZK photons (red dashed) and neutrinos (blue dashed) for 100% UHECR primaries.

Parameters	Benchmark value	Range
α	2.4	$2.2 - 2.7$
$E_{\rm cut}$ (eV)	10^{21}	$5 \times 10^{20} - 10^{22}$
$d_{\rm min}$ (Mpc)	1	$0.1 - 100$

Table 7.1: The choice of benchmark parameter values and the range considered in our analysis for Fig. 7.3, see Sec. 6.4 for justification.

chosen so as to draw a comparison with the existing sensitivities of different experiments. The GZK photon flux has been plotted in units of km^{-2} y^{-1} sr^{-1}, whereas the GZK neutrino flux is shown in units of eV cm^{-2} sr^{-1}. In the left (right) panel, the red (blue) solid curve corresponds to the benchmark values whereas the red (blue) band corresponds to the range of variation of parameters given in Table 7.1 for gamma-rays (neutrinos). The photon band also incorporates the ERB uncertainty. For the upper limit of the red band, we consider the minimum estimate of PB96 ERB, whereas the lower limit is obtained by considering the maximum estimate of ERB Nitu21 together with the ARCADE2 results (ERB Fixsen). The sensitivities of existing detectors are depicted on the plots which allow for a direct comparison with our prediction. Note that the GZK neutrino band below 10^{20} eV is narrower compared to the GZK photon band. This is due to the fact that the effect of UHECR source parameters (α and $E_{\rm cut}$) is more prominent at the higher energies (see Sec. 6.4) and there is no propagation effect on the GZK neutrinos. It is evident from observations that there are heavier elements in the UHECR spectrum. The heavier elements in the UHECRs can result in lowering the GZK photon and GZK neutrino fluxes. Hence, in addition to the pure proton primary case, we also show the GZK photon (red dashed) and GZK neutrino (blue dashed) fluxes due to heavier composition, considering 100% iron primaries. For this estimation, we consider the parameter values as $\alpha = 2.7$, $E_{\rm cut} = 5 \times 10^{20}$ eV and $d_{\rm min} = 100$ Mpc. These fluxes show that the uncertainty in the GZK photon and GZK neutrino fluxes can extend about an order lower than the lower limit of the pure proton case. For any mixed UHECR composition, the corresponding GZK photon (neutrino) flux should fall in between the upper edge of the red (blue) band and the red (blue) dashed curve.

From left panel of Fig. 7.3, it is evident that the existing detectors do not have the sensitivity to probe the predicted GZK photon flux. However, Auger SD 2025 (brown line) (321) and GRAND 200k 3 years (gray line) (338) may be able to access the GZK photon flux. Likewise,

from the right panel it is clear that existing neutrino detectors are insensitive to the predicted GZK neutrino flux. Only IceCube-Gen2 (25) and GRAND200k (338; 27) could provide us with opportunities of detection of these fluxes in the future. Note that the IceCube-Gen2 sensitivity is a band rather than a line due to the radio array design uncertainties of the detector (25).

7.2.1 What can we learn from non-observation GZK photon and GZK neutrino flux ?

Current upper limits on the UHE photon flux by different detectors (Auger and TA) have been shown by the downward arrows in the left panel of Fig. 7.3. The sensitivities of the Auger 2025 upgrade (brown line) (321) and the future proposal, GRAND200k 3 years (gray line) (338) have also been plotted. The upper limit on the GZK photon flux is well below the sensitivity of the Auger Hybrid (52) and TA (53) detector. However, The sensitivity of the Auger SD 1500 m (52) detector is found to be close to the benchmark flux in the energy range $(1-4)\times 10^{19}$ eV. The photon fluxes (in the red band) in this energy range above the typical flux mostly come from the smaller power law index ($\alpha < 2.4$) and large cut-off energy ($E_{\rm cut} = 10^{22}$ eV) of the primary UHECR spectra. The upper limit at these photon energies ($< 10^{20}$ eV) also corresponds to a smaller ERB flux at the medium and higher frequencies. The non-observation of the GZK fluxes at Auger and the sensitivity of Auger SD 1500 m slightly overlapping with these GZK photon fluxes can be due to large spectral index, $\alpha \geq 2$ and/or heavy UHECR primaries. . However, one needs to detect the GZK photon flux over a wide energy range to constrain these parameters. The upcoming Auger upgrade and the GRAND detector will be able to put such constraints more firmly.

Similarly, sensitivities of different UHE neutrino detectors are plotted in the right panel of Fig. 7.3. The neutrino flux corresponding to our benchmark parameter values is found to be consistent with the Waxman-Bahcall limit (341) (Black dashed line). The neutrino benchmark flux is also below the sensitivity of IceCube (magenta curve) (25) and Auger (purple curve) (319) and is consistent with the GZK non-observation at both the detectors. The combined sensitivity of ANITA I + II + III (green curve) (342) is found to be above the upper limit on the GZK neutrinos. The sensitivities of the future detectors ARA37 (orange curve) (51) and

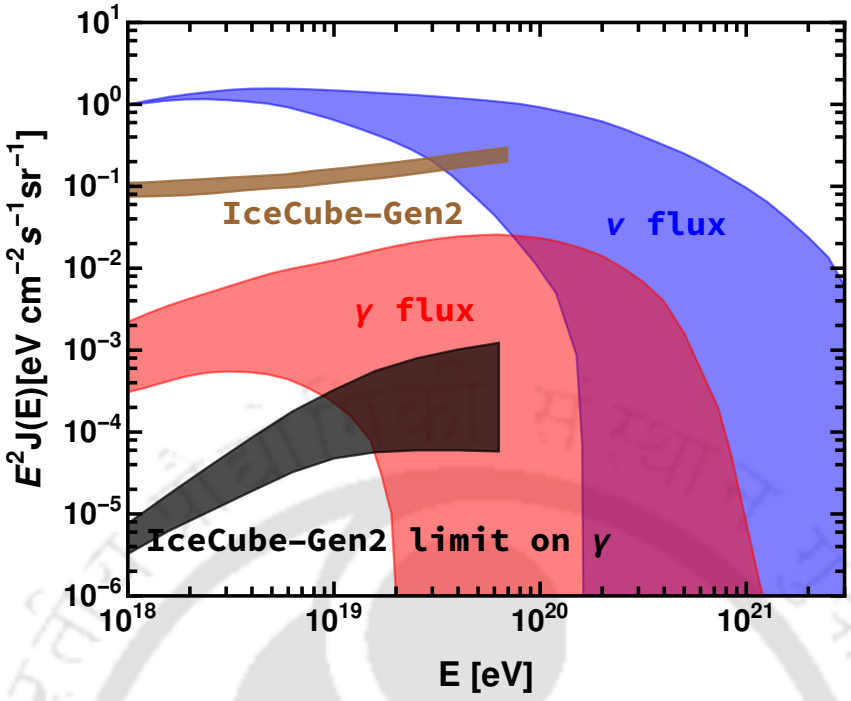

Figure 7.4: Constraints on GZK photon flux from detection/non-detection of GZK neutrinos at IceCube-Gen2. The blue and red bands show our estimated GZK neutrino (ν, single flavour) and GZK photon (γ) fluxes respectively. The brown band shows the sensitivity of IceCube-Gen2 to GZK neutrinos. Following the neutrino sensitivity (brown band), the corresponding limit on the GZK photon flux has been estimated, shown by the black band. This band also takes into account of the ERB uncertainties. Detection of GZK neutrinos by IceCube-Gen2 would mean that the GZK photon flux is above (or within due to ERB uncertainties) this black band.

SKA low (cyan curve) (319; 25) are also found to be above the GZK neutrino flux upper limit. Thus, none of these detectors are capable of probing the benchmark neutrino flux. However, the proposed sensitivity (brown band) of the next generation of IceCube experiment (IceCube-Gen2) will be able to probe the GZK neutrino flux upto 10^{20} eV. It should be noted that these neutrino detectors can not probe the effect of the parameter $E_{\rm cut}$. Further, the neutrino flux is nearly independent of the parameter $d_{\rm min}$, hence $d_{\rm min}$ can only be probed through the detection of GZK protons and photons. In addition, the GZK neutrino flux at lower energies ($< 10^{19}$ eV) is almost independent of the parameters α, $E_{\rm cut}$ and $d_{\rm min}$. The variation of the neutrino flux in these energies can be due to composition effects only. Hence, detection of GZK neutrinos in IceCube-Gen2 and GRAND will help us to constrain the UHECR composition.

7.2.2 What can IceCube-Gen2 limit say about GZK photon flux ?

Having discussed the flux prediction and sensitivity limits of the existing detectors for the GZK photons and GZK neutrinos separately, we now address if observation of any one of the component can have implications for detection of the other component, thereby utilizing the power of multi-messenger approach. In particular, we discuss the implications of GZK neutrino flux measured by IceCube-Gen2 on GZK photon flux. As we have seen from Fig. 7.3, IceCube-Gen2 detector is sensitive to the GZK neutrinos upto 10^{20} eV. Using IceCube-Gen2 neutrino sensitivity, we compute the corresponding GZK photon flux limit. We compute this limit for the scenario of UHECR primary to be protons only.

For this estimation, we use the IceCube-Gen2 limit to obtain the normalization and the spectral index of the primary UHECR proton flux. However, this primary UHECR proton flux may produce different GZK photon flux due to different propagation effects. In this regard, we estimate the GZK photon flux corresponding to the neutrino flux sensitivity of IceCube-Gen2 considering propagation effects of both the CMB and ERB. The uncertainties in the ERB give rise to a band in the GZK photon flux. Our results are shown in Fig. 7.4. The constraints from IceCube-Gen2 together with the GZK neutrino (blue) and photon (red) fluxes (see Fig. 7.3) from our analysis are plotted in Fig. 7.4. The brown band shows the GZK neutrino flux sensitivity of IceCube-Gen2 whereas the black band represents the corresponding constraint on the GZK photon flux. The GZK photon band is wider in comparison the neutrino sensitivity band primarily due to the effect of ERB uncertainties. Indeed, our limit of the GZK photon flux is well below the model prediction in the corresponding energies. Thus pointing at the following crucial multi-messenger implications:

- If IceCube-Gen2 detects GZK neutrinos - the GZK photon flux is guaranteed from the GZK interaction and expected to lie above or within the black band (Fig. 7.4).
- If IceCube-Gen2 does not detect GZK neutrinos - it would create a tension between the observed UHECR data and our understanding of the GZK process which links the fluxes of UHECR primary and secondaries.

This photon flux corresponding to the IceCube-Gen2 neutrino sensitivity can be interpreted as multi-messenger limit on the GZK photon flux. However, it shouldn't confused with the

lowest GZK photon flux that nature can produce. The present limit is for 100 percent protons, however we found that different composition of UHECR primaries will lead to very similar multi-messenger limit as the overall normalization is fixed by the IceCube-Gen2 limit. We have also found that there could be a little variation in the spectral shape of this limit due to the choice of the primary UHECR spectral index. Nevertheless, this difference is found to be negligible compared to the uncertainties due to the ERB. However, it should be noted that the GZK photons suffer from propagation uncertainties and hence it is not possible to derive a similar limit for the GZK neutrinos from the detection of GZK photons. Also, different UHECR parameters (source and propagation) lead to the same GZK photon flux as shown in Fig. 7.3. This arbitrariness makes the reverse correspondence from GZK photons to GZK neutrinos inconclusive.

7.3 Conclusion

In this chapter, we have numerically estimated the diffuse flux of GZK secondaries (neutrinos and photons) and discussed possibilities of their detection with current and upcoming UHECR and UHE neutrino experiments. For estimation of the fluxes, we have used the code CRPropa 3.2 assuming that UHECR primary has a power-law distribution with an exponential cut-off. In Chapter 6, we have analysed the dependence on various parameters such as the spectral index (α), the cut-off energy ($E_{\rm cut}$) and the minimum distance to the source ($d_{\rm min}$) and based on these analysis, we have estimated the GZK secondary flux in this chapter. In order to obtain the expected flux of the GZK photons, it is important to consider the attenuation of GZK photons by the CMB as well as ERB. We have considered the impact of both the CMB and ERB (including the impact of associated uncertainties) on the propagation of GZK photons. Finally, we have also discussed the possible multi-messenger phenomenological implications of GZK neutrinos (especially with IceCube-Gen2) on the flux of GZK photons.

The predicted GZK photon flux is found to be below the sensitivities of the telescopes, Auger and TA. However, in future, Auger 2025 and GRAND200k will be able to probe the GZK photon flux parameter space. The sensitivity of GRAND200k is expected to be one order smaller than our predicted upper limit of the GZK photon flux and will be the best option for GZK photon detection. In addition, we have found that the uncertainties at the high frequency

part of the ERB spectra can have significant impact on the low energy GZK photon flux. This low energy flux being detectable at the upcoming UHE photon detectors, Auger SD 2025 and GRAND200k can provide us better understanding of the high energy ERB spectra uncertainties (like, ARCADE2 radio excess). The IceCube-Gen2 neutrino detector being sensitive in these low energies can also provide multi-messenger constraints.

The predicted GZK neutrino flux is beyond the reach of the UHE neutrino detectors like Auger, IceCube, ANITA, ARA37 and SKA low. The GZK neutrino flux estimate is found to be in excellent agreement with the Waxman-Bahcall limit (341). The reach of the proposed IceCube-Gen2 will be better and hence, it is expected that IceCube-Gen2 would be able to detect GZK neutrinos. It should be noted that uncertainties in source parameters have little impact on the GZK neutrino flux at energies below 10^{20} eV and can be used to calibrate the GZK photon flux for any multi-messenger study.

Apart from discussing the flux prediction and sensitivity limits of the existing detectors for the GZK photons and GZK neutrinos, we have also addressed the impact of detection of any one of the component on the other component utilizing the power of multi-messenger approach. Using IceCube-Gen2 neutrino sensitivity, we have computed the corresponding GZK photon flux limit. This limit is consistent with our model predictions and yields the following crucial conclusions. Any future detection of GZK neutrinos in IceCube-Gen2 will imply a guaranteed GZK photon flux which can expected within this limit. However, non-detection of GZK neutrinos at IceCube-Gen2 may create a tension between the observed UHECR flux and the present understanding of the GZK process. Moreover, detection of the GZK secondaries can also indirectly lead to an improved understanding of the ERB.

Note that our prediction of GZK neutrinos and GZK photon fluxes is based on the assumption of pure proton composition of UHECR primaries. However, the presence of heavy elements in the UHECR primaries might result in lower fluxes depending on the fraction of different heavy elements. Though this is expected to be a minor effect, in principle, the fluxes of GZK neutrinos and GZK photons presented in this work are representing the upper limits, in regards to the presence of heavier elements in the UHECR fluxes.

This page was intentionally left blank.

Chapter 8

Summary and Conclusion

The study of CRs is fascinating as these particles spread over almost 12 decades of energies from GeV to ZeV and come from different parts of our Universe. Understanding the CRs will help us in unfolding several issues in CR physics such as their sources, composition and production mechanism. Observations by various CR experiments have provided us with a reasonable understanding of these issues but not yet complete. Advancements of different gamma-ray and high energy neutrino telescopes have opened up a new window to multi-messenger astrophysics providing new insights into the CR physics paradigm. This is because CRs during propagation can produce different secondary particles such as gamma-rays and high energy neutrinos. Neutrinos being weakly interacting propagate through space without any losses and can be useful in understanding CR source properties. While the gamma-rays attenuate during propagation due to interaction with these background photons such as CMB, ERB making them essential to understand the nature of the propagation background. Thus, combined detection of gamma-rays and neutrinos and a multi-messenger analysis are crucial for the understanding of the sources and propagation of CRs. Neutrino detectors such as IceCube, Auger (also upcoming KM3NeT, IceCube-Gen2, GRAND) and gamma-ray detectors like Fermi-LAT, Auger (also upcoming CTA, GRAND) are the drivers of this multi-messenger approach.

In this thesis, we have performed phenomenological studies of gamma-ray and high energy neutrino fluxes produced by high energy CRs as well as UHECRs interacting with different target particles and analyse their detection prospects with the various telescopes mentioned above. We have also utilized (wherever applicable) the multi-messenger connection discussed above to constrain these fluxes. In the following, we provide a brief summary of the different analyses done in this thesis and highlight the major findings.

In Chapter 2, we have estimated the gamma-ray and high energy neutrino fluxes from the 12 Galactic sources (known as PeVatrons) detected in TeV-PeV gamma-rays by LHAASO, (22; 28). These detected gamma-rays are expected to be produced by CRs accelerated in sources like, SNR or pulsars through either hadronic process (CR protons interacting with neighbouring molecular cloud, i.e, $p-p$ interaction) or leptonic process (inverse Compton by CR electrons). In the hadronic channel, gamma-rays are accompanied by high energy neutrinos as both are produced through charged and neutral pion decays created by pp collision. Therefore, detection of these neutrinos is crucial to probe the hadronic nature of these sources. We have adopted two prototype sources (SNR G106.3+2.7, SNR G40.5–0.5) for modeling ($p-p$ interaction) the gamma-ray emission and fitted the gamma-ray fluxes to the observed data (22; 28). Using this fitting approach, we have obtained the corresponding neutrino fluxes for these two sources. We have also estimated the neutrino fluxes for the remaining LHAASO sources and analyse their detection prospects with IceCube, IceCube-Gen2 and KM3NeT. Our study have shown that several of these LHAASO sources will be discoverable in the upcoming IceCube-Gen2 and KM3NeT detectors.

In Chapter 3, we have estimated gamma-ray and neutrino fluxes from different types of young SNe: IIn, II-P, IIb/II-L and Ib/c. In this young SNe scenario, gamma-rays and neutrinos can be produced by inelastic $p-p$ interaction caused by SN ejecta crashing into a dense CSM. This interaction of SN ejecta with CSM can produce a fast forward shock accelerating particles to very high energies (upto a few decades of PeV). The fluxes of these secondary gamma-rays and high energy neutrinos depend on the properties of the shock as well as on the CSM environment, i.e, size and density of the CSM. The gamma-ray flux however can undergo absorption due to pair production on low energy thermal photons in the CSM. The amount of gamma-ray attenuation depends on the average energy of the thermal photons as well as their density. Considering all these effects, we have estimated the fluxes of gamma-rays and high energy neu-

trinos for different types YSNe. We have found that type IIn YSNe produce the largest fluxes of gamma-rays and neutrinos as the CSM in these SNe are densest. The second largest fluxes are produced by Ib/c (LT), which have dense CSMs far away from the progenitors giving rise to late CSM interaction and followed by the fluxes of II-P. The fluxes produced by IIb/II-L and usual Ib/c YSNe are found to be very small compared to the other types as the CSMs found in these SNe are very thin. Furthermore, we have analysed the detection prospects of these different YSNe with current and upcoming gamma-ray (Fermi-LAT and CTA) and neutrino (IceCube, IceCube-Gen2 and KM3NeT) detectors. We have found that type IIn YSNe having the largest fluxes are detectable upto 10 Mpc in both gamma-rays and neutrinos, whereas type Ib/c (LT) and II-P are detectable upto a few Mpc. The remaining YSNe are found to be detectable only at Galactic distances.

In Chapter 4, we have performed a detailed analysis on the gamma-ray and neutrino flux from Ib/c (LT) YSNe following different CSM models of SN 2014C in literature. Observations of certain SNe, such as SN 2014C, in both X-ray and radio wavelengths have unveiled a phenomenon where they experience a resurgence in brightness over a period of approximately one year following their initial detection. This intriguing discovery suggests a transformation from a hydrogen-poor SN of Type Ib/c to a hydrogen-rich SN of Type IIn. In our study, we have undertaken calculations to estimate the neutrino and gamma-ray fluxes emanating from such Ib/c (LT) SNe. Our calculations have taken into account interactions between protons accelerated by the shockwave and the non-relativistic protons within the CSM. We have considered three different CSM models, inspired by recent electromagnetic observations, to estimate the fluxes of gamma-rays and neutrinos. Furthermore, we have assessed the potential for detecting these signals using existing and forthcoming gamma-ray telescopes such as Fermi-LAT and the CTA, as well as neutrino observatories like IceCube, IceCube-Gen2, and KM3NeT. Our research aligns with the existing results, the non-observation of gamma-rays and high energy neutrinos from SN 2014C. Nevertheless, our analysis suggests promising prospects for detecting late-time emission from SNe using the Cerenkov Telescope Array and IceCube-Gen2 (in conjunction with Fermi and IceCube), particularly if the SN event occurs within a range of 10 Mpc (4 Mpc).

In Chapter 5, we have estimated the diffuse fluxes of gamma-rays and high energy neutrinos from different types of YSNe discussed in Chapter 3 and Chapter 4. The estimation of

these diffuse fluxes is motivated by the diffuse gamma-ray observation by Fermi-LAT as well as the diffuse neutrino flux detected by IceCube. To calculate these diffuse fluxes, several key factors come into play, including the initial gamma-ray and neutrino fluxes at the source (see Chapter 3), the rate of CCSNe as a function of redshift, the distribution of different types of SNe, and the parameters of the cosmological model (ΛCDM) (45). When computing the diffuse fluxes for individual SN types, we have also considered the abundance of each type in the local Universe (277). The analysis reveals that the diffuse fluxes of gamma-rays and high-energy neutrinos originating from Type IIn SNe are the most substantial, followed by Type II-P, Type Ib/c, and Type IIb/II-L. We have also calculated the overall diffuse fluxes encompassing all these YSN types. Interestingly, the total diffuse neutrino flux is found to be consistent with the data from IceCube's High-Energy Starting Events (HESE). The corresponding diffuse gamma-ray flux remains significantly below the data from Fermi-LAT's Isotropic Gamma-Ray Background (IGRB). This suggests that for such YSNe with dense CSM, the origin of the IGRB and HESE signals may not share a common source and no tension between HESE and IGRB observations for YSNe being the source for HESE.

In Chapter 6, we delved into the intricate processes governing the propagation of UHECRs through the intergalactic space. We have examined the production and propagation of GZK photons and GZK neutrinos, along with the significance of the ERB in the context of GZK photon flux propagation. It is expected that the CRs reaching beyond the GZK cut-off threshold energies (approximately 4×10^{19} eV) interact substantially with the CMB and suffer significant attenuation of the UHECR flux. Therefore, the observation of CRs beyond the GZK cut-off presents a new avenue for investigating the origin and propagation mechanism of UHECRs. The GZK interaction, involving proton collisions with CMB photons ($p + \gamma_{CMB}$), results in the production of charged and neutral pions through the Δ^* resonance, subsequently decaying into gamma-rays (GZK photons) and neutrinos (GZK neutrinos) (49). Detecting these GZK secondary particles offers vital insights into the UHECR's source and propagation. To calculate the fluxes of these GZK secondary particles, it is imperative to comprehend the properties of the primary UHECR sources as well as the propagation of these secondaries through various intervening backgrounds. We have formulated the primary UHECR spectrum as a power-law distribution with an exponential cut-off, representing the maximum energy attainable by CRs (10; 65; 310). Using this source spectrum model, we have illustrated the production of GZK photons and GZK neutrinos. The GZK photon flux experiences significant attenuation due to

interactions such as pair production and inverse Compton scattering with the CMB and the ERB. The ERB spectrum, characterized by considerable model uncertainties and influenced by the ARCADE2 radio excess, plays a pivotal role in shaping the predictions for the GZK photon flux, resulting in substantial uncertainties (306; 307; 309). To exemplify these propagation effects, we calculate the attenuation of GZK photons independently when interacting with the CMB and the ERB using the CRPropa 3.2 code (310). We have analysed the dependence of GZK neutrino and GZK photon flux on the UHECR source parameters (spectral index and cut-off energy) as well as on the minimum distance to the UHECR sources. Our analysis in this chapter establishes the expected properties of the GZK fluxes for variation of different source and background characteristics. The large spectral index of the primary UHECR spectrum is found to imply softer secondary flux and smaller cut-off energies of the primary UHECR spectrum have resulted in exponential fall of the secondary flux at smaller energies. The GZK photon flux is found to be strongly dependent on the minimum distance to the source. For sources located far away from Earth, the GZK photon flux suffers large attenuation. However, the neutrinos being weakly interacting remain unaffected by the minimum distance to the sources. We have also shown that impact of ERB on the GZK photon flux is more pronounced at energies larger than 10^{19} eV.

In Chapter 7, we have first analysed the impact of ERB model uncertainties on the GZK photon flux propagation. The two ERB models in the literature: PB96 and Nitu21 have significant uncertainties due to observational limitations. In addition to these model uncertainties, the ARCADE2 experiment's measurement has identified an excess radio signal at GHz frequencies. As the propagation of GZK photons is strongly impacted by the ERB photons leading to severe attenuation, the uncertainties in the ERB models can also affect the prediction of GZK photon flux. We have analysed the impact of the ERB model uncertainties on the GZK photon flux at Earth and found that these uncertainties could lead to about a order of uncertainties in the GZK photon flux. Since the GZK neutrinos are not affected by the ERB or any other propagation effects, their detection will help in constraining the UHECR source properties, eventually leading to contraints on the GZK photon flux. This constrained GZK photon flux is also dependent on the ERB model uncertainties. This multi-messenger probe might be feasible with the upcoming UHECR (Auger upgrade, GRAND200k) and UHE neutrino (IceCube-Gen2) detectors. In order to understand the detection prospects of the GZK fluxes, we compute the GZK photon and neutrino fluxes based on constraints available from UHECR observations. We have found that

the estimated GZK photon and GZK neutrino fluxes are below the sensitivities of the currently operating detectors. However, the future planned experiments mentioned above are found to have substantial sensitivities to these fluxes. In fact, the sensitivity of IceCube-Gen2 to GZK neutrino flux is found to be best among all the detectors and will be able to hunt the GZK neutrino flux one order lower than the current prediction. So the detection of GZK neutrinos will allow us to constrain the GZK photon flux. Following this multi-messenger approach, we have also computed the limit on the GZK photon flux corresponding to the IceCube-Gen2 neutrino sensitivity, considering propagation uncertainties due to ERB.

To conclude, we have investigated the potential for detecting gamma-rays and UHE neutrinos originating from a range of astrophysical sources and examined the multi-messenger implications of such detections. The presence of substantial uncertainties in the fluxes of gamma-rays and high-energy neutrinos is primarily attributed to observational limitations. Nevertheless, it's important to note that the inventory of astrophysical observations continues to evolve regularly, thanks to advancements in various telescope technologies. Looking ahead, the forthcoming IceCube-Gen2 and GRAND detectors hold the promise of unveiling a multitude of cosmic ray mysteries in the near future.

Appendix A

Acceleration and different cooling timescales of CRs

Shock accelerated protons lose energy through different processes such as pp interactions, dynamic or adiabatic losses, proton synchrotron, inverse Compton, Bethe-Heitler, etc. In this Appendix, we provide an overview of the different energy loss time scales for high energy protons and compare them with the acceleration time scales.

Acceleration time scale

The proton acceleration time scale is given by (174):

$$t_{\rm acc} = \frac{6E_{\rm p}c}{eBv_{\rm sh}^2}\,, \tag{A.1}$$

where the magnetic field B is given in Sec. 3.2.1.

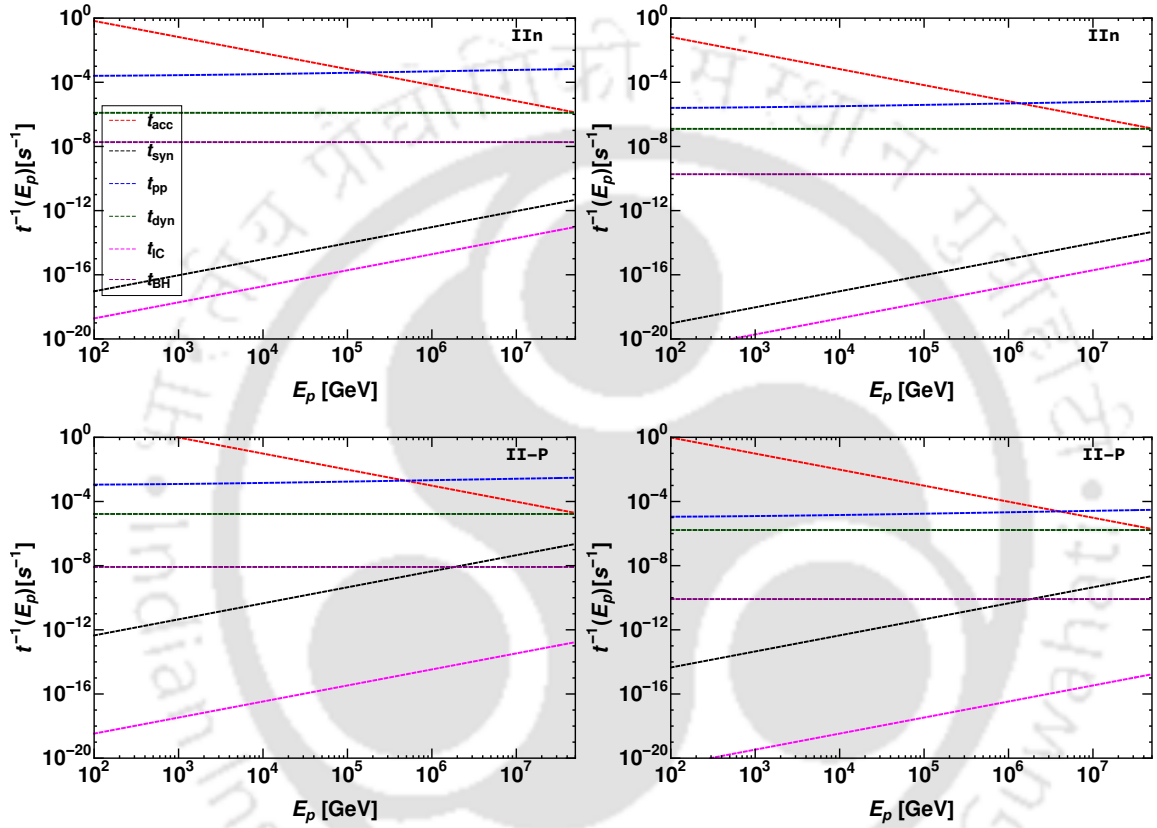

Figure A.1: Acceleration time scale of protons and various proton energy loss processes as functions of the proton energy for Type IIn YSNe (top panels) and Type II-P SNe (bottom panels) using the parameters in 3.1 and Sec. 3.4.2. The left panels show the interaction time for $r = r_{\rm in}$, while right panels consider $r = 10\ r_{\rm in}$. Proton cooling is dominated by pp losses and therefore the total cooling timescale is the same as the pp collision timescale.

Adiabatic loss time scales

The adiabatic loss time scale for protons is same as the dynamical time scale and is given by:

$$t_{\rm ad} \sim t_{\rm dyn} = \frac{r}{v_{\rm sh}}. \tag{A.2}$$

Proton-proton collision time scale

The pp collision time scale is given by

$$t_{\rm pp} = (\kappa_{\rm pp}\sigma_{\rm pp}(E_{\rm p})n_{\rm CSM}(r)c)^{-1}, \tag{A.3}$$

where $\kappa_{\rm pp} = 0.5$ is the pp collision inelasticity.

Proton synchrotron time scale

High energy protons may lose energy due to proton synchrotron radiation. The corresponding synchrotron time scale is given by (343; 344):

$$t_{\rm syn} = \frac{\gamma m_{\rm p} c^2}{P_{\rm syn}}, \tag{A.4}$$

where $\gamma = E_{\rm p}/m_{\rm p}c^2$ and $P_{\rm syn}$ is the synchrotron power loss and is given by

$$P_{\rm syn} = \frac{4}{3}\sigma_T c \left(\frac{m_{\rm e}}{m_{\rm p}}\right)^2 \frac{B^2(r)}{8\pi} \left(\frac{v_{\rm sh}}{c}\right)^2 \gamma^2 , \tag{A.5}$$

where $\sigma_{\rm T}$ is the Thomson scattering cross-section.

Inverse Compton loss time scales

Protons may lose energy to low energy SN photons via inverse Compton scattering and the corresponding loss time scale is given by (343)

$$t_{\rm IC} = \frac{\gamma m_{\rm p} c^2}{P_{\rm IC}}, \tag{A.6}$$

where the inverse Compton power $P_{\rm IC}$ is given by

$$P_{\rm IC} = \frac{4}{3}\sigma_{\rm T} c U_{\rm ph}(r)\gamma^2 \left(\frac{v_{\rm sh}}{c}\right)^2 \left(\frac{m_{\rm e}}{m_{\rm p}}\right)^2, \tag{A.7}$$

where, $U_{\rm ph}(r)$ is the energy density of photons in CSM (35):

$$U_{\rm ph}(r) = \frac{L_{\rm SN,pk}}{(4\pi c r_{\rm in}^2)} \left(\frac{r_{\rm in}}{r}\right)^2. \tag{A.8}$$

The SN peak luminosity $L_{\rm SN,pk}$ for different YSNe can be found in Sec. 3.4.2.

Bethe-Heitler energy loss time scale

The Bethe-Heitler energy loss time scale is

$$t_{\rm BH} = \tau_{\rm BH} \left(\frac{r}{r_{\rm in}}\right)^2 \tag{A.9}$$

where $\tau_{\rm BH}^{-1} = (\kappa_{\rm BH}\sigma_{\rm BH} c U_{\rm ph}(r_{\rm in}))/\varepsilon_{\rm av}$ and $\kappa_{\rm BH}\sigma_{\rm BH} \approx 6 \times 10^{-31}$ cm^2 (35).

Dominant energy loss processes

Fig. A.1 shows the time scales introduced above as functions of the proton energy for the dominant YSN classes: SNe IIn (top panel) and II-P (bottom panel), see Table 3.1. Since the CSM density and SN thermal photon density change with the shock radius, the acceleration timescale and different cooling timescales also change. Therefore, we show the evolution of these timescales for two different values of shock radius, i.e., $r = r_{\rm in}$ (left panel) and $r = 10r_{\rm in}$ (right panel). For both classes of SNe, the dominant energy loss processes are pp collisions and adiabatic losses for both shock radii. Note that photo-hadronic ($p\gamma$) interactions are not important here as the average energy of SN thermal photons is about 1 eV; the threshold energy of protons for this process is ~ 10 PeV and the SN flux of protons above this energy is very small. Moreover, the cross-section of $p\gamma$ interactions ($\sim 10^{-28}$ cm^2 (49)) is much smaller than that of pp interaction ($\sim 10^{-26}$ cm^2 (29)).

This page was intentionally left blank.

References

[1] T.K. Gaisser, R. Engel and E. Resconi, *Cosmic Rays and Particle Physics*, Cambridge University Press, 2 ed. (2016), 10.1017/CBO9781139192194.

[2] T.K. Gaisser, R.J. Protheroe and T. Stanev, *Gamma-ray production in supernova remnants*, *Astrophys. J.* **492** (1998) 219 [astro-ph/9609044].

[3] P. Bhattacharjee and G. Sigl, *Origin and propagation of extremely high-energy cosmic rays*, *Phys. Rept.* **327** (2000) 109 [astro-ph/9811011].

[4] B.D. Piazzoli, S.-M. Liu, D. della Volpe, Z. Cao, A. Chiavassa, B.D. Piazzoli et al., *Chapter 4 cosmic-ray physics *, Chinese Physics C* **46** (2022) 030004.

[5] PIERRE AUGER collaboration, *The energy spectrum of cosmic rays beyond the turn-down around* 10^{17} *eV as measured with the surface detector of the Pierre Auger Observatory*, *Eur. Phys. J. C* **81** (2021) 966 [2109.13400].

[6] HIRES collaboration, *Measurement of the flux of ultrahigh energy cosmic rays from monocular observations by the High Resolution Fly's Eye experiment*, *Phys. Rev. Lett.* **92** (2004) 151101 [astro-ph/0208243].

[7] N. Hayashida et al., *Updated AGASA event list above 4 x 10**19-eV*, astro-ph/0008102.

[8] K. Greisen, *End to the cosmic-ray spectrum?*, *Phys. Rev. Lett.* **16** (1966) 748.

[9] G.T. Zatsepin and V.A. Kuz'min, *Upper Limit of the Spectrum of Cosmic Rays*, *Soviet Journal of Experimental and Theoretical Physics Letters* **4** (1966) 78.

[10] G. Gelmini, O.E. Kalashev and D.V. Semikoz, *GZK photons as ultra high energy cosmic rays*, *J. Exp. Theor. Phys.* **106** (2008) 1061 [astro-ph/0506128].

[11] R.U. Abbasi, T. Abu-Zayyad, G. Archbold, R. Atkins, J. Bellido, K. Belov et al., *A study of the composition of ultra-high-energy cosmic rays using the high-resolution fly's eye*, *The Astrophysical Journal* **622** (2005) 910.

[12] B.R. Dawson, R. Meyhandan and K.M. Simpson, *Comparison of Fly's Eye and AGASA Mass Composition Measurements*, in *International Cosmic Ray Conference*, vol. 4 of *International Cosmic Ray Conference*, p. 25, Jan., 1997.

[13] PIERRE AUGER collaboration, *Combined fit of spectrum and composition data as measured by the Pierre Auger Observatory*, *JCAP* **04** (2017) 038 [1612.07155].

[14] PIERRE AUGER collaboration, *Inferences on mass composition and tests of hadronic interactions from 0.3 to 100 EeV using the water-Cherenkov detectors of the Pierre Auger Observatory*, *Phys. Rev. D* **96** (2017) 122003 [1710.07249].

[15] N. Arsene, *Mass Composition of UHECRs from Xmax Distributions Recorded by the Pierre Auger and Telescope Array Observatories*, *Universe* **7** (2021) 321 [2109.03626].

[16] A.V. Glushkov and A.V. Saburov, *Mass Composition of Cosmic Rays with Energies above 10^{17} eV According to the Data from the Muon Detectors of the Yakutsk EAS Array*, *JETP Lett.* **109** (2019) 559.

[17] AUGER collaboration, *Mass Composition of Cosmic Rays with Energies above $10^{17.2}$ eV from the Hybrid Data of the Pierre Auger Observatory*, *PoS* **ICRC2019** (2020) 482.

[18] P. Mészáros, D.B. Fox, C. Hanna and K. Murase, *Multi-Messenger Astrophysics*, *Nature Rev. Phys.* **1** (2019) 585 [1906.10212].

[19] A. Neronov, *Introduction to multi-messenger astronomy*, *Journal of Physics: Conference Series* **1263** (2019) 012001.

[20] M. Branchesi, *Multi-messenger astronomy: gravitational waves, neutrinos, photons, and cosmic rays*, *Journal of Physics: Conference Series* **718** (2016) 022004.

[21] ICECUBE, FERMI-LAT, MAGIC, AGILE, ASAS-SN, HAWC, H.E.S.S., INTEGRAL, KANATA, KISO, KAPTEYN, LIVERPOOL TELESCOPE, SUBARU, SWIFT NUSTAR, VERITAS, VLA/17B-403 collaboration, *Multimessenger observations of a flaring blazar coincident with high-energy neutrino IceCube-170922A*, *Science* **361** (2018) eaat1378 [1807.08816].

[22] Z. Cao, F.A. Aharonian, Q. An, L.X. Axikegu, Bai, Y.X. Bai, Y.W. Bao et al., *Ultrahigh-energy photons up to 1.4 petaelectronvolts from 12 γ-ray Galactic sources*, *nat* **594** (2021) 33.

[23] TIBET ASγ collaboration, *Potential PeVatron supernova remnant G106.3+2.7 seen in the highest-energy gamma rays*, *Nature Astron.* **5** (2021) 460 [2109.02898].

[24] CTA, "Cherenkov telescope array." Available at https://www.cta-observatory.org/science/ctao-performance/#1472563157332-1ef9e83d-426c.

[25] ICECUBE-GEN2 collaboration, *IceCube-Gen2: the window to the extreme Universe*, *J. Phys. G* **48** (2021) 060501 [2008.04323].

[26] *KM3NeT: Technical Design Report*, .

[27] GRAND collaboration, *The Giant Radio Array for Neutrino Detection (GRAND): Science and Design*, *Sci. China Phys. Mech. Astron.* **63** (2020) 219501 [1810.09994].

[28] Tibet ASγ Collaboration, M. Amenomori, Y.W. Bao, X.J. Bi, D. Chen, T.L. Chen et al., *Potential PeVatron supernova remnant G106.3+2.7 seen in the highest-energy gamma rays*, *Nature Astronomy* **5** (2021) 460 [2109.02898].

[29] S.R. Kelner, F.A. Aharonian and V.V. Bugayov, *Energy spectra of gamma-rays, electrons and neutrinos produced at proton-proton interactions in the very high energy regime*, *Phys. Rev. D* **74** (2006) 034018 [astro-ph/0606058].

[30] ICECUBE collaboration, *All-sky Search for Time-integrated Neutrino Emission from Astrophysical Sources with 7 yr of IceCube Data*, *Astrophys. J.* **835** (2017) 151 [1609.04981].

[31] ICECUBE collaboration, *Differential limit on the extremely-high-energy cosmic neutrino flux in the presence of astrophysical background from nine years of IceCube data*, *Phys. Rev. D* **98** (2018) 062003 [1807.01820].

[32] K. Murase, K. Kashiyama, K. Kiuchi and I. Bartos, *Gamma-Ray and Hard X-Ray Emission from Pulsar-Aided Supernovae as a Probe of Particle Acceleration in Embryonic Pulsar Wind Nebulae*, *Astrophys. J.* **805** (2015) 82 [1411.0619].

[33] K. Murase, *New Prospects for Detecting High-Energy Neutrinos from Nearby Supernovae*, *Phys. Rev. D* **97** (2018) 081301 [1705.04750].

[34] K. Murase, A. Franckowiak, K. Maeda, R. Margutti and J.F. Beacom, *High-Energy Emission from Interacting Supernovae: New Constraints on Cosmic-Ray Acceleration in Dense Circumstellar Environments*, *Astrophys. J.* **874** (2019) 80 [1807.01460].

[35] M. Petropoulou, A. Kamble and L. Sironi, *Radio synchrotron emission from secondary electrons in interaction-powered supernovae*, *Mon. Not. Roy. Astron. Soc.* **460** (2016) 44 [1603.00891].

[36] M. Petropoulou, S. Coenders, G. Vasilopoulos, A. Kamble and L. Sironi, *Point-source and diffuse high-energy neutrino emission from Type IIn supernovae*, *Mon. Not. Roy. Astron. Soc.* **470** (2017) 1881 [1705.06752].

[37] N. Smith, *Mass Loss: Its Effect on the Evolution and Fate of High-Mass Stars*, *Ann. Rev. Astron. Astrophys.* **52** (2014) 487 [1402.1237].

[38] E.O. Ofek et al., *SN 2010jl: Optical to Hard X-Ray Observations Reveal an Explosion Embedded in a Ten Solar Mass Cocoon*, *Astrophys. J.* **781** (2014) 42 [1307.2247].

[39] E.O. Ofek, L. Lin, C. Kouveliotou, G. Younes, E. Gogus, M.M. Kasliwal et al., *SN2009ip: Constraints on the progenitor mass-loss rate*, *Astrophys. J.* **768** (2013) 47 [1303.3894].

[40] E.O. Ofek et al., *Interaction-powered supernovae: Rise-time vs. peak-luminosity correlation and the shock-breakout velocity*, *Astrophys. J.* **788** (2014) 154 [1404.4085].

[41] S. Das and A. Ray, *Modeling type II-p/II-l supernovae interacting with recent episodic mass ejections from their presupernova stars with MESA and SNEC*, *Astrophys. J.* **851** (2017) 138.

[42] D. Brethauer, R. Margutti, D. Milisavljevic and M. Bietenholz, *Six Years of Luminous X-Ray Emission from the Strongly Interacting Ypye-Ib SN2014C Captured by Chandra and NuSTAR*, *Res. Notes AAS* **4** (2020) 235 [2012.04081].

[43] J.C. Mauerhan, W. Zheng, T. Brink, M.L. Graham, I. Shivvers, K. Clubb et al., *Stripped-envelope supernova SN 2004dk is now interacting with hydrogen-rich circumstellar material*, *Mon. Not. Roy. Astron. Soc.* **478** (2018) 5050 [1803.07051].

[44] N. Smith, *Interacting Supernovae: Types IIn and Ibn*, 1612.02006.

[45] P. Sarmah, S. Chakraborty, I. Tamborra and K. Auchettl, *High energy particles from young supernovae: gamma-ray and neutrino connections*, *JCAP* **08** (2022) 011 [2204.03663].

[46] Q. Yuan, N.-H. Liao, Y.-L. Xin, Y. Li, Y.-Z. Fan, B. Zhang et al., *Fermi Large Area Telescope detection of gamma-ray emission from the direction of supernova iPTF14hls*, *Astrophys. J. Lett.* **854** (2018) L18 [1712.01043].

[47] FERMI-LAT collaboration, *The spectrum of isotropic diffuse gamma-ray emission between 100 MeV and 820 GeV*, *Astrophys. J.* **799** (2015) 86 [1410.3696].

[48] ICECUBE collaboration, *The IceCube high-energy starting event sample: Description and flux characterization with 7.5 years of data*, *Phys. Rev. D* **104** (2021) 022002 [2011.03545].

[49] S.R. Kelner and F.A. Aharonian, *Energy spectra of gamma-rays, electrons and neutrinos produced at interactions of relativistic protons with low energy radiation*, *Phys. Rev. D* **78** (2008) 034013 [0803.0688].

[50] S. Das, K. Murase and T. Fujii, *Revisiting ultrahigh-energy constraints on decaying superheavy dark matter*, *Phys. Rev. D* **107** (2023) 103013 [2302.02993].

[51] ARA collaboration, *Performance of two Askaryan Radio Array stations and first results in the search for ultrahigh energy neutrinos*, *Phys. Rev. D* **93** (2016) 082003 [1507.08991].

[52] PIERRE AUGER collaboration, *Upper limit on the cosmic-ray photon flux above 10^{19} eV using the surface detector of the Pierre Auger Observatory*, *Astropart. Phys.* **29** (2008) 243 [0712.1147].

[53] TELESCOPE ARRAY collaboration, *Highlights from the Telescope Array Experiments*, in *21st International Symposium on Very High Energy Cosmic Ray Interactions*, 9, 2022 [2209.03591].

[54] J. Casaus, *The AMS-02 experiment on the ISS*, in *Journal of Physics Conference Series*, vol. 171 of *Journal of Physics Conference Series*, p. 012045, June, 2009, DOI.

[55] W. Hanlon, "William hanlon's web page, updated cosmic ray spectrum." https://web.physics.utah.edu/~whanlon/.

[56] E. Fermi, *On the origin of the cosmic radiation*, *Phys. Rev.* **75** (1949) 1169.

[57] W.I. Axford, E. Leer and G. Skadron, *The Acceleration of Cosmic Rays by Shock Waves*, in *International Cosmic Ray Conference*, vol. 11 of *International Cosmic Ray Conference*, p. 132, Jan., 1977.

[58] G.F. Krymskii, *A regular mechanism for the acceleration of charged particles on the front of a shock wave*, *Akademiia Nauk SSSR Doklady* **234** (1977) 1306.

[59] A.R. Bell, *The acceleration of cosmic rays in shock fronts – II*, *Monthly Notices of the Royal Astronomical Society* **182** (1978) 443 [https://academic.oup.com/mnras/article-pdf/182/3/443/3856040/mnras182-0443.pdf].

[60] R.D. Blandford and J.P. Ostriker, *Particle acceleration by astrophysical shocks.*, *apjl* **221** (1978) L29.

[61] M.A. Malkov and L.O. Drury, *Nonlinear theory of diffusive acceleration of particles by shock waves*, *Reports on Progress in Physics* **64** (2001) 429.

[62] R. Blandford and D. Eichler, *Particle acceleration at astrophysical shocks: A theory of cosmic ray origin*, *physrep* **154** (1987) 1.

[63] A.M. Hillas, *The Origin of Ultra-High-Energy Cosmic Rays*, *araa* **22** (1984) 425.

[64] S. Chakraborty, P. Mehta and P. Sarmah, *A relook at the GZK Neutrino-Photon Connection: Impact of Extra-galactic Radio Background & UHECR properties*, 2307.15667.

[65] G.B. Gelmini, O. Kalashev and D. Semikoz, *Upper Limit on the Diffuse Radio Background from GZK Photon Observation*, *Universe* **8** (2022) 402 [2206.00408].

[66] C. Giunti and C.W. Kim, *Fundamentals of Neutrino Physics and Astrophysics*, Oxford University Press (03, 2007), 10.1093/acprof:oso/9780198508717.001.0001.

[67] A.Y. Smirnov, *The MSW effect and solar neutrinos*, in *10th International Workshop on Neutrino Telescopes*, pp. 23–43, 5, 2003 [hep-ph/0305106].

[68] M. Ahlers and K. Murase, *Probing the Galactic origin of the IceCube excess with gamma rays*, *prd* **90** (2014) 023010 [1309.4077].

[69] ICECUBE collaboration, *Flavor Ratio of Astrophysical Neutrinos above 35 TeV in IceCube*, *Phys. Rev. Lett.* **114** (2015) 171102 [1502.03376].

[70] P. Meszaros, *Astrophysical Sources of High Energy Neutrinos in the IceCube Era*, *Ann. Rev. Nucl. Part. Sci.* **67** (2017) 45 [1708.03577].

[71] D. Guetta, *Neutrinos from Gamma Ray Bursts in the IceCube and ARA Era*, *JHEAp* **7** (2015) 90 [1503.07146].

[72] M. Bustamante, J.F. Beacom and K. Murase, *Testing decay of astrophysical neutrinos with incomplete information*, *Phys. Rev. D* **95** (2017) 063013 [1610.02096].

[73] KM3NET collaboration, *Sensitivity of the KM3NeT/ARCA neutrino telescope to point-like neutrino sources*, *Astropart. Phys.* **111** (2019) 100 [1810.08499].

[74] FERMI-LAT collaboration, *The Spectrum of the Isotropic Diffuse Gamma-Ray Emission Derived From First-Year Fermi Large Area Telescope Data*, *Phys. Rev. Lett.* **104** (2010) 101101 [1002.3603].

[75] FERMI-LAT collaboration, *The Fermi-LAT high-latitude Survey: Source Count Distributions and the Origin of the Extragalactic Diffuse Background*, *Astrophys. J.* **720** (2010) 435 [1003.0895].

[76] FERMI-LAT collaboration, *GeV Observations of Star-forming Galaxies with \textitFermi LAT*, *Astrophys. J.* **755** (2012) 164 [1206.1346].

[77] FERMI-LAT collaboration, *Resolving the Extragalactic γ-Ray Background above 50 GeV with the Fermi Large Area Telescope*, *Phys. Rev. Lett.* **116** (2016) 151105 [1511.00693].

[78] FERMI-LAT, ASAS-SN, ICECUBE collaboration, *Investigation of two Fermi-LAT gamma-ray blazars coincident with high-energy neutrinos detected by IceCube*, *Astrophys. J.* **880** (2019) 880:103 [1901.10806].

[79] PIERRE AUGER collaboration, *Constraining models for the origin of ultra-high-energy cosmic rays with a novel combined analysis of arrival directions, spectrum, and composition data measured at the Pierre Auger Observatory*, 2305.16693.

[80] T.K. Gaisser, T. Stanev and S. Tilav, *Cosmic ray energy spectrum from measurements of air showers*, *Frontiers of Physics* **8** (2013) 748 [1303.3565].

[81] A.R. Bell, *Turbulent amplification of magnetic field and diffusive shock acceleration of cosmic rays*, *mnras* **353** (2004) 550.

[82] S.P. Reynolds, *Supernova remnants at high energy.*, *araa* **46** (2008) 89.

[83] D. Gaggero, F. Zandanel, P. Cristofari and S. Gabici, *Time evolution of gamma rays from supernova remnants*, *mnras* **475** (2018) 5237 [1710.05038].

[84] S. Gabici, C. Evoli, D. Gaggero, P. Lipari, P. Mertsch, E. Orlando et al., *The origin of Galactic cosmic rays: Challenges to the standard paradigm*, *International Journal of Modern Physics D* **28** (2019) 1930022 [1903.11584].

[85] P. Cristofari, *The Hunt for Pevatrons: The Case of Supernova Remnants*, *Universe* **7** (2021) 324 [2110.07956].

[86] T. Montmerle, *On gamma-ray sources, supernova remnants, OB associations, and the origin of cosmic rays.*, *apj* **231** (1979) 95.

[87] S. Gabici and F.A. Aharonian, *Searching for Galactic Cosmic-Ray Pevatrons with Multi-TeV Gamma Rays and Neutrinos*, *apjl* **665** (2007) L131 [0705.3011].

[88] F. Aharonian, R. Yang and E. de Oña Wilhelmi, *Massive stars as major factories of Galactic cosmic rays*, *Nature Astronomy* **3** (2019) 561 [1804.02331].

[89] M. Ackermann, M. Ajello, A. Allafort, L. Baldini, J. Ballet, G. Barbiellini et al., *Detection of the Characteristic Pion-Decay Signature in Supernova Remnants*, *Science* **339** (2013) 807 [1302.3307].

[90] HESS Collaboration, A. Abramowski, F. Aharonian, F.A. Benkhali, A.G. Akhperjanian, E.O. Angüner et al., *Acceleration of petaelectronvolt protons in the Galactic Centre*, *nat* **531** (2016) 476 [1603.07730].

[91] Lhaaso Collaboration, Z. Cao, F. Aharonian, Q. An, Axikegu, L.X. Bai et al., *Peta-electron volt gamma-ray emission from the Crab Nebula*, *Science* **373** (2021) 425 [2111.06545].

[92] R.-Y. Liu and X.-Y. Wang, *PeV Emission of the Crab Nebula: Constraints on the Proton Content in Pulsar Wind and Implications*, *apj* **922** (2021) 221 [2109.14148].

[93] Q.-Y. Peng, B.-W. Bao, F.-W. Lu and L. Zhang, *Multiband Emission up to PeV Energy from the Crab Nebula in a Spatially Dependent Lepto-hadronic Model*, *apj* **926** (2022) 7 [2112.14939].

[94] Q. An, R. Asfandiyarov, P. Azzarello, P. Bernardini, X.J. Bi, M.S. Cai et al., *Measurement of the cosmic ray proton spectrum from 40 GeV to 100 TeV with the DAMPE satellite*, *Science Advances* **5** (2019) eaax3793 [1909.12860].

[95] Z.-Q. Huang, R.-Y. Liu, J.C. Joshi and X.-Y. Wang, *Examining the Secondary Product Origin of Cosmic-Ray Positrons with the Latest AMS-02 Data*, *apj* **895** (2020) 53 [2001.02973].

[96] Y. Fujita, Y. Ohira, S.J. Tanaka and F. Takahara, *Molecular Clouds as a Probe of Cosmic-Ray Acceleration in a Supernova Remnant*, *apjl* **707** (2009) L179 [0911.4482].

[97] N. Gupta, *Galactic PeV neutrinos*, *Astroparticle Physics* **48** (2013) 75 [1305.4123].

[98] S. Celli, F. Aharonian and S. Gabici, *Spectral Signatures of PeVatrons*, *apj* **903** (2020) 61 [2009.05999].

[99] A. Kar and N. Gupta, *Ultrahigh-energy γ-Rays from Past Explosions in Our Galaxy*, *apj* **926** (2022) 110 [2112.08757].

[100] A. De Sarkar and N. Gupta, *Exploring the Hadronic Origin of LHAASO J1908+0621*, *apj* **934** (2022) 118 [2205.01923].

[101] T. Sudoh and J.F. Beacom, *Where are Milky Way's Hadronic PeVatrons?*, *arXiv e-prints* (2022) arXiv:2209.03970 [2209.03970].

[102] M. Mandelartz and J. Becker Tjus, *Prediction of the diffuse neutrino flux from cosmic ray interactions near supernova remnants*, *Astroparticle Physics* **65** (2015) 80 [1301.2437].

[103] R. Abbasi, M. Ackermann, J. Adams, J.A. Aguilar, M. Ahlers, M. Ahrens et al., *IceCube high-energy starting event sample: Description and flux characterization with 7.5 years of data*, *prd* **104** (2021) 022002 [2011.03545].

[104] S. Chakraborty and I. Izaguirre, *Diffuse neutrinos from extragalactic supernova remnants: Dominating the 100 TeV IceCube flux*, *Phys. Lett. B* **745** (2015) 35 [1501.02615].

[105] S. Razzaque, *Galactic Center origin of a subset of IceCube neutrino events*, *prd* **88** (2013) 081302 [1309.2756].

[106] A. Neronov, D. Semikoz and C. Tchernin, *PeV neutrinos from interactions of cosmic rays with the interstellar medium in the Galaxy*, *prd* **89** (2014) 103002 [1307.2158].

[107] E. Kafexhiu, F. Aharonian, A.M. Taylor and G.S. Vila, *Parametrization of gamma-ray production cross sections for p p interactions in a broad proton energy range from the kinematic threshold to PeV energies*, *prd* **90** (2014) 123014 [1406.7369].

[108] I.V. Moskalenko, T.A. Porter and A.W. Strong, *Attenuation of vhe gamma rays by the milky way interstellar radiation field*, *Astrophys. J. Lett.* **640** (2006) L155 [astro-ph/0511149].

[109] C. Ge, R.-Y. Liu, S. Niu, Y. Chen and X.-Y. Wang, *Revealing a peculiar supernova remnant G106.3+2.7 as a petaelectronvolt proton accelerator with X-ray observations*, *The Innovation* **2** (2021) 100118 [2012.11531].

[110] R. Kothes, B. Uyaniker and S. Pineault, *The Supernova Remnant G106.3+2.7 and Its Pulsar-Wind Nebula: Relics of Triggered Star Formation in a Complex Environment*, *apj* **560** (2001) 236 [astro-ph/0106270].

[111] Y. Bao and Y. Chen, *On the Hard Gamma-Ray Spectrum of the Potential PeVatron Supernova Remnant G106.3 + 2.7*, *apj* **919** (2021) 32 [2103.01814].

[112] C. Yang, H. Zeng, B. Bao and L. Zhang, *Possible hadronic origin of TeV photon emission from SNR G106.3+2.7*, *aap* **658** (2022) A60 [2106.02629].

[113] Y. Fujita, A. Bamba, K.K. Nobukawa and H. Matsumoto, *X-Ray Emission from the PeVatron-candidate Supernova Remnant G106.3+2.7*, *apj* **912** (2021) 133 [2101.10329].

[114] Y. Xin, H. Zeng, S. Liu, Y. Fan and D. Wei, *VER J2227+608: A Hadronic PeVatron Pulsar Wind Nebula?*, *apj* **885** (2019) 162 [1907.04972].

[115] V.A. Acciari, E. Aliu, T. Arlen, T. Aune, M. Bautista, M. Beilicke et al., *Detection of Extended VHE Gamma Ray Emission from G106.3+2.7 with Veritas*, *apjl* **703** (2009) L6 [0911.4695].

[116] M.A. Malkov, *Asymptotic Particle Spectra and Plasma Flows at Strong Shocks*, *apjl* **511** (1999) L53 [astro-ph/9807097].

[117] A.A. Abdo, B. Allen, D. Berley, S. Casanova, C. Chen, D.G. Coyne et al., *TeV Gamma-Ray Sources from a Survey of the Galactic Plane with Milagro*, *apjl* **664** (2007) L91 [0705.0707].

[118] F. Aharonian, A.G. Akhperjanian, G. Anton, U. Barres de Almeida, A.R. Bazer-Bachi, Y. Becherini et al., *Detection of very high energy radiation from HESS J1908+063 confirms the Milagro unidentified source MGRO J1908+06*, *aap* **499** (2009) 723 [0904.3409].

[119] HAWC Collaboration collaboration, *Multiple galactic sources with emission above 56 tev detected by hawc*, *Phys. Rev. Lett.* **124** (2020) 021102.

[120] J. Yang, J.-L. Zhang, Z.-Y. Cai, D.-R. Lu and Y.-H. Tan, *Molecular Gas Distribution around the Supernova Remnant G40.5 0.5*, *cjaa* **6** (2006) 210.

[121] A.J.B. Downes, T. Pauls and C.J. Salter, *G 40.5-0.5 : A previously unrecognised supernova remnant in Aql.*, *aap* **92** (1980) 47.

[122] J. Li, R.-Y. Liu, E. de Oña Wilhelmi, D.F. Torres, Q.-C. Liu, M. Kerr et al., *Investigating the Nature of MGRO J1908+06 with Multiwavelength Observations*, *apjl* **913** (2021) L33 [2102.05615].

[123] S. Abdollahi, F. Acero, M. Ackermann, M. Ajello, W.B. Atwood, M. Axelsson et al., *Fermi Large Area Telescope Fourth Source Catalog*, *apjs* **247** (2020) 33 [1902.10045].

[124] H. E. S. S. Collaboration, H. Abdalla, A. Abramowski, F. Aharonian, F. Ait Benkhali, E.O. Angüner et al., *The H.E.S.S. Galactic plane survey*, *aap* **612** (2018) A1 [1804.02432].

[125] Fermi-LAT, "Official website." Available at https://fermi.gsfc.nasa.gov.

[126] S. Vernetto and for the LHAASO Collaboration, *Gamma ray astronomy with lhaaso*, *Journal of Physics: Conference Series* **718** (2016) 052043.

[127] A. Tibet, "The Tibet ASg Experiment." Available at icrr.u-tokyo.ac.jp/prwps/extreview/2013/pdf/16_04_Tibet_AS-Gamma.pdf.

[128] IceCube Collaboration, R. Abbasi, M. Ackermann, J. Adams, J.A. Aguilar, M. Ahlers et al., *IceCube Data for Neutrino Point-Source Searches Years 2008-2018*, *arXiv e-prints* (2021) arXiv:2101.09836 [2101.09836].

[129] P. Blasi, *A semi-analytical approach to non-linear shock acceleration*, *Astroparticle Physics* **16** (2002) 429 [astro-ph/0104064].

[130] M.G. Aartsen, K. Abraham, M. Ackermann, J. Adams, J.A. Aguilar, M. Ahlers et al., *All-sky search for time-integrated neutrino emission from astrophysical sources with 7 yr of IceCube data*, *The Astrophysical Journal* **835** (2017) 151.

[131] R. Abbasi, M. Ackermann, J. Adams, N. Aggarwal, J.A. Aguilar, M. Ahlers et al., *Searches for Neutrinos from Large High Altitude Air Shower Observatory Ultra-high-energy γ-Ray Sources Using the IceCube Neutrino Observatory*, *apjl* **945** (2023) L8 [2211.14184].

[132] L.O. Drury, *REVIEW ARTICLE: An introduction to the theory of diffusive shock acceleration of energetic particles in tenuous plasmas*, *Reports on Progress in Physics* **46** (1983) 973.

[133] M.A. Malkov, *Asymptotic Particle Spectra and Plasma Flows at Strong Shocks*, *apjl* **511** (1999) L53 [astro-ph/9807097].

[134] D.F. Torres, A. Cillis, J. Martín and E. de Oña Wilhelmi, *Time-dependent modeling of TeV-detected, young pulsar wind nebulae*, *Journal of High Energy Astrophysics* **1** (2014) 31 [1402.5485].

[135] H. Yu, K. Wu, L. Wen and J. Fang, *A leptonic model for the γ-rays coincident with the tail region of the supernova remnant G106.3+2.7*, *na* **90** (2022) 101669.

[136] J.C. Joshi, S.J. Tanaka, L.S. Miranda and S. Razzaque, *Study of maximum electron energy of sub-PeV pulsar wind nebulae by multiwavelength modelling*, *arXiv e-prints* (2022) arXiv:2205.00521 [2205.00521].

[137] R. Margutti et al., *A panchromatic view of the restless SN2009ip reveals the explosive ejection of a massive star envelope*, *Astrophys. J.* **780** (2014) 21 [1306.0038].

[138] R.M. Humphreys and K. Davidson, *The Luminous Blue Variables: Astrophysical Geysers*, *Publ. Astron. Soc. Pac.* **106** (1989) 1025.

[139] N. Smith, *Luminous blue variables and the fates of very massive stars*, *Philosophical Transactions of the Royal Society A: Mathematical, Physical and Engineering Sciences* **375** (2017) 20160268 [https://royalsocietypublishing.org/doi/pdf/10.1098/rsta.2016.0268].

[140] K. Weis and D.J. Bomans, *Luminous Blue Variables*, *Galaxies* **8** (2020) 20 [2009.03144].

[141] J.H. Groh, G. Meynet and S. Ekstrom, *Massive star evolution: Luminous Blue Variables as unexpected Supernova progenitors*, *Astron. Astrophys.* **550** (2013) L7 [1301.1519].

[142] S. Ustamujic et al., *Modeling the remnants of core-collapse supernovae from luminous blue variable stars*, *Astron. Astrophys.* **654** (2021) A167 [2108.01951].

[143] W. Jacobson-Galán et al., *Final Moments. I. Precursor Emission, Envelope Inflation, and Enhanced Mass Loss Preceding the Luminous Type II Supernova 2020tlf*, *Astrophys. J.* **924** (2022) 15 [2109.12136].

[144] G. Terreran et al., *The Early Phases of Supernova 2020pni: Shock Ionization of the Nitrogen-enriched Circumstellar Material*, *Astrophys. J.* **926** (2022) 20 [2105.12296].

[145] YOUNG SUPERNOVA EXPERIMENT collaboration, *An Early-time Optical and Ultraviolet Excess in the Type-Ic SN 2020oi*, *Astrophys. J.* **924** (2022) 55 [2105.09963].

[146] A. Marcowith, V.V. Dwarkadas, M. Renaud, V. Tatischeff and G. Giacinti, *Core-collapse supernovae as cosmic ray sources*, *Mon. Not. R. Astron. Soc.* **479** (2018) 4470 [1806.09700].

[147] A. Marcowith, M. Renaud, V. Dwarkadas and V. Tatischeff, *Cosmic-ray acceleration and gamma-ray signals from radio supernovæ*, *Nuc. Phys. B Proc. Suppl.* **256** (2014) 94 [1409.3670].

[148] P. Cristofari, A. Marcowith, M. Renaud, V.V. Dwarkadas, V. Tatischeff, G. Giacinti et al., *The first days of Type II-P core collapse supernovae in the gamma-ray range*, *Mon. Not. R. Astron. Soc.* **511** (2022) 3321 [2201.09583].

[149] R.J. Foley, N. Smith, M. Ganeshalingam, W. Li, R. Chornock and A.V. Filippenko, *SN 2006jc: A Wolf-Rayet Star Exploding in a Dense He-rich Circumstellar Medium*, *Astrophys. J. Lett.* **657** (2007) L105 [astro-ph/0612711].

[150] K. Wang, T.-Q. Huang and Z. Li, *Transient High-energy Gamma-Rays and Neutrinos from Nearby Type II Supernovae*, *Astrophys. J.* **872** (2019) 157 [1901.05598].

[151] K. Murase, T.A. Thompson, B.C. Lacki and J.F. Beacom, *New class of high-energy transients from crashes of supernova ejecta with massive circumstellar material shells*, *Phys. Rev. D* **84** (2011) 043003 [1012.2834].

[152] K. Murase, T.A. Thompson and E.O. Ofek, *Probing cosmic ray ion acceleration with radio-submm and gamma-ray emission from interaction-powered supernovae*, *Mon. Not. R. Astron. Soc.* **440** (2014) 2528 [1311.6778].

[153] K. Murase, M. Ahlers and B.C. Lacki, *Testing the hadronuclear origin of PeV neutrinos observed with IceCube*, *Phys. Rev. D* **88** (2013) 121301 [1306.3417].

[154] P. Sarmah, S. Chakraborty and J.C. Joshi, *Probing LHAASO galactic PeVatrons through gamma-ray and neutrino correspondence*, *Mon. Not. R. Astron. Soc.* **521** (2023) 1144 [2301.04161].

[155] A. Kheirandish and K. Murase, *Detecting High-Energy Neutrino Minibursts from Local Supernovae with Multiple Neutrino Observatories*, 2204.08518.

[156] P. Chandra, *Circumstellar interaction in supernovae in dense environments - an observational perspective*, *Space Sci. Rev.* **214** (2018) 27 [1712.07405].

[157] S.J. Sturner, J.G. Skibo, C.D. Dermer and J.R. Mattox, *Temporal evolution of nonthermal spectra from supernova remnants*, *Astrophys. J.* **490** (1997) 619.

[158] P. Chandra, C.J. Stockdale, R.A. Chevalier, S.D. Van Dyk, A. Ray, M.T. Kelley et al., *Eleven years of radio monitoring of the Type IIn supernova SN 1995N*, *Astrophys. J.* **690** (2009) 1839 [0809.2810].

[159] R.A. Chevalier and C. Fransson, *Supernova interaction with a circumstellar medium*, *Lect. Notes Phys.* **598** (2003) 171 [astro-ph/0110060].

[160] M.A. Roth, M.R. Krumholz, R.M. Crocker and S. Celli, *The diffuse γ-ray background is dominated by star-forming galaxies*, *Nature* **597** (2021) 341 [2109.07598].

[161] S. Chakraborty and I. Izaguirre, *Star-forming galaxies as the origin of IceCube neutrinos: Reconciliation with Fermi-LAT gamma rays*, 1607.03361.

[162] I. Tamborra and K. Murase, *Neutrinos from Supernovae*, *Space Sci. Rev.* **214** (2018) 31.

[163] Fermi-LAT, *https://fermi.gsfc.nasa.gov/ssc/data/analysis/documentation/Cicerone/Cicerone_LAT_IRFs/LAT_sensitivity.html*, .

[164] M. Actis, G. Agnetta, F. Aharonian, A. Akhperjanian, J. Aleksić, E. Aliu et al., *Design concepts for the Cherenkov Telescope Array CTA: an advanced facility for ground-based high-energy gamma-ray astronomy*, *Experimental Astronomy* **32** (2011) 193 [1008.3703].

[165] F.W. Stecker, S.T. Scully and M.A. Malkan, *An Empirical Determination of the Intergalactic Background Light from UV to FIR Wavelengths Using FIR Deep Galaxy Surveys and the Gamma-ray Opacity of the Universe*, *Astrophys. J.* **827** (2016) 6 [1605.01382].

[166] F.W. Stecker and T.M. Venters, *Components of the Extragalactic Gamma Ray Background*, *Astrophys. J.* **736** (2011) 40 [1012.3678].

[167] O.D. Fox et al., *On the Nature of Type Ia-CSM Supernovae: Optical and Near-Infrared Spectra of SN 2012ca and SN 2013dn*, *Mon. Not. Roy. Astron. Soc.* **447** (2015) 776 [1408.6239].

[168] S.J. Sturner, J.G. Skibo, C.D. Dermer and J.R. Mattox, *Temporal Evolution of Nonthermal Spectra from Supernova Remnants*, *Astrophys. J.* **490** (1997) 619.

[169] A.R. Bell, *Particle acceleration by shocks in supernova remnants*, *Braz. J. Phys.* **44** (2014) 415 [1311.5779].

[170] R.A. Chevalier, *Self-similar solutions for the interaction of stellar ejecta with an external medium.*, *Astrophys. J.* **258** (1982) 790.

[171] A. Mastichiadis, *On the high-energy nonthermal emission from shell type supernova remnants*, *Astron. Astrophys.* **305** (1996) L53 [astro-ph/9601132].

[172] E. Waxman and B. Katz, *Shock breakout theory*, in *Handbook of Supernovae*, A.W. Alsabti and P. Murdin, eds., (Cham), pp. 967–1015, Springer International Publishing (2017), DOI.

[173] D. Caprioli and A. Spitkovsky, *Simulations of ion acceleration at non-relativistic shocks. i. acceleration efficiency*, *Astrophys. J.* **783** (2014) 91.

[174] R.J. Protheroe and R.W. Clay, *Ultrahigh energy cosmic rays*, *Publ. Astron. Soc. Pac.* **21** (2004) 1 [astro-ph/0311466].

[175] T. Piran, *The physics of gamma-ray bursts*, *Rev. Mod. Phys.* **76** (2005) 1143.

[176] P. Meszaros, *Gamma-Ray Bursts*, *Rept. Prog. Phys.* **69** (2006) 2259 [astro-ph/0605208].

[177] A. Marcowith, V. Dwarkadas, M. Renaud, V. Tatischeff and G. Giacinti, *Core collapse supernovae as Cosmic Ray sources*, *Mon. Not. Roy. Astron. Soc.* **479** (2018) 4470 [1806.09700].

[178] S.R. Kelner, F.A. Aharonian and V.V. Bugayov, *Energy spectra of gamma rays, electrons, and neutrinos produced at proton-proton interactions in the very high energy regime*, *prd* **74** (2006) 034018 [astro-ph/0606058].

[179] A. Mastichiadis and J.G. Kirk, *Self-consistent particle acceleration in active galactic nuclei*, astro-ph/9408077.

[180] J.D. Finke and C.D. Dermer, *Cosmic-Ray Electron Evolution in the Supernova Remnant RX J1713.7-3946*, *Astrophys. J.* **751** (2012) 65 [1203.4242].

[181] F.W. Stecker, M.A. Malkan and S.T. Scully, *Intergalactic photon spectra from the far ir to the uv lyman limit for $0 < Z < 6$ and the optical depth of the universe to high energy gamma-rays*, *Astrophys. J.* **648** (2006) 774 [astro-ph/0510449].

[182] J.M. Jauch and F. Rohrlich, *The theory of photons and electrons. The relativistic quantum field theory of charged particles with spin one-half*, Texts and Monographs in Physics, Springer, Berlin, 2nd ed. ed. (1976), 10.1007/978-3-642-80951-4.

[183] X.-C. Chang and X.-Y. Wang, *The diffuse gamma-ray flux associated with sub-PeV/PeV neutrinos from starburst galaxies*, *Astrophys. J.* **793** (2014) 131 [1406.1099].

[184] L.A. Anchordoqui et al., *Cosmic Neutrino Pevatrons: A Brand New Pathway to Astronomy, Astrophysics, and Particle Physics*, *JHEAp* **1-2** (2014) 1 [1312.6587].

[185] N. Smith et al., *Endurance of SN 2005ip after a decade: X-rays, radio and Hα like SN 1988Z require long-lived pre-supernova mass-loss*, *Mon. Not. Roy. Astron. Soc.* **466** (2017) 3021 [1612.02011].

[186] D. Pooley, J.C. Wheeler, J. Vinkó, V.V. Dwarkadas, T. Szalai, J.M. Silverman et al., *Interaction of SN~Ib 2004dk with a Previously-Expelled Envelope*, *Astrophys. J.* **833** (2019) 120 [1910.06395].

[187] P. Chandra, R.A. Chevalier, N. Chugai, D. Milisavljevic and C. Fransson, *Supernova Interaction with a Dense Detached Shell in SN 2001em*, *Astrophys. J.* **902** (2020) 55 [2008.13724].

[188] A. Balasubramanian, A. Corsi, E. Polisensky, T.E. Clarke and N.E. Kassim, *Radio Observations of SN2004dk with VLITE Confirm Late-time Rebrightening*, *Astrophys. J.* **923** (2021) 32 [2101.07348].

[189] T. Szalai et al., *Spitzer's Last Look at Extragalactic Explosions: Long-term Evolution of Interacting Supernovae*, *Astrophys. J.* **919** (2021) 17 [2106.12427].

[190] L. DeMarchi et al., *Radio Analysis of SN 2004C Reveals an Unusual CSM Density Profile as a Harbinger of Core Collapse*, 2203.07388.

[191] A. Gal-Yam, *Observational and Physical Classification of Supernovae*, in *Handbook of Supernovae*, A.W. Alsabti and P. Murdin, eds., p. 195 (2017), DOI.

[192] M. Turatto, *Classification of supernovae*, *Lect. Notes Phys.* **598** (2003) 21 [astro-ph/0301107].

[193] T.J. Moriya, K. Maeda, F. Taddia, J. Sollerman, S.I. Blinnikov and E.I. Sorokina, *Mass-loss histories of Type IIn supernova progenitors within decades before their explosion*, *Mon. Not. Roy. Astron. Soc.* **439** (2014) 2917 [1401.4893].

[194] F. Taddia et al., *Carnegie Supernova Project: Observations of Type IIn supernovae*, *Astron. Astrophys.* **555** (2013) A10 [1304.3038].

[195] C.L. Ransome, S.M. Habergham-Mawson, M.J. Darnley, P.A. James, A.V. Filippenko and E.M. Schlegel, *A systematic reclassification of Type IIn supernovae*, *Mon. Not. Roy. Astron. Soc.* **506** (2021) 4715 [2107.02179].

[196] V.V. Dwarkadas, *On luminous blue variables as the progenitors of core-collapse supernovae, especially Type IIn supernovae*, *Mon. Not. Roy. Astron. Soc.* **412** (2011) 1639 [1011.3484].

[197] R.A. Chevalier and Z.-Y. Li, *Wind interaction models for gamma-ray burst afterglows: The Case for two types of progenitors*, *Astrophys. J.* **536** (2000) 195 [astro-ph/9908272].

[198] V. Morozova, A.L. Piro and S. Valenti, *Unifying Type II Supernova Light Curves with Dense Circumstellar Material*, *Astrophys. J.* **838** (2017) 28 [1610.08054].

[199] V. Morozova, A.L. Piro, M. Renzo and C.D. Ott, *Numerical Modeling of the Early Light Curves of Type IIP Supernovae*, *Astrophys. J.* **829** (2016) 109 [1603.08530].

[200] S. Ekström, C. Georgy, P. Eggenberger, G. Meynet, N. Mowlavi, A. Wyttenbach et al., *Grids of stellar models with rotation. I. Models from 0.8 to 120 $M_{\odot}$ at solar metallicity (Z = 0.014)*, *aap* **537** (2012) A146 [1110.5049].

[201] S.J. Smartt, *Observational constraints on the progenitors of core-collapse supernovae : the case for missing high mass stars*, *Publ. Astron. Soc. Austral.* **32** (2015) e016 [1504.02635].

[202] A. Heger, C.L. Fryer, S.E. Woosley, N. Langer and D.H. Hartmann, *How massive single stars end their life*, *Astrophys. J.* **591** (2003) 288 [astro-ph/0212469].

[203] G.A. Wagle and A. Ray, *Type IIP Supernova Progenitors. II. Stellar Mass and Obscuration by the Dust in the Circumstellar Medium*, *Astrophys. J.* **889** (2020) 86 [1911.12831].

[204] T. Nakaoka et al., *The Low-luminosity Type IIP Supernova 2016bkv with Early-phase Circumstellar Interaction*, *Astrophys. J.* **859** (2018) 78 [1804.06065].

[205] O. Yaron et al., *Confined Dense Circumstellar Material Surrounding a Regular Type II Supernova: The Unique Flash-Spectroscopy Event of SN 2013fs*, *Nature Phys.* **13** (2017) 510 [1701.02596].

[206] C. Bullivant et al., *SN 2013fs and SN 2013fr: exploring the circumstellar-material diversity in Type II supernovae*, *Mon. Not. Roy. Astron. Soc.* **476** (2018) 1497 [1801.01532].

[207] R. Margutti et al., *Ejection of the Massive Hydrogen-rich Envelope Time with the Collapse of the Stripped SN 2014C*, *Astrophys. J.* **835** (2017) 140 [1601.06806].

[208] T.J. Moriya, F. Förster, S.-C. Yoon, G. Gräfener and S.I. Blinnikov, *Type IIP supernova light curves affected by the acceleration of red supergiant winds*, *Mon. Not. Roy. Astron. Soc.* **476** (2018) 2840 [1802.07752].

[209] F. Förster et al., *The delay of shock breakout due to circumstellar material evident in most type II supernovae*, *Nature Astron.* **2** (2018) 808 [1809.06379].

[210] N. Sravan, P. Marchant, V. Kalogera, D. Milisavljevic and R. Margutti, *Progenitors of Type IIb Supernovae: II. Observable Properties*, *Astrophys. J.* **903** (2020) 70 [2009.06405].

[211] R. Ouchi and K. Maeda, *Radii and Mass-loss Rates of Type IIb Supernova Progenitors*, *Astrophys. J.* **840** (2017) 90 [1705.02430].

[212] K.A. Bostroem et al., *Signatures of Circumstellar Interaction in the Type IIL Supernova ASASSN-15oz*, *Mon. Not. Roy. Astron. Soc.* **485** (2019) 5120 [1901.09962].

[213] T.M. Reynolds et al., *SN 2016gsd: An unusually luminous and linear type II supernova with high velocities*, *Mon. Not. Roy. Astron. Soc.* **493** (2020) 1761 [1909.13617].

[214] A. Kamble, R. Margutti, A.M. Soderberg, S. Chakraborti, C. Fransson, R. Chevalier et al., *Radio and X-rays From SN 2013df Enlighten Progenitors of Type IIb Supernovae*, 1504.07988.

[215] A. Gilkis and I. Arcavi, *How much hydrogen is in Type Ib and IIb supernova progenitors?*, *Mon. Not. Roy. Astron. Soc.* **511** (2022) 691 [2111.04432].

[216] M.-K. Jung, S.-C. Yoon and H.-J. Kim, *Effects of Winds on the Optical Properties of Type Ib and Ic Supernova Progenitors*, *Astrophys. J.* **925** (2022) 216 [2112.00272].

[217] S. Tinyanont et al., *Supernova 2014C: ongoing interaction with extended circumstellar material with silicate dust*, *Astrophys. J.* **887** (2019) 75 [1909.06403].

[218] C.D. Kilpatrick et al., *A cool and inflated progenitor candidate for the Type Ib supernova 2019yvr at 2.6 yr before explosion*, *Mon. Not. Roy. Astron. Soc.* **504** (2021) 2073 [2101.03206].

[219] F. Vargas, F. De Colle, D. Brethauer, R. Margutti and C.G. Bernal, *Survival of the Fittest: Numerical Modeling of SN 2014C*, *Astrophys. J.* **930** (2022) 150 [2102.12581].

[220] D. Richardson, R.L. Jenkins, J. Wright and L. Maddox, *Absolute-Magnitude Distributions of Supernovae*, *Astron. J.* **147** (2014) 118 [1403.5755].

[221] A.A. Miller et al., *The Exceptionally Luminous Type II-L SN 2008es*, *Astrophys. J.* **690** (2009) 1303 [0808.2193].

[222] S. Immler et al., *Swift and Chandra Detections of Supernova 2006jc: Evidence for Interaction of the Supernova Shock with a Circumstellar Shell*, *Astrophys. J. Lett.* **674** (2008) L85 [0712.3290].

[223] M. Singh et al., *The fast evolving type Ib Supernova SN 2015dj in NGC 7371*, *Astrophys. J.* **909** (2021) 100 [2101.09430].

[224] A. Kheirandish and K. Murase, *High-energy neutrinos from Supernovae: Prospects for Identification in Current and Future Neutrino Telescopes*, .

[225] P. Cristofari, A. Marcowith, M. Renaud, V.V. Dwarkadas, V. Tatischeff, G. Giacinti et al., *The first days of Type II-P core collapse supernovae in the gamma-ray range*, *Mon. Not. Roy. Astron. Soc.* **511** (2022) 3321 [2201.09583].

[226] P. Cristofari, M. Renaud, A. Marcowith, V.V. Dwarkadas and V. Tatischeff, *Time-dependent high-energy gamma-ray signal from accelerated particles in core-collapse supernovae: the case of SN 1993J*, *Mon. Not. Roy. Astron. Soc.* **494** (2020) 2760 [2004.02650].

[227] A. Marcowith, M. Renaud, V. Dwarkadas and V. Tatischeff, *Cosmic-ray acceleration and gamma-ray signals from radio supernovæ*, *Nucl. Phys. B Proc. Suppl.* **256-257** (2014) 94 [1409.3670].

[228] A.R. Bell, *Turbulent amplification of magnetic field and diffusive shock acceleration of cosmic rays*, *Mon. Not. Roy. Astron. Soc.* **353** (2004) 550.

[229] V.N. Zirakashvili, V.S. Ptuskin and H.J. Volk, *Modeling Bell's Non-resonant Cosmic Ray Instability*, *Astrophys. J.* **678** (2008) 255 [0801.4486].

[230] C. Haggerty, D. Caprioli and E. Zweibel, *Hybrid Simulations of the Resonant and Non-Resonant Cosmic Ray Streaming Instability*, *PoS* **ICRC2019** (2020) 279 [1909.06346].

[231] N. Smith, W. Li, A.V. Filippenko and R. Chornock, *Observed fractions of core-collapse supernova types and initial masses of their single and binary progenitor stars*, *Mon. Not. Roy. Astron. Soc.* **412** (2011) 1522 [1006.3899].

[232] S.E. Woosley, T. Sukhbold and D.N. Kasen, *Model Light Curves for Type Ib and Ic Supernovae*, *Astrophys. J.* **913** (2021) 145 [2009.06868].

[233] S. Immler, M. Modjaz, W. Landsman, F. Bufano, P.J. Brown, P. Milne et al., *Swift and Chandra Detections of Supernova 2006jc: Evidence for Interaction of the Supernova Shock with a Circumstellar Shell*, *Astrophys. J. Lett.* **674** (2008) L85 [0712.3290].

[234] D. Milisavljevic et al., *Metamorphosis of SN 2014C: Delayed Interaction Between a Hydrogen Poor Core-collapse Supernova and a Nearby Circumstellar Shell*, *Astrophys. J.* **815** (2015) 120 [1511.01907].

[235] B.P. Thomas, J.C. Wheeler, V.V. Dwarkadas, C. Stockdale, J. Vinkó, D. Pooley et al., *Seven Years of SN 2014C: A Multiwavelength Synthesis of an Extraordinary Supernova*, *Astrophys. J.* **930** (2022) 57 [2203.12747].

[236] E. Zapartas et al., *Delay-time distribution of core-collapse supernovae with late events resulting from binary interaction*, *Astron. Astrophys.* **601** (2017) A29 [1701.07032].

[237] F. Vargas, F. De Colle, D. Brethauer, R. Margutti and C.G. Bernal, *Survival of the Fittest: Numerical Modeling of SN 2014C*, *Astrophys. J.* **930** (2022) 150 [2102.12581].

[238] D. Brethauer, R. Margutti, D. Milisavljevic, M.F. Bietenholz, R. Chornock, D.L. Coppejans et al., *Seven Years of Coordinated Chandra-NuSTAR Observations of SN 2014C Unfold the Extreme Mass-loss History of Its Stellar Progenitor*, *Astrophys. J.* **939** (2022) 105 [2206.00842].

[239] A. Balasubramanian, A. Corsi, E. Polisensky, T.E. Clarke and N.E. Kassim, *Radio Observations of SN2004dk with VLITE Confirm Late-time Rebrightening*, *Astrophys. J.* **923** (2021) 32 [2101.07348].

[240] N. Smith, *Mass Loss: Its Effect on the Evolution and Fate of High-Mass Stars*, *Ann. Rev. Astron. Astrophys.* **52** (2014) 487 [1402.1237].

[241] P. Sarmah, S. Chakraborty, I. Tamborra and K. Auchettl, *High energy particles from young supernovae: gamma-ray and neutrino connections*, *JCAP* **2022** (2022) 011 [2204.03663].

[242] A. Stasik, *Search for High Energetic Neutrinos from Core Collapse Supernovae using the IceCube Neutrino Telescope*, Ph.D. thesis, 01, 2018.

[243] E. Quataert and J. Shiode, *Wave-driven mass loss in the last year of stellar evolution: setting the stage for the most luminous core-collapse supernovae*, *Mon. Not. R. Astron. Soc.* **423** (2012) L92 [1202.5036].

[244] A. Mastichiadis, *On the high energy non-thermal emission from shell-type supernova remnants.*, *aap* **305** (1996) L53 [astro-ph/9601132].

[245] P. Blasi, *The Origin of Galactic Cosmic Rays*, *Astron. Astrophys. Rev.* **21** (2013) 70 [1311.7346].

[246] M. Cardillo, E. Amato and P. Blasi, *On the cosmic ray spectrum from type II Supernovae expanding in their red giant presupernova wind*, *Astropart. Phys.* **69** (2015) 1 [1503.03001].

[247] P. Cristofari, P. Blasi and D. Caprioli, *Microphysics of Diffusive Shock Acceleration: Impact on the Spectrum of Accelerated Particles*, *Astrophys. J.* **930** (2022) 28 [2203.15624].

[248] A.R. Bell, *The interaction of cosmic rays and magnetized plasma*, *Monthly Notices of the Royal Astronomical Society* **358** (2005) 181 [https://academic.oup.com/mnras/article-pdf/358/1/181/3479398/358-1-181.pdf].

[249] S.G. Lucek and A.R. Bell, *Non-linear amplification of a magnetic field driven by cosmic ray streaming*, *Monthly Notices of the Royal Astronomical Society* **314** (2000) 65 [https://academic.oup.com/mnras/article-pdf/314/1/65/3566804/314-1-65.pdf].

[250] K.M. Schure and A.R. Bell, *Cosmic ray acceleration in young supernova remnants*, *Monthly Notices of the Royal Astronomical Society* **435** (2013) 1174 [https://academic.oup.com/mnras/article-pdf/435/2/1174/3490642/stt1371.pdf].

[251] A.R. Bell, K.M. Schure, B. Reville and G. Giacinti, *Cosmic-ray acceleration and escape from supernova remnants*, *Monthly Notices of the Royal Astronomical Society* **431** (2013) 415 [https://academic.oup.com/mnras/article-pdf/431/1/415/18243010/stt179.pdf].

[252] M.C. Stroh, G. Terreran, D.L. Coppejans, J.S. Bright, R. Margutti, M.F. Bietenholz et al., *Luminous Late-time Radio Emission from Supernovae Detected by the Karl G. Jansky Very Large Array Sky Survey (VLASS)*, *Astrophys. J.* **923** (2021) L24 [2106.09737].

[253] K. Murase, T.A. Thompson, B.C. Lacki and J.F. Beacom, *New Class of High-Energy Transients from Crashes of Supernova Ejecta with Massive Circumstellar Material Shells*, *Phys. Rev. D* **84** (2011) 043003 [1012.2834].

[254] B. Katz, N. Sapir and E. Waxman, *X-rays, γ-rays and neutrinos from collisionless shocks in supernova wind breakouts*, in *Death of Massive Stars: Supernovae and Gamma-Ray Bursts*, P. Roming, N. Kawai and E. Pian, eds., vol. 279, pp. 274–281, Sept., 2012, DOI [1106.1898].

[255] S. Celli, G. Morlino, S. Gabici and F.A. Aharonian, *Exploring particle escape in supernova remnants through gamma rays*, *Mon. Not. Roy. Astron. Soc.* **490** (2019) 4317 [1906.09454].

[256] B.D. Metzger, D. Caprioli, I. Vurm, A.M. Beloborodov, I. Bartos and A. Vlasov, *Novae as Tevatrons: prospects for CTA and IceCube*, *Monthly Notices of the Royal Astronomical Society* **457** (2016) 1786 [https://academic.oup.com/mnras/article-pdf/457/2/1786/2926159/stw123.pdf].

[257] P. Sarmah, S. Chakraborty, I. Tamborra and K. Auchettl, *Gamma-rays and neutrinos from supernovae of Type Ib/c with late time emission*, 2303.13576.

[258] ICECUBE collaboration, *Search for steady point-like sources in the astrophysical muon neutrino flux with 8 years of IceCube data*, *Eur. Phys. J. C* **79** (2019) 234 [1811.07979].

[259] L. Ambrogi, S. Celli and F. Aharonian, *On the potential of Cherenkov Telescope Arrays and KM3 Neutrino Telescopes for the detection of extended sources*, *Astropart. Phys.* **100** (2018) 69 [1803.03565].

[260] R. Abbasi et al., *Constraining High-Energy Neutrino Emission from Supernovae with IceCube*, 2303.03316.

[261] R. Abbasi, Y. Abdou, T. Abu-Zayyad, J. Adams, J.A. Aguilar, M. Ahlers et al., *Time-integrated Searches for Point-like Sources of Neutrinos with the 40-string IceCube Detector*, *apj* **732** (2011) 18 [1012.2137].

[262] A. Lien, B.D. Fields and J.F. Beacom, *Synoptic Sky Surveys and the Diffuse Supernova Neutrino Background: Removing Astrophysical Uncertainties and Revealing Invisible Supernovae*, *Phys. Rev. D* **81** (2010) 083001 [1001.3678].

[263] D.D. Dzhappuev et al., *Upper Limits on the Isotropic Diffuse Flux of Cosmic PeV Photons from Carpet-2 Observations*, *JETP Lett.* **117** (2023) 184 [2212.01088].

[264] N.-C. Sun, J.R. Maund, P.A. Crowther, R. Hirai, A. Kashapov, J.-F. Liu et al., *An environmental analysis of the type ib sn 2019yvr and the possible presence of an inflated binary companion*, *Mon. Not. R. Astron. Soc.* **510** (2022) 3701.

[265] M.F. Bietenholz, F. De Colle, J. Granot, N. Bartel and A.M. Soderberg, *Radio limits on off-axis GRB afterglows and VLBI observations of SN 2003gk*, *Mon. Not. R. Astron. Soc.* **440** (2014) 821 [1310.7171].

[266] S. Wellons, A.M. Soderberg and R.A. Chevalier, *Radio Observations Reveal Unusual Circumstellar Environments for Some Type Ibc Supernova Progenitors*, *Astrophys. J.* **752** (2012) 17 [1201.5120].

[267] FERMI-LAT collaboration, *The spectrum of isotropic diffuse gamma-ray emission between 100 MeV and 820 GeV*, *Astrophys. J.* **799** (2015) 86 [1410.3696].

[268] S. Hussain, R.A. Batista, E.M. de Gouveia Dal Pino and K. Dolag, *The diffuse gamma-ray flux from clusters of galaxies*, *Nature Commun.* **14** (2023) 2486 [2203.01260].

[269] ICECUBE collaboration, *Observation of high-energy neutrinos from the Galactic plane*, *Science* **380** (2023) 6652 [2307.04427].

[270] K. Murase, D. Guetta and M. Ahlers, *Hidden Cosmic-Ray Accelerators as an Origin of TeV-PeV Cosmic Neutrinos*, *Phys. Rev. Lett.* **116** (2016) 071101 [1509.00805].

[271] P.B. Denton and I. Tamborra, *The Bright and Choked Gamma-Ray Burst Contribution to the IceCube and ANTARES Low-Energy Excess*, *JCAP* **04** (2018) 058 [1802.10098].

[272] M. Ahlers and F. Halzen, *Pinpointing Extragalactic Neutrino Sources in Light of Recent IceCube Observations*, *Phys. Rev. D* **90** (2014) 043005 [1406.2160].

[273] K. Murase, S.S. Kimura and P. Meszaros, *Hidden Cores of Active Galactic Nuclei as the Origin of Medium-Energy Neutrinos: Critical Tests with the MeV Gamma-Ray Connection*, *Phys. Rev. Lett.* **125** (2020) 011101 [1904.04226].

[274] N. Senno, P. Mészáros, K. Murase, P. Baerwald and M.J. Rees, *Extragalactic star-forming galaxies with hypernovae and supernovae as high-energy neutrino and gamma-ray sources: the case of the 10 TeV neutrino data*, *Astrophys. J.* **806** (2015) 24 [1501.04934].

[275] E. Cappellaro et al., *Supernova rates from the SUDARE VST-OmegaCAM search - I. Rates per unit volume*, *Astron. Astrophys.* **584** (2015) A62 [1509.04496].

[276] PLANCK collaboration, *Planck 2015 results. XIII. Cosmological parameters*, *Astron. Astrophys.* **594** (2016) A13 [1502.01589].

[277] L.-G. Strolger, T. Dahlen, S.A. Rodney, O. Graur, A.G. Riess, C. McCully et al., *The Rate of Core Collapse Supernovae to Redshift 2.5 From The CANDELS and CLASH Supernova Surveys*, *Astrophys. J.* **813** (2015) 93 [1509.06574].

[278] J. Melinder, T. Dahlen, L. Mencía Trinchant, G. Östlin, S. Mattila, J. Sollerman et al., *The rate of supernovae at redshift 0.1-1.0. The Stockholm VIMOS Supernova Survey III*, *aap* **545** (2012) A96 [1206.6897].

[279] P. Madau and M. Dickinson, *Cosmic Star Formation History*, *Ann. Rev. Astron. Astrophys.* **52** (2014) 415 [1403.0007].

[280] E.E. Salpeter, *The Luminosity function and stellar evolution*, *Astrophys. J.* **121** (1955) 161.

[281] H. Yuksel, M.D. Kistler, J.F. Beacom and A.M. Hopkins, *Revealing the High-Redshift Star Formation Rate with Gamma-Ray Bursts*, *Astrophys. J. Lett.* **683** (2008) L5 [0804.4008].

[282] J.D. Finke, S. Razzaque and C.D. Dermer, *Modeling the Extragalactic Background Light from Stars and Dust*, *Astrophys. J.* **712** (2010) 238 [0905.1115].

[283] A. Saldana-Lopez, A. Domínguez, P.G. Pérez-González, J. Finke, M. Ajello, J.R. Primack et al., *An observational determination of the evolving extragalactic background light from the multiwavelength HST/CANDELS survey in the Fermi and CTA era*, *Mon. Not. Roy. Astron. Soc.* **507** (2021) 5144 [2012.03035].

[284] KM3NeT collaboration, *Sensitivity estimates for diffuse, point-like, and extended neutrino sources with KM3NeT/ARCA*, *JINST* **16** (2021) C09030 [2107.13050].

[285] M. Di Mauro, S. Manconi, H.-S. Zechlin, M. Ajello, E. Charles and F. Donato, *Deriving the contribution of blazars to the Fermi-LAT Extragalactic γ-ray background at $E > 10$ GeV with efficiency corrections and photon statistics*, *Astrophys. J.* **856** (2018) 106 [1711.03111].

[286] M. Lisanti, S. Mishra-Sharma, L. Necib and B.R. Safdi, *Deciphering Contributions to the Extragalactic Gamma-Ray Background from 2 GeV to 2 TeV*, *Astrophys. J.* **832** (2016) 117 [1606.04101].

[287] T. Linden, *Star-Forming Galaxies Significantly Contribute to the Isotropic Gamma-Ray Background*, *Phys. Rev. D* **96** (2017) 083001 [1612.03175].

[288] H.J. Völk, F.A. Aharonian and D. Breitschwerdt, *The Nonthermal Energy Content and Gamma-Ray Emission of Starburst Galaxies and Clusters of Galaxies*, *Space Science Reviews* **75** (1996) 279.

[289] K. Fang, B.D. Metzger, I. Vurm, E. Aydi and L. Chomiuk, *High-energy Neutrinos and Gamma Rays from Nonrelativistic Shock-powered Transients*, *Astrophys. J.* **904** (2020) 4 [2007.15742].

[290] IceCube collaboration, *Searching for High-Energy Neutrinos from Core-Collapse Supernovae with IceCube*, *PoS* **ICRC2021** (2021) 1116 [2107.09317].

[291] HiRes collaboration, *First observation of the Greisen-Zatsepin-Kuzmin suppression*, *Phys. Rev. Lett.* **100** (2008) 101101 [astro-ph/0703099].

[292] V. Berezinsky, A. Gazizov and S. Grigorieva, *On astrophysical solution to ultrahigh energy cosmic rays*, *Phys. Rev. D* **74** (2006) 043005.

[293] S. Sarkar, *New physics from ultrahigh-energy cosmic rays*, *Acta Phys. Polon. B* **35** (2004) 351 [hep-ph/0312223].

[294] G.A. Medina-Tanco and A.A. Watson, *Dark matter halos and the anisotropy of ultrahigh-energy cosmic rays*, *Astropart. Phys.* **12** (1999) 25 [astro-ph/9903182].

[295] H.B. Kim and P. Tinyakov, *Constraining superheavy dark matter model of UHECR with SUGAR data*, *Astropart. Phys.* **21** (2004) 535 [astro-ph/0306413].

[296] R. Aloisio and F. Tortorici, *Super Heavy Dark Matter and UHECR Anisotropy at Low Energy*, *Astropart. Phys.* **29** (2008) 307 [0706.3196].

[297] N.W. Evans, F. Ferrer and S. Sarkar, *The Anisotropy of the ultrahigh-energy cosmic rays*, *Astropart. Phys.* **17** (2002) 319 [astro-ph/0103085].

[298] L.A. Anchordoqui, H. Goldberg, D. Hooper, S. Sarkar and A.M. Taylor, *Predictions for the Cosmogenic Neutrino Flux in Light of New Data from the Pierre Auger Observatory*, *Phys. Rev. D* **76** (2007) 123008 [0709.0734].

[299] M. Ahlers, L.A. Anchordoqui and S. Sarkar, *Neutrino diagnostics of ultra-high energy cosmic ray protons*, *Phys. Rev. D* **79** (2009) 083009 [0902.3993].

[300] M. Ahlers, L.A. Anchordoqui, M.C. Gonzalez-Garcia, F. Halzen and S. Sarkar, *GZK Neutrinos after the Fermi-LAT Diffuse Photon Flux Measurement*, *Astropart. Phys.* **34** (2010) 106 [1005.2620].

[301] D. Hooper, A.M. Taylor and S. Sarkar, *Cosmogenic photons as a test of ultra-high energy cosmic ray composition*, *Astroparticle Physics* **34** (2011) 340 [1007.1306].

[302] M. Birkel and S. Sarkar, *Extremely high-energy cosmic rays from relic particle decays*, *Astropart. Phys.* **9** (1998) 297 [hep-ph/9804285].

[303] S. Sarkar and R. Toldra, *The High-energy cosmic ray spectrum from relic particle decay*, *Nucl. Phys. B* **621** (2002) 495 [hep-ph/0108098].

[304] J. Heinze, D. Boncioli, M. Bustamante and W. Winter, *Cosmogenic neutrinos challenge the cosmic-ray proton dip model*, *The Astrophysical Journal* **825** (2016) 122.

[305] D.J. Fixsen, *The Temperature of the Cosmic Microwave Background*, *apj* **707** (2009) 916 [0911.1955].

[306] R.J. Protheroe and P.L. Biermann, *A New estimate of the extragalactic radio background and implications for ultrahigh-energy gamma-ray propagation*, *Astropart. Phys.* **6** (1996) 45 [astro-ph/9605119].

[307] I.C. Niţu, H.T.J. Bevins, J.D. Bray and A.M.M. Scaife, *An updated estimate of the cosmic radio background and implications for ultra-high-energy photon propagation*, *Astropart. Phys.* **126** (2021) 102532 [2004.13596].

[308] K.M. Groth, Y. Génolini and M. Ahlers, *Improved Limits on Cosmogenic Fluxes from Ultra-High Energy Cosmic Rays*, *PoS* **ICRC2021** (2021) 1005.

[309] D.J. Fixsen, A. Kogut, S. Levin, M. Limon, P. Lubin, P. Mirel et al., *Arcade 2 measurement of the absolute sky brightness at 3–90 ghz*, *The Astrophysical Journal* **734** (2011) 5.

[310] R. Alves Batista, A. Dundovic, M. Erdmann, K.-H. Kampert, D. Kuempel, G. Müller et al., *CRPropa 3 - a Public Astrophysical Simulation Framework for Propagating Extraterrestrial Ultra-High Energy Particles*, *JCAP* **05** (2016) 038 [1603.07142].

[311] V.S. Berezinskii, S.V. Bulanov, V.A. Dogiel and V.S. Ptuskin, *Astrophysics of cosmic rays* (1990).

[312] R.J. Protheroe, *Acceleration and interaction of ultrahigh-energy cosmic rays*, astro-ph/9812055.

[313] K. Mannheim, R.J. Protheroe and J.P. Rachen, *On the cosmic ray bound for models of extragalactic neutrino production*, *Phys. Rev. D* **63** (2001) 023003 [astro-ph/9812398].

[314] ICECUBE collaboration, *IceCube Data for Neutrino Point-Source Searches Years 2008-2018*, 2101.09836.

[315] "Cosmic ray spectrum icecube masterclass." https://masterclass.icecube.wisc.edu/en/analyses/cosmic-ray-energy-spectrum.

[316] R. Durrer, *The cosmic microwave background: the history of its experimental investigation and its significance for cosmology*, *Class. Quant. Grav.* **32** (2015) 124007 [1506.01907].

[317] T.A. Clark, L.W. Brown and J.K. Alexander, *Spectrum of the Extra-galactic Background Radiation at Low Radio Frequencies*, *nat* **228** (1970) 847.

[318] R. Alves Batista et al., *CRPropa 3.2 — an advanced framework for high-energy particle propagation in extragalactic and galactic spaces*, *JCAP* **09** (2022) 035 [2208.00107].

[319] PIERRE AUGER collaboration, *Probing the origin of ultra-high-energy cosmic rays with neutrinos in the EeV energy range using the Pierre Auger Observatory*, *JCAP* **10** (2019) 022 [1906.07422].

[320] S. Thoudam, J.P. Rachen, A. van Vliet, A. Achterberg, S. Buitink, H. Falcke et al., *Cosmic-ray energy spectrum and composition up to the ankle: the case for a second Galactic component*, *Astron. Astrophys.* **595** (2016) A33 [1605.03111].

[321] PIERRE AUGER collaboration, *The Pierre Auger Observatory Upgrade - Preliminary Design Report*, 1604.03637.

[322] K. Møller, P.B. Denton and I. Tamborra, *Cosmogenic Neutrinos Through the GRAND Lens Unveil the Nature of Cosmic Accelerators*, *JCAP* **05** (2019) 047 [1809.04866].

[323] D. Ehlert, A. van Vliet, F. Oikonomou and W. Winter, *Constraints on the proton fraction of cosmic rays at the highest energies and the consequences for cosmogenic neutrinos and photons*, 2304.07321.

[324] D. Hooper, A. Taylor and S. Sarkar, *The Impact of heavy nuclei on the cosmogenic neutrino flux*, *Astropart. Phys.* **23** (2005) 11 [astro-ph/0407618].

[325] M. Ave, N. Busca, A.V. Olinto, A.A. Watson and T. Yamamoto, *Cosmogenic neutrinos from ultra-high energy nuclei*, *Astropart. Phys.* **23** (2005) 19 [astro-ph/0409316].

[326] K.-H. Kampert, J. Kulbartz, L. Maccione, N. Nierstenhoefer, P. Schiffer, G. Sigl et al., *CRPropa 2.0 - A public framework for propagating high energy nuclei, secondary gamma rays and neutrinos*, *Astroparticle Physics* **42** (2013) 41 [1206.3132].

[327] M. Gervasi, A. Tartari, M. Zannoni, G. Boella and G. Sironi, *The Contribution of the Unresolved Extragalactic Radio Sources to the Brightness Temperature of the Sky*, *apj* **682** (2008) 223 [0803.4138].

[328] R. Subrahmanyan, Private communication.

[329] A.J.B. Simon, *The origin of the extragalactic background radiation between 0.5 and 400 MHz.*, *mnras* **180** (1977) 429.

[330] A. Kogut, D.J. Fixsen, S.M. Levin, M. Limon, P.M. Lubin, P. Mirel et al., *ARCADE 2 Observations of Galactic Radio Emission*, *apj* **734** (2011) 4 [0901.0562].

[331] M. Seiffert, D.J. Fixsen, A. Kogut, S.M. Levin, M. Limon, P.M. Lubin et al., *Interpretation of the ARCADE 2 Absolute Sky Brightness Measurement*, *apj* **734** (2011) 6.

[332] R. Subrahmanyan and R. Cowsik, *Is there an Unaccounted for Excess in the Extragalactic Cosmic Radio Background?*, *Astrophys. J.* **776** (2013) 42 [1305.7060].

[333] N. Fornengo, R. Lineros, M. Regis and M. Taoso, *Possibility of a Dark Matter Interpretation for the Excess in Isotropic Radio Emission Reported by ARCADE*, *Phys. Rev. Lett.* **107** (2011) 271302 [1108.0569].

[334] P.L. Biermann and B.C. Harms, *Dark energy as stimulated emission of gravitons from a background brane*, *arXiv e-prints* (2013) arXiv:1305.0498 [1305.0498].

[335] R. Mondal et al., *Tight constraints on the excess radio background at z = 9.1 from LOFAR*, *Mon. Not. Roy. Astron. Soc.* **498** (2020) 4178 [2004.00678].

[336] M.G. Labate, J. Wagg, B. Alachkar, S. Breen, G. Swart and A. van Es, *The most sensitive radio telescope to deliver unprecedented and global open science: The square kilometer array (50 mhz - 15.3 ghz)*, in *2021 15th European Conference on Antennas and Propagation (EuCAP)*, pp. 1–5, 2021, DOI.

[337] C. Simpson, *Extragalactic radio surveys in the pre-Square Kilometre Array era*, *Royal Society Open Science* **4** (2017) 170522 [1706.06603].

[338] GRAND collaboration, *The Giant Radio Array for Neutrino Detection (GRAND) project*, *PoS* **ICRC2021** (2021) 1181 [2108.00032].

[339] ANITA collaboration, *The Antarctic Impulsive Transient Antenna Ultra-high Energy Neutrino Detector Design, Performance, and Sensitivity for 2006-2007 Balloon Flight*, *Astropart. Phys.* **32** (2009) 10 [0812.1920].

[340] I. Kravchenko, S. Hussain, D. Seckel, D. Besson, E. Fensholt, J. Ralston et al., *Updated results from the RICE experiment and future prospects for ultra-high energy neutrino detection at the south pole*, *prd* **85** (2012) 062004 [1106.1164].

[341] E. Waxman and J.N. Bahcall, *High-energy neutrinos from astrophysical sources: An Upper bound*, *Phys. Rev. D* **59** (1999) 023002 [hep-ph/9807282].

[342] ANITA collaboration, *Constraints on the diffuse high-energy neutrino flux from the third flight of ANITA*, *Phys. Rev. D* **98** (2018) 022001 [1803.02719].

[343] T. Padmanabhan, *Theoretical Astrophysics*, vol. 1, Cambridge University Press (2000), 10.1017/CBO9781139171083.

[344] G. Ghisellini, G. Ghirlanda, G. Oganesyan, S. Ascenzi, L. Nava, A. Celotti et al., *Proton–synchrotron as the radiation mechanism of the prompt emission of gamma-ray bursts?*, *Astron. Astrophys.* **636** (2020) A82 [1912.02185].